UNIVERZITA PALACKÉHO V OLOMOUCI
PŘÍRODOVĚDECKÁ FAKULTA

Katedra optiky

Charakterizace vnějších stupňů volnosti světla a optická metrologie

Mgr. Martin Paúr

Disertační práce předložena k získání titulu
Doktor Filosofie

Školitel: prof. Mgr. Jaroslav Řeháček, Ph.D.

Olomouc 2020

PALACKÝ UNIVERSITY OLOMOUC
FACULTY OF SCIENCE

Department of optics

Characterization of external degrees of freedom of light and optical metrology

Mgr. Martin Paúr

A dissertation thesis presented for the degree of
Doctor of Philosophy

Supervisor: prof. Mgr. Jaroslav Řeháček, Ph.D.

Olomouc 2020

Abstrakt a Klíčová slova

Tato disertační práce se zabývá studiem moderních technik a vědeckých aplikací, a to převážně v oblasti optického rozlišení jednoho nebo dvou bodových zdrojů a okrajově mechanismem samoobnovení u optických polí. Začátek práce je věnován stručnému úvodu rozšířeném o aktuální vývoj dané problematiky. V následující kapitole je prezentován přehled hlavních teoretických principů a představení nejdůležitějších komponent využitých během experimentů. Hlavní část práce se poté zaměřuje na dvou-bodové rozlišení s použitím aktuálních metod využívající kvantových protokolů se záměrem překonat klasická rozlišovací kritéria, mj. použití nových metod superrozlišení a na modernější popis mechanismu samorekonstrukce u Gaussovských svazků. Vlastní přínos v podobě dosažených experimentálních výsledků je důkladněji rozpracován v kapitolách 4 až 8.

V kapitolách 4 až 7 je prezentován výzkum v oblasti optického superrozlišení z pohledu teorie informace a teorie parametrického odhadu. Aplikací kvantových ekvivalentů Fisherovy míry informace a Cramér-Raovi dolní meze rozptylu bylo dokázáno, že v případě rozlišení dvou nekoherentních bodových zdrojů je možné nalézt optimální měření překonávající klasické rozlišovací kritéria teoreticky bez omezení.

V kapitole 8 je představeno studium samorekonstrukčních vlastností u Gaussovských svazků za pomoci komplexního vlnového popisu a Babinetova principu. Byla zde zavedena nová míra kvantifikace podobnosti mezi omezeným a neomezeným svazkem a nová definice minimální rekonstrukční vzdálenosti. Tyto teoretické předpoklady byly posléze úspěšně experimentálně ověřeny.

Klíčová slova

Klasické dvou-bodové rozlišení, Rayleighovo kritérium, Rayleighova kletba, superrozlišení, Fisherova informace, kvantová Fisherova informace, Cramér-Raova dolní mez rozptylu, kvantová Cramér-Raova dolní mez rozptylu, nedifrakční svazky, samoobnovení optických svazků a prostorový modulátor světla.

Abstact and Key words

This dissertation thesis presents study of modern techniques and scientific applications mainly in the area of optical resolution of one or two point sources and partially of the self-healing mechanism of optical fields. The beginning of the work is devoted to the brief introduction extended with actual research progress in selected topics. The following chapter provides an overview of the main theoretical principles and an introduction to the most important components used during the experiments. The main part of this work is focused on two-point resolution using actual methods utilizing quantum protocols with the intention to overcome the classical resolution criteria, i.e., uses of new superresolution methods and a more modern description of the mechanism of self-reconstruction of Gaussian beams. My contribution in the form of achieved experimental results is thoroughly elaborated in Chapters 4 - 8.

In Chapters 4 - 7, the research in the field of optical superresolution from the point of view of information and parametric estimation theory is introduced. It has been shown that for the case of resolution of two incoherent point sources, applying the quantum equivalents of the Fisher information and Cramér-Rao lower bound leads to the possibility to find optimal measurement schemes which surpass the classical resolution criteria, theoretically without any limitation.

In Chapter 8, the study of self-reconstruction properties of Gaussian beams using comprehensive wave optics description and Babinet principle is introduced. The novel quantitative metric of similarity between obstructed and unobstructed beam and a new definition of minimal reconstruction distance were formed. These theoretical assumptions were subsequently experimentally verified.

Key words

Classical two-point resolution, Rayleigh's criterion, Rayleigh's curse, superresolution, Fisher information, quantum Fisher information, Cramér-Rao lower bound, quantum Cramér-Rao lower bound, non-diffracting beams, beam self-healing, spatial light modulator.

Acknowledgements

Firstly, I would like to thank my supervisor, Jaroslav Řeháček for his support, help, and inspiring scientific discussions, that showed me the true potential of the optical world. I would like to extend my gratitude to Bohumil Stoklasa for his indispensable support in the laboratory and his imperishable experimental enthusiasm, that always pushed me forward.

Special thanks belongs to L.L. Sánchez-Soto for all eye-opening discussions and ideas and for my interships in Madrid and Erlangen. Furthermore, I would like to thank Zdeněk Hradil, Libor Moťka and other members of the Department of optics for various help and support during my studies.

Finally, my warmest thanks belong to my family, friends and my girlfriend Lucia for their endless patience, love and care.

Thank you.

Martin

Declaration

I hereby declare that this thesis is my own work and is based on five original publications [1–5] which summarized my most significant results reached during my Ph.D. studies. My contribution to these publications was mainly in experimental realizations of proposed theoretical models in classical optical systems and furthermore analysis of the experimental data in Chapter 8. The main goals of this study were to validate theoretical models and confirm their experimental feasibility and robustness.

I declare that I wrote this Ph.D. thesis entitled ***Characterization of external degrees of freedom of light and optical metrology*** on my own under the guidance of my supervisor prof. Mgr. Jaroslav Řeháček, Ph.D. This Thesis uses only the resources cited in the Bibliography section.

I agree with the further usage of this thesis according to the requirements of the Palacký University Olomouc and the Department of optics.

In Olomouc, 14th September, 2020 .....

Martin Paúr

List of Abbreviations

3D	Three-dimensional
BS	Beamsplitter
CCD	Charge-coupled device
CGH	Computer generated hologram
CMOS	Complementary Metal–Oxide–Semiconductor
CRLB	Cramér-Rao lower bound
DMD	Digital micromirror device
DLP	Digital light projector
EMCCD	Electron-multiplying CCD camera
FWHM	Full width half maximum
He-Ne	Helium-Neon
HG	Hermite-Gaussian mode
LCD	Liquid crystal displays
LCOS	Liquid crystal on silicon
MSe	Mean square estimator
MSE	Mean square error
MEMS	Micro-electro-mechanical system
MVU	Minimum variance unbiased
PDF	Probability density function
POVM	Positive-operator valued measurement
PSF	Point-spread function
QCRLB	Quantum Cramér-Rao lower bound
QFIM	Quantum Fisher information matrix
S-H	Shack-Hartmann wavefront sensor
SLD	Symmetric logarithmic derivative
SLM	Spatial light modulator
RLD	Right logarithmic derivative
TFT	Thin-film transistors
TN-LC	Twisted nematic liquid crystals

Contents

Chapter 1

Goal of the Thesis

The aim of this dissertation thesis is to comprehensively present my experimental research, which was realized during my Ph.D. studies. The topic of the thesis is devoted to the study of methods and experimental applications in the scope of two-point resolution and self-reconstruction mechanism of optical fields. The main focus is dedicated to the application of current quantum protocols overcoming the classical two-point resolution criteria and on description and quantification of self-healing mechanism of Gaussian beams. These proof-of-principle experiments verify the suggested novel theoretical principles, and validate their implementation and feasibility in real conditions.

The objective of this chapter is to overview the subject of this thesis and introduce five proof-of-principle experiments, based on five publications [1–5], shortly discussed below. *Chapter 2* briefly describes contemporary state of research mainly dedicated to the two main above mentioned topics. *Chapter 3* includes theoretical formalism as well as experimental tools essential to the submitted research. Attention is paid to Rayleigh's criterion, Fisher Information, Quantum Fisher information and spatial light modulators (SLM). Following *Chapters 4 - 8* introduce achieved experimental results. At the beginning of each Chapter, there is a short abstract describing the basic idea and motivation. It is followed by section of the theory important for understanding the experiment, actual experiment, achieved results and short summary. Finally, the main results are reviewed in *Chapter 9*. The list of my publications, citation index and bibliography section are given at the end of the thesis.

As we mentioned above, the main chapters result from the following scientific articles:

Chapter 4 introduces one of the first experimental realization of recently proposed measuring method, called spatial-mode demultiplexing (SPADE). Tsang et al. (2016) [6] proposed this scheme promising to violate the classical Rayleigh's resolution criterion for two incoherent point sources. Surprisingly, by applying quantum protocols, namely quantum Fisher information, they found that this quantity remains constant for any separation between two sources. During our research, an optimal experimental technique based on the ideas of the SPADE method was developed, that confirmed a significant overcoming of classical resolution criteria. The experiment itself was based on digital holography components and signal decomposition into Hermite-Gaussian mode basis. This Chapter is based on a publication [1] M. Paúr, B. Stoklasa, Z. Hradil, L. L. Sánchez-Soto and J. Řeháček. '*Achieving the ultimate optical resolution*'. In: *Optica* **3**.**10** (2016), pp. 1144–1147.

Research in *Chapter 5* builds on previous results by focusing on two-point resolution from the perspective of direct charge-coupled device (CCD) detection. For this typical laboratory scenario, the Fisher information decays quadratically to zero with vanishing separation between point sources, effect denominated as Rayleigh's curse. Contrary to this belief, an optimal optical transformation was found providing a linear decrease of Fisher information. From the acquired experimental data, it was found that any "well-behaved" symmetric point spread function (PSF) can be easily converted to a special form of information-rich zero intensity region using a simple non-absorbing signum filter. This chapter is based on publication [2] M. Paúr, B. Stoklasa, J. Grover, A. Krzic, L. L. Sánchez-Soto, Z. Hradil and J. Řeháček. '*Tempering Rayleigh's curse with PSF shaping*'. In: *Optica* **5**.**10** (2018), pp. 1177–1180.

Chapter 6 presents further studies on the impact of "zero" intensity areas of point spread function on two-point resolution in direct detection regime. It was confirmed theoretically and also experimentally, that these zeros contain the majority of the necessary information and notably contribute to the Fisher information linear scaling for small separations. This was confirmed by two spectroscopic experiments, using Sinc PSF consisting of large number of natural zeros, where the separations of naturally and artificially generated spectral doublets were measured. This Chapter is based on publication [3] M. Paúr, B. Stoklasa, D. Koutný, J. Řeháček, Z. Hradil et al. '*Reading out Fisher information from the zeros of the point spread function*'. In: *Optics Letters* **44**.**12** (2019), pp. 3114–3117.

Chapter 7 is focused on overcoming of classical limits of the longitudinal (axial) localization of one optical point source. This research revealed that in the case of a Gaussian point source, the saturation of the quantum limit requires only single intensity scan provided by the CCD camera suitably positioned at one of two optimal transverse detection planes. The theoretical principles were experimentally confirmed using a simple microscopy setup, with achieved accuracy in the order of tens of nanometers. This Chapter results from the publication [4] J. Řeháček, M. Paúr, B. Stoklasa, D. Koutný, Z. Hradil and L. L. Sánchez-Soto. '*Intensity-Based Axial Localization at the Quantum Limit*'. In: *Physical Review Letters* **123.19** (2019), p. 193601.

In *Chapter 8*, the self-healing mechanism of optical fields is studied. This optical property has been attributed only to non-diffractive beams, such as Bessel beams for a long time, and characterizes the beam ability to fully recover beam intensity profile after interaction with solid obstruction in a certain plane behind it. Recently, the comprehensive description of this effect was published by Aiello et al. (2014), using wave optics description and the Babinet principle. Here the presented research using this wave description advances the self-reconstruction potential for almost any kind of optical beams. Moreover, the novel metric quantifying the similarity between an obstructed and unobstructed beam and a new definition of minimal reconstruction distance were defined. The rightness of these definitions was experimentally confirmed on Gaussian beam measuring the whole complex amplitude using CCD camera and Shack-Hartmann sensor. This Chapter is based on the publication [5] A. Aiello, G. S. Agarwal, M. Paúr, B. Stoklasa, Z. Hradil et al. '*Unraveling beam self-healing*'. In: *Optics Express* **25.16** (2017), pp. 19147–19157.

Chapter 2

Contemporary state of research

Optical resolution

The optical resolution has always been a pivotal concept in human life and the important area of physical sciences. The most familiar consideration about optical resolution comes from the experiences with optical imaging associated with human visual system. Historically, the human eye was one and the only optical imaging device that measured and visualized the world around us for a long period of time. Through centuries, a large number of optical instruments have been developed and modified to improve their resolving power [7].

In simple terms, the resolution limits the level of details on an object, which can be reliably observed, or distinctiveness of the number of objects in the scene. The regions in the real-world scene usually contain more or less uniform textures divided by discontinuities and also individual bright point-like structures. However, we are not able to see sharp edges or points, instead we always see blurred versions of them.

Analogously, for any image-forming optical system the "fuzzy" response to a single point-like source is known as the point spread function or impulse response. This is the notorious product of a diffraction property of light. Because of this smearing, we cannot be exactly sure what we are looking at. Our inability to resolve details beyond some scale means that different situations will give rise to the same wrong result. Similarly, if we have prior information that the scene consists of one or two equally bright closely separated point-like sources, we can use this to try to decide between these two possibilities. This fundamental problem, known as two-point resolution, has been studied by many researchers to quantify the degree of resolution attainable with a given optical device.

For simplicity, we can consider a single point source and a diffraction-limited optical imaging system described by a circular aperture. The resulting impulse response of this system is described by the Bessel function of a first kind which is known as Airy disk

[8]. This image intensity pattern consists of a central main lobe with several side-lobes. Naturally, this conception of single-point resolution has its justification in cases when we need to determine the position (centroid) of the point source [9–11]. This brings it in almost every scientific experiment, where some parameter wants to be determined. This simple setup can be considered as a baseline scenario for the following text.

Classical two-point resolution criteria

To extend the previous discussion to a two-point resolution, one can simply add another source point. Two-point resolution is then defined as the optical system's ability to resolve these two points sources of equal intensity, i.e., find the minimum distinguishable separation between them. There exist several classical resolution criteria, which are related to the diffraction-limited systems, where the performance of the system is limited only by diffraction as a result of finite size of the system aperture and the wavelength of the light. For example, the broader summary is discussed in den Dekker and van den Bos [12] and Ramsay et al. [13]. The following criteria correspond to the incoherent point-sources.

The well known Rayleigh criterion [14, 15] states that two point sources are just resolved when the central maximum of the image intensity pattern of the first point falls into the first zero minimum of the second one. This results in a distinctive intensity dip between two peaks of the PSFs. Thereto, this can be generalized for PSFs without any zeros in their side-lobes. The resolution limit is then expressed as the distance for which the ratio among the central dip and the sidelong maxima in resulting intensity distribution is equal to 0.81. Except two-point resolution, the same resolution criteria can be applied, e.g. to the separation of spectral lines in a spectrometer [16].

The Sparrow's criterion [17, 18] follows the aforementioned Rayleigh criterion. Sparrow limit defines the resolution as a situation when the central intensity dip vanishes. This means that both side maxima and the central valley merge together, and the consequential intensity pattern composes from the single central peak. Comparing these limits, the Sparrow resolution limit is approximately two-thirds of the Rayleigh limit.

Contrariwise, the Schuster limit [19] propose that the two points are just resolved if the main lobes of their PSFs do not overlap. This responds to the twice of the Rayleigh criterion.

Houston criterion [20] was postulated to resolve two points concerning the distance between lateral maxima of the composite intensity pattern. If the interval is greater or equal the full width at half maximum (FWHM) of either point source, then they can be distinguished.

A very similar criterion to Houston criterion was suggested by Buxton [21]. However,

he considered the amplitude diffraction patterns instead of the intensity and limited the resolution by unification of the closest inflection points.

The last analogous criterion is Dawes criterion. This was empirically determined by Dawes [22], observing closely spaced double stars of equal intensities by telescope. It is very close to the full width at half maximum of the point-spread function and means a 5% drop of central dip. This limit lies between the Sparrow and Rayleigh criterion.

The classical resolution limits take the PSFs as exactly known mathematical models without any noise. The corresponding resolution shrinks into a measure of the width of the main lobes and theoretically can be unlimited. Naturally, such an optical system without any errors, noise or aberrations is ideal and has never been realized in practice.

Resolution based on parameter-estimation theory

In the case of real optical systems with all systematic and non-systematic errors, the unlimited resolution is unreachable. This situation inspired researchers to look at the resolution problem from different points of view such as inverse filter theory [23–25], information theory [26, 27], decision theory and parameter-estimation theory [28, 29]. Most of the modern methods introduce the concept of *superresolution*, which basically means, that these methods violate the classical resolution criteria (diffraction limit) and provide more accurate results and discriminate smaller separations.

The parameter-estimation theory is currently one of the most discussed statistical conception. From the viewpoint of this approach, the attainable precision, respectively resolution of two incoherent point sources, can be determined. The main idea is that the ensamble of intensity measurements comprise the information about the values of unknown parameters that we want to estimate. In our case, the parameters of interest are individual locations (centroids), separation or amplitudes of the sources.

Moreover, when the probability density function for each detection is known, it can be used to construct some of the standard statistical estimators. The proper choice of this unbiased estimator influences the uncertainty of the inferred values and depends on the measured quantities and on the particular measurement configurations. As a representative example, the maximum likelihood estimator can be used. For each unbiased estimator, its variance is bounded below by the theoretical Cramér-Rao lower bound (CRLB). This quantity is reciprocally connected with the well-known Fisher information [30, 31], which describes the total amount of information per photon detection about unknown parameters in our measured data-set, i.e., expectation values of our parameters. In this way, we should be able to enumerate better performance of observation schemes and optimize signal estimation strategies [32].

It can be easily shown, that for two incoherent point sources and direct image-plane photo counting schemes, the resulting Fisher information deteriorates rapidly to zero as the separation between points approaches sub-Rayleigh region. In other words, the estimation error goes to infinity for vanishing separation and shows that the separation estimation for overlapping patterns needs different approach.

Parameter-estimation theory from viewpoint of quantum metrology

Contrary to this belief, prof. Tsang and coworkers showed in their ground-breaking paper [6], that this problem can be treated from the perspective of quantum information theory, mainly by methods adopted from quantum metrology which were shown to be relevant to the imaging and sensing [33–35]. Authors derived fundamental quantum limits for the precision of separation of two incoherent optical point sources using quantum Fisher information and associated quantum Crámer-Rao lower bound (QCRLB), which was firstly proposed by Helstrom [33]. Thus, the quantum Fisher information specifies the maximal amount of the Fisher information that cannot be beaten by any measurement, i.e., quantum Fisher infromation is optimized over all possible quantum measurements, and also quantifies the maximum accessible amount of information. Intriguingly, they discovered that the QCRLB maintains entirely constant value for any separation value. Hence, this result is in direct contrast to the quadratic outcome obtained for CRLB, dubbed as *Rayleigh's curse*. Generally, for any non-vanishing quantum Fisher information, there should exist an optimal measurement that can saturate the QCRLB and extracts the maximum available information per one photon.

Furthermore, authors suggested a linear experimental proposal based on the method called spatial-mode demultiplexing (SPADE). They showed that this technique is able to saturate the QCRLB asymptotically [36, 37] and extract the full information for the separation parameter, violating the classical Rayleigh criterion. In recent years, prof. Tsang enhanced this technique in moments-estimation problem of arbitrary sub-diffraction objects promising applications in both astronomy and fluorescence microscopy. Foremost, the fundamental introduction based on statistical optics was presented in [38]. The more adequate replenishment of semiclassical formalism inclusive of diffraction, photon shot-noise and coherent optical processing with the evaluation of upper bound on quantum Fisher information was discussed in [39]. Another alternative scheme called superlocalization by image inversion interferometry (SLIVER) was suggested by the same research group [40, 41].

In further theoretical works [42], the generalized application of QCRLB was propounded. In [43], the calculation of one-dimensional separation of thermal sources of arbitrary strength

using the Gaussian-state model was accomplished with a proposal of modified SPADE and SILVER methods. Lupo and Pirandola [44], studied the application of arbitrary quantum states as a source pair and introduced the optimal entangled states for sub-Rayleigh imaging. In [45], the authors developed a general mechanism to acquire an optimal set of optical modes with respect to the used PSF.

These distinctive studies opened a new avenue to enhance the localization precision and separation estimation for linear optical systems examining one or two close incoherent sources. Nevertheless, the application potential in other associated optical areas is possible. Shortly after the publication of these results, the first experimental realizations appeared.

One of the first experimental realization inspired by SPADE method was performed by Paúr et al. [1]. Here, the authors developed and demonstrated an optimal measurement technique using digital holography setup and Gaussian-state model, confirming the strong violation of the Rayleigh criterion. This result is a part of this thesis and is comprehensively analyzed in Chapter 4.

At the same time, other resembling experiments were realized by other groups. Tham et al. [46] performed another two-point superresolution method called super-resolved position localization by inversion of coherence along an edge (SPLICE), with the application of parity sensitive interferometers. Furthermore, Tsang et al. [47] implemented a self-interference technique based on image inversion interferometry and Yang et al. [48] applied a heterodyne detection scheme to microscopy-related tasks.

More insight can be obtained from the perspective of space-time duality of light. As this already provides valuable tools in classical time-frequency measurements [49, 50], the adaptation of these techniques into metrology analysis in the time-frequency domain is adequate. In a letter, Donohue et al. [51] demonstrated the experimental realization of separation estimation on the incoherent mixture of shaped ultrafast optical pulses. This measurement was performed in both temporal and spectral regime, using the mode-selective method facilitated by wave-guided nonlinear interactions and single-photon detection. They validated sub-pulse-width separations with precision well below the standard CRLB.

The most general quantum extension of classical CRLB is the Holevo bound [52, 53]. This bound circumscribes the best lower bound among all existing lower bounds for the variance of unbiased estimators of any family of state. The saturation of the Holevo bound was investigated for systems in the pure states [54] or in the subject of multi-parameter estimation [53, 55]. Further, Yamagata et al. [56] addressed the attainability in the context of the local scenario, where the bound can be saturated only if the estimator satisfies certain regularity conditions. Unfortunately, the optimal estimators generally depend on the true parameter which limits their practical interest or requires adaptive measurement strategies.

Direct detection and enhancement of standard Fisher information

Despite of the results of the quantum Fisher information, the demonstrated proof-of-concept experiments require sophisticated accessories, increasing the complexity of typical experimental setups. This hints at the revision of the scenario of direct imaging, and the potential enhancement of classical Fisher information. Paúr et al. [2] analyzed this problem and surprisingly revealed, that application of a simple phase mask, i.e., signum filter, makes the decay of the Fisher information linear, instead of quadratic. Utilization of such non-absorbing spatial filter is equivalent to the well-known Hilbert transform and generation of information-rich zero intensity region in the center of final PSF, which encompasses the majority of Fisher information.

This idea of isolated zero regions was experimentally extended by the same scientific group in two spectroscopic setups for resolving natural or artificially created spectral doublets [45]. They validated the significant contribution from these zero intensity regions and also linear scaling of resulting Fisher information for rectangular apertures and Sinc PSF.

These results imply, that the superiority of the above-mentioned quantum schemes with separation-independent Fisher information over classical techniques is smaller than previously assumed. This works are a part of this thesis and are extensively resolved in Chapters 5 and 6.

Axial superresolution

Another field potentially benefiting from superresolution methods is optical microscopy. Here again, for any optical microscope the essential metric is spatial resolution. The maximum resolution is commonly defined in terms of the Abbe-Rayleigh criterion [57]. Let us stress, this classical criterion is based on the same heuristic arguments as the above mentioned two-point resolution criteria and may fail in the state of art of the digital imaging techniques.

In recent years, several methods have been proposed for superresolution microscopy [58, 59] with the capability to improve resolution by more than one magnitude with respect to the diffraction limit. The important class of these techniques includes the fluorescence microscopy [29, 60–62], with widely used approach of gradually activated fluorescent molecules ensuring the localization precision around tens of nanometers. Another frequently used method is stimulated emission depletion (STED) microscopy [63, 64] and reversible saturable optically linear fluorescence transitions (RESOLFTs) [65].

Many other methods are concentrated on the realization of axial super-localization, which is crucial mainly for three-dimensional optical systems. For example, methods relying on precise localization of single point sources, such as interferometric microscope [66,

67], PSF engineering [68–70], and multi-plane detection schemes [71–73] belong here.

A related challenge is to determine an imperceptible axial separation of two radiating incoherent point sources. This objective was successfully verified by Zhou et al. [74] inspired by the spatial mode demultiplexing method. They theoretically and experimentally demonstrated the application of the lossless Laguerre-Gaussian radial mode sorter reaching the QCRLB for arbitrarily small axial separations. Unlike previously mentioned superresolution schemes, this design does not require sophisticated stabilization nor consecutive fluorophores activation. Moreover, the performed experimental setup can be simply adapted to the axial localization of a single point source.

Simultaneously with the aforementioned research, Řeháček et al. [4] addressed this question from a different perspective. They focused on a single-point axial localization based on the direct imaging method. They found optimal measurement, that strikingly achieved the quantum limits with a single intensity scan while the CCD camera was placed in one of two optimal transverse detection planes. The theory was verified with a simple microscopic layout, bringing the axial resolution up to dozens of nanometers, and revealing the redundancy in adopting more complicated detection schemes. This work, as a part of this thesis, will be discussed in more detail in Chapter 7.

Multi-parameter quantum estimation

Up to now, we have focused on the estimation of one parameter, typically separation. The key feature of these techniques lies in phase-sensitive measurements implementing mode projections or linear transformation of the measured signal. This requires highly symmetric PSFs and configurations with equally bright point sources. The more realistic scenario of unequally bright sources and asymmetric peaks involves the simultaneous estimation of separation, centroid, and intensities. This multi-parameter estimation brings about a trade-off in how precisely different parameters can be estimated. When the estimation procedure is tuned for a specific parameter, the precision can deteriorate for the remaining ones.

Řeháček et al. [75] showed that unbalanced intensity in the estimation process tends to make the Fisher information smaller and vanishing for zero separation. Strictly speaking, the previous concepts are not robust with respect to the lack of information about the other parameters. Nevertheless, the available information in the optimal scheme still overwhelms conventional direct imaging schemes. On top of this, the authors also formulated the quantum Fisher information matrix (QFIM) [76, 77], as a central quantity for multi-parameter strategy, which clearly shows the interplay between various estimation parameters. For example, for equally bright sources, the QFIM for the spacing parameter is reduced into the form of constant Fisher information which coincides with previous outcomes. This

particular physical situation is singular and embodies anomalous features. This matrix circumscribes the generalized complex analysis of the ultimate precision bounds suggesting the possible application in observational astronomy, where the binary stars have typically small angular separations with large differences in their brightness.

Other multi-parameter estimation task was considered in related context by Ang et al. in [78]. The authors addressed the problem of two-dimensional resolution, i.e., entire transverse-plane localization, adopting the preceding weak-source model. They obtained the full four-parameter quantum Fisher information matrix describing the ultimate precision for estimaton of the transverse Cartesian components of the centroid and separation of two incoherent point sources. They also outlined and analyzed two measurement schemes — the extended versions of SLIVER and SPADE methods via Monte Carlo simulations, verifying mean square error (MSE) no larger than twice the predicted quantum limits.

Two-point resolution with presence of coherence

Additional straightforward extension of two-point resolution is the consideration of the effect of partial coherence. Within the early advancement of the optical coherence theory, it was established that both the magnitude and the phase of the degree of partial coherence substitute prominent parts in designating image intensity distribution and its statistical attributes [79–82]. It was shown, that for direct measurement schemes, a larger degree of coherence implies the better resolution. Contrariwise, in classical estimation theory the coherence effectively lowers the estimation precision. This contradiction is intensified when the resultant optical field is generated by correlated point sources [83, 84].

From the quantum point of view, it is important to find out, whether the quantum precision bounds are also lowered in the presence of this optical property. This task was deeply investigated by Larson and Saleh [85]. In this article, the authors reformulated this problem as a multi-parameter estimation of the separation and the degree of coherence. They showed, that quantum precision bound of the separation drops to zero even at a very small (nonzero) degree of coherence, which would mean the vulnerability of violation of Rayleigh's curse for incoherent sources for any small positive or negative correlation between them. Moreover, the theoretical results reflected that even when the degree of coherence is known and negative, the curse remains, while for positive correlations the curse could be broken.

Almost immediately, these results triggered discussions about the correctness of the announced results. Tsang and Nair [86] questioned Larson's and Saleh's calculations and showed that their statements have fundamental deficiencies. They pointed out that Fisher information of spatial-mode demultiplexing measurement can surpass Rayleigh's curse for

any value of the degree of coherence below 1, and even predicted higher sensitivity as long as the degree of coherence stays negative. The other handled problem is the used quantum model and corresponding normalization of the photon density operator in the computation of the quantum Fisher information.

Naturally, Larson and Saleh quickly replied to this comment [87] and tried to vindicate their findings with their reference to an inconsistency in the Tsang and Nair model itself. Indeed, after the proper reformulation, authors obtained the analogous violation of Rayleigh's curse as in the Tsang and Nair model with a difference in the rate of predicted sensitivity and in a case of fully coherent case. This different behavior was inflicted by the inappropriate normalization in Tsang-Nair model.

In the latter proposals, the non-uniformity of used quantum models and their normalization factors conducted the misleading conclusions and did not reach the adequate consensus. Despite of these arguments, very recent research of Hradil et al. [88] tried to explain the reasons for these misunderstandings by basic physical arguments and definite calculations for a fundamental model of a coherent superposition. It was found that, when the coherence effects are taken into consideration, the resulting Fisher information itself is no longer a meaningful measure of precision because the channels exhibiting interference are not equivalent in terms of the signal strength. When the quantum Fisher information is properly normalized by the number of detecting particles, there is no advantage of coherent sources over the incoherent ones. Moreover, for the partially coherence case, the correctly weighed quantum Fisher information is always limited by the incoherent superposition.

Non-diffracting beams

Diffraction, as a universal optical phenomena, is inherently connected to the wave nature of light. It influences all classical wave fields and arises when a wave impinges on a solid obstruction or passes through an aperture. Within this, the wave amplitude or phase can be modified and the remaining parts of the wavefront extending beyond exhibit the diffraction pattern. Concurrently, any beam-like field should also undergo diffractive spreading through its free space propagation. A nice example is a propagation of the Gaussian beam, where the beam diameter spreads, as a subject of the diffraction, undergoes a divergence. The characteristic parameter which describes the spread of the Gaussian beam as well as the distance, where the cross-section increase by a factor of 2, is the well-known Rayleigh range.

Amazingly, there exist exact free-space solutions of the scalar-wave equation that are *diffraction-free*. These solutions are non-singular with infinite energy and can have sharply

defined intensity patterns in each transverse plane, independent of propagation distance. One of the non-diffracting field, which has an axial symmetry, is proportional to zero-order Bessel function of the first kind, typically called "Bessel" or "Bessel-type" beam. The utilized Bessel function mathematically leads to the cross-sectional profile of concentric rings, where over an infinite area can be an infinite number of these rings and carry infinite power. Naturally, any realization of such beams in a laboratory needs to be limited by a finite aperture, which leads to an approximation (a quasi-Bessel beam) with altered mathematical properties.

The first mathematical construction of Bessel beams was presented by Durin [89] in the late eighties of the last century. The initial experimental implementation was realized soon after by Durin et al. [90]. Authors utilized the fact that the Fourier spectrum of the Bessel beam is a conical superposition of plane waves that manifests itself as a ring of infinitesimal thickness. So they simply placed a solid annular slit in the back focal plane of a thin spherical lens to form the beam. However, this method is heavily inefficient, as the majority of the incident field is obstructed by the annulus [91, 92]. This concept was rather controversial and scientists linked the results to the line images [93, 94] or Poisson's spot [95].

The Bessel beam may also be created by using an axicon [96] or conical lens, which provides the conical superposition of the wave in free space [97]. The use of an axicon allows a higher efficiency in generation than with the annular slit as it processes the whole or majority of the incident field. Also, this approach helps to remove the rapid on-axis intensity oscillations associated with slit but the beams still exist only in the focal region of the conical lens, exceeding only a few centimeters. There exist other cost-effective methods of generation of Bessel beams, including spatial light modulators [98–101] or Fabry-Perot cavity [97, 102].

Self-healing property

Besides the capability of propagating without changing the intensity profile, there exists other interesting property of Bessel beams, namely the self-healing ability [103]. This self-reconstruction mechanism allows beams to fully reconstruct their intensity profile after encountering an obstacle during propagation. These two remarkable traits attracted prominent interest in the last four decades and have been more extensively investigated in [104, 105].

Especially the self-healing effect was found to be very helpful in various applications, such as optical particle manipulation by optical tweezers [106–108] using the technique of optical gradient force trap, microscopy [109, 110] and light-sheet microscopy [111, 112]

with simultaneous improvement of image quality and contrast, quantum communication [113] based on self-healing capacity of entangled photon pairs, material processing [114] using in laser-based processing, and more others. Additionally, the class of superposition Bessel beams was applied for the generation of helicon beams [115, 116], conveyor beams [117, 118], or general self-accelerating beams [119, 120]. Thanks to their outstanding self-healing capabilities, Bessel beams found their indispensable role in free-space satellite communication, mainly in long-range communication through turbulent media [121, 122].

Even though the self-reconstructing beams had been the spotlight of many research studies, the deeper understanding of self-healing behavior was missing. It was studied mainly numerically [123, 124], but several analytical investigations based on Gaussian optics [125, 126] had been presented in the last decade. These analytical notions suffered from unavailability to express the minimum reconstruction distance, where this crucial parameter was previously determined based on geometric arguments only.

This drawback was successfully removed by Aiello et al. [127] by submitting full wave-optics characterization of self-reconstruction process. Their approach allows easy computation of minimum reconstruction distance based on robust physical arguments. In addition, using well-known Babinet principle [128], authors exposed that the self-healing mechanism can be compared with elementary propagation of plane wave via the aperture.

Furthermore, Aiello et al. [5] showed that the above-mentioned wave-optics description extends the concept of self-reconstruction to almost any kind of beam. They introduced a novel definition of minimum reconstruction distance and metric which quantifies the similarity between the perturbed and the unperturbed beams. These theoretical predictions were experimentally verified with the Gaussian beam by measuring the whole complex amplitude of the field. This work is a part of this thesis and is discussed in Chapter 8.

The research complementing previous approaches was presented by Arrizon et al. [129]. The authors reformulated the analysis of the self-healing of a partially obstructed optical beam by decomposition of the obstructed field into two mutually orthogonal components, one of the exact copy of attenuated original beam and second as a distorted version of the field. They established a more comprehensive quantitative measure of the beam damage and degree of self-healing which provides the overall description and characterization of this phenomenon.

Very recently, Vetter et al. [130] proposed a new approach for generating a long-distance Bessel beams based on a newly-manufactured ring-shape (annular) lens. This light evolution method brings about diffraction-free propagation over several meters and presents strong self-healing capacity against opaque and non-opaque scatterers. Beyond these significant improvements, authors successfully manifested the realization of the longest optical conveyor and helicon beam in history.

Chapter 3

Methods and Tools

This chapter encompasses a brief overview of main theoretical tools and important experimental devices related to this thesis. Cardinal results are concerned with the classical two-point resolution problem from the viewpoint of statistical estimation and quantum theory. Each experiment requires specific measuring scheme and numerical data processing, explained in detail in individual chapters. Nevertheless, the background framework is universal across all discussed problems, namely Rayleigh's criterion, classical and quantum Fisher information and application of spatial light modulators.

3.1 Rayleigh's criterion

Rayleigh's criterion is one of the most often used quality factors for two-point resolution, i.e., the ability of an optical system to resolve two closely spaced point sources. It has been generally applied to microscopy or astronomical applications, where it has a simple implementation and definition. The well known notation of this criterion reads that two incoherent point sources are "*barely resolved*" by a diffraction-limited optical system with a circular aperture when the center of the Airy intensity pattern generated by one point source falls precisely on the first zero of the Airy disk generated by the second source [83].

3.1.1 Circular aperture

The Airy disk represents the intensity distribution of the Fraunhofer diffraction pattern generated by a uniformly irradiated circular aperture of radius w. The circular symmetry suggests that the Fourier transform describing the Fraunhofer diffraction can be rewritten to the form of Fourier-Bessel or Hankel transform [131, 132]. The resulting image plane

amplitude distribution is defined as

$$U(r) = e^{ikf} e^{i\frac{kr^2}{2f}} \frac{\pi w^2}{i\lambda f} \left(2\frac{J_1(kwr/f)}{kwr/f} \right), \tag{3.1}$$

where k is a wave number, r is a radius coordinate in the observation plane, f is an effective focal length of optical system and J_1 is the Bessel function of the first kind. The associated Airy pattern is then given as

$$I(r) = |U(r)|^2 = \left(\frac{\pi w^2}{\lambda f} \right)^2 \left(2\frac{J_1(kwr/f)}{kwr/f} \right)^2. \tag{3.2}$$

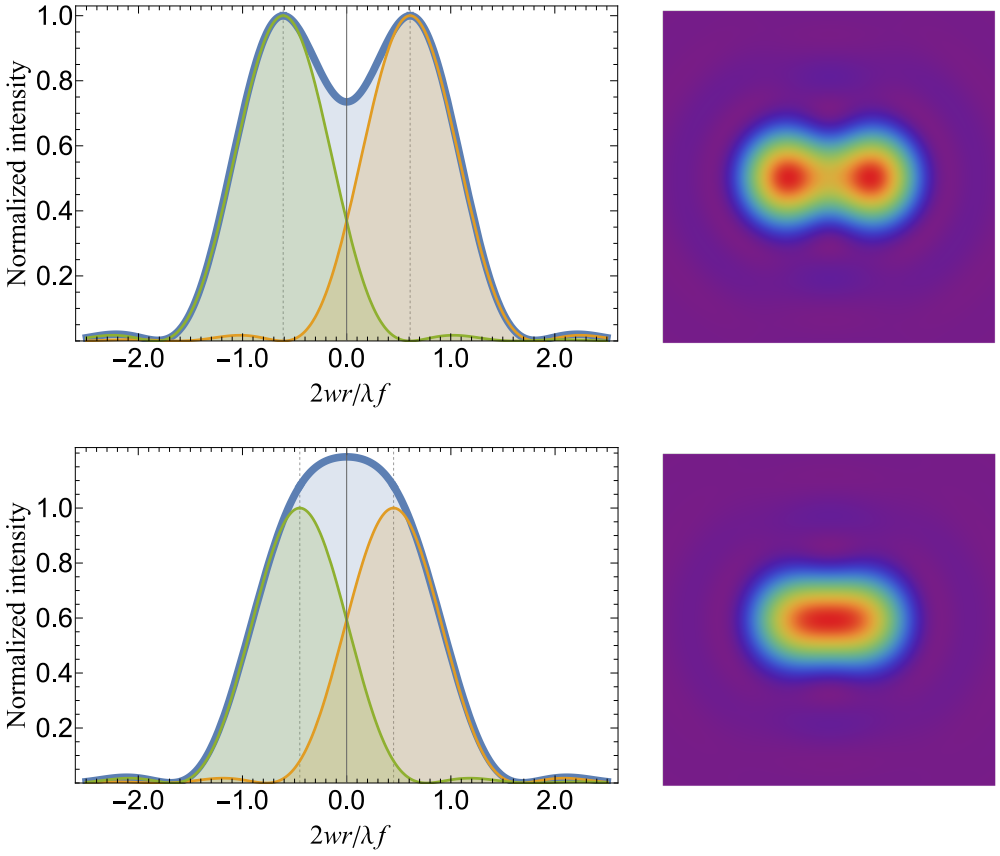

Figure 3.1: Rayleigh's criterion for incoherent imaging of two point sources using a circular aperture. Cross-section plots (left) and density plots (right) of the image intensity distributions are depicted for two different object separations. The left graphs show the combined intensity pattern of two sources (blue) and individual single-point intensities (green, orange) for "resolved" sources (top) and "unresolved" sources below the resolution limit (bottom). The vertical gray dotted lines indicate the centroids of each point spread function. Right density plots show 2D equivalents of these two cases.

The width of the central lobe of this Airy disk is given by

$$d_A = \frac{0.61\lambda}{NA} = \frac{1.22\lambda f}{w}, \tag{3.3}$$

where the *NA* is a numerical aperture of the optical system. Simultaneously, this mathematically defines the Rayleigh's criterion minimum resolvable distance between point sources. Figure 3.1 shows the cross-sections and density plots of intensity distributions of two equally bright incoherent point sources separated by the Rayleigh distance and the *"unresolvable"* distance below this value. In the case of Rayleigh resolution distance, the central zone falls about 27 % below the peak intensity. For comparison, the other conventional resolution criteria are defined as follows - Sparrow limit $0.47\lambda/NA$, Abbe limit $0.5\lambda/NA$ and axial Abbe limit $2\lambda/NA^2$ [133].

In the case of coherent illumination, the corresponding image intensity distribution relies on the phase distribution associated with both point sources as

$$I(r) \approx \left| \left(2\frac{J_1(kw(r-\frac{\mathfrak{s}}{2})/f)}{kw(r-\frac{\mathfrak{s}}{2})/f} \right) + e^{i\phi} \left(2\frac{J_1(kw(r+\frac{\mathfrak{s}}{2})/f)}{kw(r+\frac{\mathfrak{s}}{2})/f} \right) \right|^2, \tag{3.4}$$

where ϕ is the relative phase difference between the two point sources and $\mathfrak{s}$ is the displacement of each point relative to the optical axis. Figure 3.2 shows the cross-sections and appropriate density plots of intensity distributions for in-phase ($\phi = 0$ rad), quadrature ($\phi = \pi/2$ rad) and anti-phase ($\phi = \pi$ rad) values. When the points are in quadrature, the intensity distribution characterized by a slight dip is identical to that resulting in incoherent case. For the in-phase variant, the points merge into one peak making the resolution of two points more difficult than for incoherent illumination. On the other hand, for anti-phase situation the central peak vanishes, making the resolution easier [83].

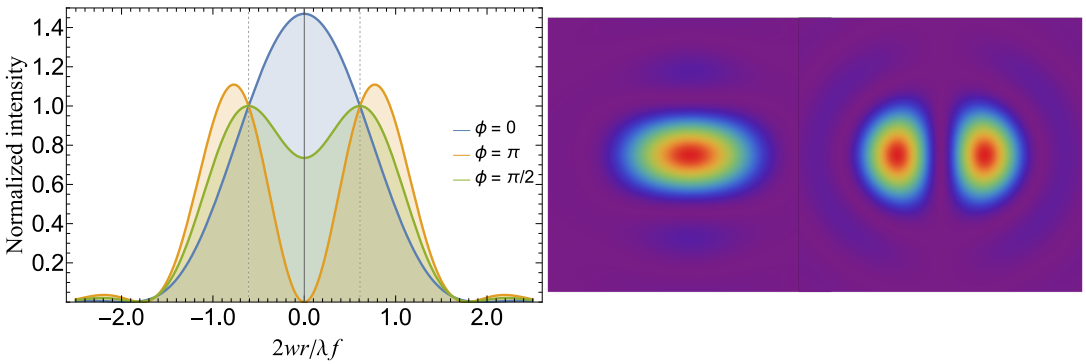

Figure 3.2: Cross-section of image intensities for two coherent point sources separated by Rayleigh distance with the phase differences for values $\phi = 0, \pi$ and $\pi/2$ (left). 2D Density plots for $\phi = 0$ and π (right).

3.1.2 Rectangular aperture

Another typical shape of optical apertures is a rectangle, mostly used in spectroscopic devices. The transmittance function of this aperture is given by

$$t_A(x,y) = \text{rect}(\frac{x}{2w_x})\text{rect}(\frac{y}{2w_y}), \tag{3.5}$$

where the constants w_x and w_y are the half-widths along x and y axes. In the Fraunhofer diffraction regime again, the resulting image complex amplitude can be found as

$$U(x,y) = e^{ikf} e^{i\frac{k(x^2+y^2)}{2f}} \frac{4w_x w_y}{i\lambda f} sinc(\frac{kw_x x}{f}) sinc(\frac{kw_y y}{f}), \tag{3.6}$$

with intensity distribution

$$I(r) = \left(\frac{4w_x w_y}{\lambda f}\right)^2 sinc^2(\frac{2\pi w_x x}{\lambda f}) sinc^2(\frac{2\pi w_y y}{\lambda f}). \tag{3.7}$$

In this case, the transverse width of the central lobe of diffraction pattern is defined as

$$d_r = \frac{\lambda f}{w_x}. \tag{3.8}$$

Figure 3.3 shows a 1D cross-section plot and 2D density plot for two incoherent point sources using a rectangular aperture. Points are separated according to the definition of Rayleigh criterion for circular aperture (maximum of one point lies in a minimum of the second point). In this situation, the central dip falls about 18.9% of peak intensity [134].

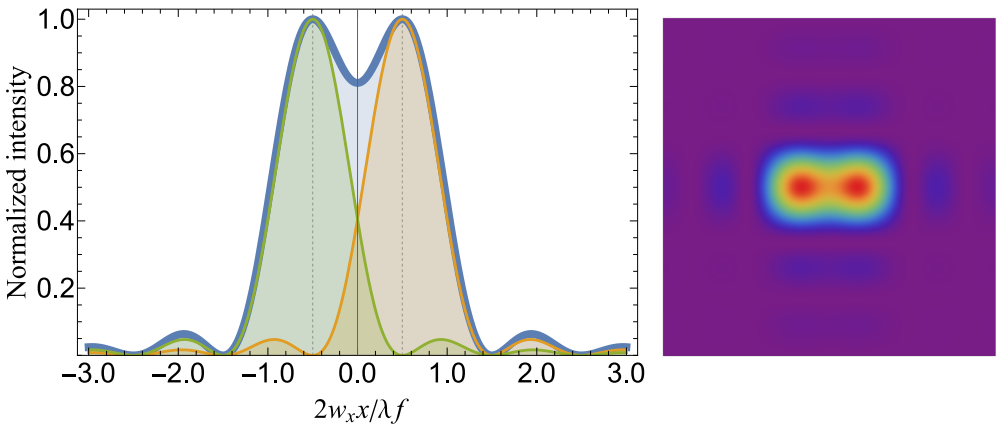

Figure 3.3: Rayleigh's criterion for incoherent imaging of two point sources using rectangular aperture. Graphs show two point sources separated by Rayleigh limiting distance. This leads to central intensity drop of about 18.9 %.

3.2 Parameter estimation in signal processing

Estimation theory as an important section of mathematical statistics and information theory deals with the problem of extracting true values of parameters of interest $\theta_1, \theta_2, ...\theta_m$ by inspecting measured data sets with a random component. Any method focused on the determination of these quantities usually leads to indirect measurements and involves an optimization procedure to identify the most accurate estimator. In this sub-chapter, we present a summary of methods comprising the classical Cramér-Rao bound with associated Fisher information and their quantum counterparts. For more details about classical estimation methods refer to [30, 135–137] and to [33, 52, 76, 138] for their quantum alternatives.

Classical estimation theory

Mathematically, we can consider that each measured N-point data set is in the form $x_m[n] = \{x[0], x[1], ..., x[N-1]\}$, which depends on the unknown parameter through the underlying physics in a way that its values influence the expected measurements results. To determine the true value of θ, it is convenient to deduce an estimator as

$$\hat{\theta}(x) = g(x[0], x[1], ..., x[N-1]), \tag{3.9}$$

where g is some function. The estimator may be thought as a rule that attributes the value of θ for each realization of x_m. Generally, the estimator may depend on other parameters. If these are unknown as well, we end up with the situation of a multi-parameter estimation problem, which complicates the estimation process more and causes some trade-off between estimation accuracy of estimated parameters.

To design an efficient estimator, it is reasonable to mathematically model the data by θ-parameterized (conditional) probability density function (PDF) $p(x;\theta)$, respecting its inherent random nature. This conditional probability denotes the probability of measuring the value x when the parameter takes the value θ. The right selection of PDF, consistent with the given physical constraints, leads to better estimation performance.

Owing to the existence of noise, any such estimator $\hat{\theta}(x)$ always embodies some statistical uncertainty $\Delta\hat{\theta}(x)$. This uncertainty restricts the searching to the class of estimators performing the lowest variability. There might be different estimators based on different statistics for the broad class of unbiased estimators, but we look for one that is uniformly the best with minimum variance for the whole set of parameters and the full range of its values. The notion "unbiased" means that the estimator achieves the true value of the sought

parameter on average. Mathematically, an unbiased estimator is defined as

$$E(\hat{\theta}) = \int \hat{\theta}(x)p(x;\theta)dx = \theta \qquad a < \theta < b, \tag{3.10}$$

where (a, b) denotes the range of possible values of θ, typically restricted by physical limits. Contrariwise, the biased estimators are characterized by a systematic error (bias). This bias can cause the deterioration of the estimation process.

3.2.1 Mean square error and minimum variance unbiased estimator

To quantify the estimator efficiency, it is necessary to select some robust metric. Naturally, simplest one is the mean square error (MSE) defined as

$$MSE(\hat{\theta}) = E\left[(\hat{\theta} - \theta)^2\right]. \tag{3.11}$$

This measures the average mean squared deviation of the estimator from its true value. To clarify the importance of this metric, we can rewrite the definition (3.11) into the more suitable form as

$$\begin{aligned} MSE(\hat{\theta}) &= E\left[\left(\hat{\theta} - E[\hat{\theta}] + E[\hat{\theta}] - \theta\right)^2\right] \\ &= E\left[\left(\hat{\theta} - E[\hat{\theta}]\right)^2\right] + \left(E[\hat{\theta}] - \theta\right)^2 \\ &= \mathrm{Var}(\hat{\theta}) + b^2(\hat{\theta}), \end{aligned} \tag{3.12}$$

where $\mathrm{Var}(\hat{\theta}) = E[\hat{\theta}^2] - E[\hat{\theta}]^2$ means variance of estimator and b is a bias. This directly shows that the MSE is the sum of the estimator variance and a bias factor. Therefore, this metric cannot be solely considered as sufficient criterion because the dependence on the bias can leads to the unsuitable estimators. On the other hand, the MSE can still be used for finding the optimal estimator. An intuitive choice is to constrain the bias to zero $b(\hat{\theta}) = 0$ and look for one which can minimize the variance. Such an estimator is termed as the minimum variance unbiased (MVU) estimator with mean square error equal only to its variance.

3.2.2 Fisher information and Cramér-Rao lower bound

Generally, there is no guarantee that the MVU estimator does always exist and provides minimum variance for all values of the searched parameter θ. If the minimum variance unbiased estimator exists, we may not be able to find it. However, there exist several ways

to find the optimal MVU estimator, of which the determination of the Cramér-Rao lower bound (CRLB) is the most used one. Simply, the CRLB determines that the variance for any unbiased estimator is greater than or equal to a given value. Then the unbiased estimator, whose variance for each value of the unknown parameter attains the CRLB, has to be the MVU estimator.

Since all our knowledge is incorporated in the measured data and corresponding PDF, it is intuitive that the estimation accuracy depends directly on the PDF. In general, the more the PDF is affected by the θ, the better estimates we get. For the computation of CRLB, it is important to assume that the $p(x;\theta)$ satisfies the regularity condition

$$E\left[\frac{\partial \ln p(x;\theta)}{\partial \theta}\right] = 0, \tag{3.13}$$

where the partial derivative, with respect to the θ of the natural logarithm of the likelihood function, is called *score*. Then, the variance of any unbiased estimator $\hat{\theta}$ must satisfy

$$\mathrm{Var}(\hat{\theta}) \geq \frac{1}{E\left[\left(\frac{\partial \ln p(x;\theta)}{\partial \theta}\right)^2\right]}, \tag{3.14}$$

where the denominator is known as the Fisher information $\mathcal{F}_{std}(\theta)$, i.e., the variance of the score. The Fisher information is a typical method how to determine the total amount of information that measured random data carries about the unknown parameter θ.

The CRLB given by (3.14) may also be written as

$$\mathrm{Var}(\hat{\theta}) \geq \frac{1}{-E\left[\frac{\partial^2 \ln p(x;\theta)}{\partial \theta^2}\right]}, \tag{3.15}$$

which is true only if the $\ln p(x;\theta)$ is twice differentiable with respect to θ. Accordingly, optimal MVU estimators $\hat{\theta} = g(x)$ are those saturating the Cramér-Rao inequality and may be found only if they fulfill

$$\frac{\partial \ln p(x;\theta)}{\partial \theta} = \mathcal{F}_{std}(\theta)(g(x) - \theta). \tag{3.16}$$

Lastly, it is important to note that the above results of CRLB and related FI stand only for one independent measured sample $p(x[n];\theta)$. So for N samples, we get Var $\leq 1/(N\mathcal{F}_{std}(\theta))$.

Quantum estimation theory

A similar approach is applied in quantum-mechanical systems as well. There are also many quantities that are not directly measurable which can be caused either fundamentally or due to experimental limitations. Typical examples are purity or entanglement, which are defined as nonlinear functions of the quantum density matrix and cannot be to the regular quantum observables. The solution can be found using quantum estimation theory and its analytical tools which seeks the optimal strategy for estimating parameters of the density operator of quantum systems.

These tools provide options for discovering suitable positive-operator valued measurement (POVM). One can find optimal POVM minimizing a suitable cost function averaged over all feasible parameter values or look for the POVM maximizing the Fisher information and consequently minimizing the variance of the estimator for specific fixed value. Moreover, the results can be applied to find the optimal estimators assuring the attainability of the ultimate bounds on precision. Here, we are interested in the determination of the optimal quantum estimator in terms of symmetric logarithmic derivative as well as the ultimate bounds in terms of quantum Fisher information with an explicit solution for systems determined by pure states.

An ordinary quantum statistical model is represented by the density operator ϱ, which ensures the calculation of probability for any outcome of a well-defined measurement on the quantum system. The density matrices are build from state vectors and can be generally expressed in their eigenbasis form

$$\varrho = \sum_n p_n \left|\psi_n\right\rangle \left\langle\psi_n\right|, \tag{3.17}$$

which relates to the mixed state with probability p_n that the system is in the pure state $|\psi_n\rangle$. Also, according to the Born rule, the classical probability function $p(x;\theta)$ can be expressed by the density operator as

$$p(x;\theta) = \mathrm{Tr}[\varrho_\theta \Pi_x], \tag{3.18}$$

where Π_x are elements of POVM satisfying $\int \Pi_x dx = \mathbb{I}$, ϱ_θ is density operator parametrized by the estimated parameter and Tr is a matrix trace operation.

Recalling the classical Cramér-Rao inequality from Eqs. (3.14) and (3.15), the Fisher information corresponds to the formula

$$\mathcal{F}_{std}(\theta) = \int_{-\infty}^{\infty} \left(\frac{\partial \ln p(x;\theta)}{\partial\theta}\right)^2 p(x;\theta)dx = \int_{-\infty}^{\infty} \left(\frac{\partial p(x;\theta)}{\partial\theta}\right)^2 \frac{1}{p(x;\theta)}dx, \tag{3.19}$$

which denotes the necessity to differentiate the PDF of the data. This means that we must likewise differentiate the density operator. Generally, there exist two principal ways - symmetric logarithmic derivative (SLD) or right logarithmic derivative (RLD). In fact, the RLD operator may not always exist for systems described by the pure states or need to satisfy strict mathematical conditions with less informative solutions than the symmetric logarithmic derivative operator. On the other hand, the bounds given by the RLD operator are inferior (lower) than the bounds given by SLD operator and are more suitable for multi-parameter estimation scenarios. In general, the application of an SLD operator is more informative and suitable for one-parameter schemes and therefore for this thesis.

The symmetric logarithmic derivative L_θ is the self-adjoint Hermitian operator satisfying the equation

$$\frac{\partial \varrho_\theta}{\partial \theta} = \frac{L_\theta \varrho_\theta + \varrho_\theta L_\theta}{2}. \tag{3.20}$$

Hence, the derivative of probability density function can be written as

$$\partial_\theta p(x;\theta) = \mathrm{Tr}\left[\partial_\theta \varrho_\theta \Pi_x\right] = \mathrm{Re}\left(\mathrm{Tr}\left[\varrho_\theta L_\theta \Pi_x\right]\right). \tag{3.21}$$

Consequently, the classical Fisher information can be reformulated into

$$\mathcal{F}_{std}(\theta) = \int_{-\infty}^{\infty} \frac{\mathrm{Re}\left(\mathrm{Tr}\left[\varrho_\theta L_\theta \Pi_x\right]\right)^2}{\mathrm{Tr}\left[\varrho_\theta \Pi_x\right]} dx. \tag{3.22}$$

3.2.3 Quantum Fisher information and quantum Cramér-Rao lower bound

The classical bounds following a given POVM Π_x from Eq. (3.22) should be achieved by proper data processing. The typical example is the maximum-likelihood estimator which provides an asymptotical saturation of these bounds for most measurements. In the case of reaching the ultimate bounds, we need to maximize the Fisher information over all possible POVM. By assuming the Eq. (3.21) and application of the Cauchy-Schwartz inequality $\left|\mathrm{Tr}\left[X^\dagger Y\right]\right|^2 \leq \mathrm{Tr}\left[X^\dagger X\right] \mathrm{Tr}\left[Y^\dagger Y\right]$, the maximized Fisher information reduces to the formula

$$\mathcal{F}_{std}(\theta) \leq \left| \int_{-\infty}^{\infty} \frac{\mathrm{Tr}\left[\varrho_\theta L_\theta \Pi_x\right]}{\sqrt{\mathrm{Tr}\left[\varrho_\theta \Pi_x\right]}} \right|^2 dx \leq \int_{-\infty}^{\infty} \mathrm{Tr}\left[L_\theta \varrho_\theta L_\theta \Pi_x\right] = \mathrm{Tr}\left[\varrho_\theta L_\theta^2\right]. \tag{3.23}$$

These inequalities determine that the classical Fisher information of any quantum measurement is always constrained by the quantum Fisher information quantity

$$\mathcal{F}_{std}(\theta) \leq \mathcal{F}(\theta) \equiv \mathrm{Tr}\left[\varrho_\theta L_\theta^2\right] = \mathrm{Tr}\left[\partial_\theta \varrho_\theta L_\theta\right]. \tag{3.24}$$

This also defines the quantum Cramér- lower bound for variance of any unbiased estimator

$$\mathrm{Var}(\hat{\theta}) \leq \frac{1}{N\mathcal{F}(\theta)}, \tag{3.25}$$

where N again stands for the number of observations of independent identical systems.

The general solution for SLD operator may be expressed in continuous form

$$L_\theta = 2\int_0^\infty \exp\{-\varrho_\theta t\}\partial_\theta \varrho_\theta \exp\{-\varrho_\theta t\}, \tag{3.26}$$

or in a more convenient representation of diagonal density operator (Eq. (3.17))

$$L_\theta = 2\sum_m \sum_n \frac{\langle\psi_n| \frac{\partial \varrho_\theta}{\partial\theta} |\psi_m\rangle}{\varrho_m + \varrho_n} |\psi_n\rangle \langle\psi_m| \tag{3.27}$$

where the sums include only terms with eigenvalues $\varrho_n + \varrho_m \neq 0$. The generic solution of quantum Fisher information by substituting the Eq. (3.27) into Eq. (3.24) can be finally expressed as

$$\mathcal{F}(\theta) = 2\sum_m \sum_n \frac{\left|\langle\psi_n| \frac{\partial \varrho_\theta}{\partial\theta} |\psi_m\rangle\right|^2}{\varrho_m + \varrho_n}. \tag{3.28}$$

The QCRLB affords ultimate bounds that rely only on the structure of the quantum statistical model and not on the measurement itself. Thus the optimal POVM saturating this ultimate bounds is called *efficient* and the intrinsic form of optimal quantum estimator holds

$$\hat{\theta}_{\mathcal{O}} = \theta\mathbb{I} + \frac{L_\theta}{\mathcal{F}(\theta)}, \tag{3.29}$$

using the fact that $\mathrm{Tr}\left[\varrho_\theta L_\theta\right] = 0$.

3.2.4 Quantum Fisher information for pure state model

When the state of quantum system for all values of the parameter θ is pure, the density operator abbreviates to the form

$$\varrho_\theta = |\psi(\theta)\rangle \langle\psi(\theta)|. \tag{3.30}$$

Equivalently, the quantum Fisher information can be computed directly

$$\mathcal{F}(\theta) = \mathrm{Tr}\left[\varrho_\theta \left(\partial \varrho_\theta\right)^2\right] = 4 \left\langle \psi(\theta)\right| \left(\frac{\partial \varrho_\theta}{\partial \theta}\right)^2 \left|\psi(\theta)\right\rangle , \tag{3.31}$$

where the eigenvalue ϱ and eigenvectors $|\psi(\theta)\rangle$ depend on the parameter of interest. For this instance, the derivation of the density matrix stands as

$$\frac{\partial \varrho_\theta}{\partial \theta} = \left|\partial_\theta \psi(\theta)\right\rangle \left\langle \psi(\theta)\right| + \left|\psi(\theta)\right\rangle \left\langle \partial_\theta \psi(\theta)\right| . \tag{3.32}$$

After straightforward but lengthy calculations the quantum Fisher information tends to the simple result to

$$\mathcal{F}(\theta) = 4 \left[\langle \partial\psi(\theta)|\partial\psi(\theta)\rangle - |\langle \psi(\theta)|\partial\psi(\theta)\rangle|^2\right] . \tag{3.33}$$

3.3 Spatial light modulators

Spatial light modulation as a key technology has wide-spread applications ranging from microdisplays projection, three-dimensional (3D) printing, and augmented reality to lithography and metrology with implementation in quantum and adaptive optical systems. Over the past decades, the miscellaneous spatial light modulator (SLM) technologies, e.g., magneto-optic, multiple quantum well, acoustic-optic Bragg cells, deformable mirrors, digital micromirror devices (DMD) and liquid crystal (LC) were developed. Nowadays, the most versatile devices are based on liquid crystal cells and micromirror displays.

As their name suggests, the main purpose of spatial light modulators is in their ability to modulate the incoming light wave by transmittance through liquid crystals or reflection on the array of micromirrors. These devices control the light in two dimensions consisting of addressable and light modulation parts. The optical attributes of the modulation part are modified by the information entered into the address part and then imprinted on the incident light. The spatial distribution of light such as the amplitude, phase, polarization, and propagation direction can be modified based on the properly addressed information.

3.3.1 Liquid crystal cells

Liquid crystals are considered as a phase of the matter with properties falling between the crystalline solid and the liquid state. As a result, they embody dielectric and optical anisotropy, i.e., the polarization dependence of the refractive index for most propagation directions and show typical flow behavior with no stable position or permanent spatial orientation of single molecules. These molecules can be characterized as uniaxial ellipsoids

with one long axis. The light propagation along directions that are not parallel to this optical axis is induced by two indices of refraction n_o and n_{eo} valid for two orthogonal polarization states referred to ordinary and extraordinary. This effect is known as birefringence [139].

For usage in liquid crystal displays (LCD) or SLMs, the LC are arranged in spatially separated cells (pixels). The optical properties of these elements can be manipulated by the application of an external electric field which changes the orientation of the molecules and causes the above-mentioned voltage-dependent birefringence. Regularly, this electric field is adjusted between covering glass plates around the LC material using transparent conductive layers coated on the inside of the plates. Thus, the LC pixels precisely change the polarization state or phase retardation of the light field by providing a well-defined voltage. Additionally, the electro-mechanical grid encompasses the LC cells and ensures the space for wires needed to addressing each cell with an independent voltage. Because of this overall two-dimensional array, the design acts as a two-dimensional grating and produces the corresponding diffraction pattern [140].

There exist several phases of liquid crystals differentiated by various molecule arrangement. The most commonly applicable types are nematic and smectic liquid crystals. For nematic liquid crystals, the molecules exhibit a characteristic linear alignment with a random distribution throughout the entire material volume. Smectic liquid crystals additionally form parallel layers with the same axes orientation.

Furthermore, it is possible to enforce the alignment of nematic molecules at the cells boundaries. This can be achieved by soft polishing of adjustment layers on a transparent cover material with scratches in the desired alignment direction. The small strokes associated with the polishing process form a preferred angle for the molecules, that are in contact with the cover plates, with their main axis parallel to the scratches. If the layers on both sides are polished in the orthogonal directions, the molecules in LC cells have tendency to maintain in their collective orientation. As a result, the molecules form a helix structure, which means that the molecules gradually rotate alongside the optical path to match the boundary conditions. This design is known as twisted nematic liquid crystals (TN-LC). In the presence of a sufficiently large applied voltage, the molecules that are not in close proximity to the boundary layers freely rotate and align their marginal axes with the applied field, i.e., pointing in a perpendicular direction to the cover glass plates [141].

Another universal design is called liquid crystal on silicon (LCOS), which basically means a structure, where a liquid crystal layer is attached to an electrically addressing silicon substrate formed by CMOS technology. The liquid crystals are concurrently aligned by the analogous alignment technology provided on the silicon and cover glass substrates, without being twisted as in the TN-LC design.

The aforementioned liquid crystals designs are used to construct specialized amplitude-only or phase-only spatial light modulators. This specific notation denotes that these types affect primarily the amplitude or phase part of impinging light or with much more efficiency than the second one.

3.3.2 Amplitude-only spatial light modulators

In the case of transmissive amplitude-only modulators, the TN-LC design is used with attached cross-oriented polarizers on both sides of the display. The orientation of these polarizers should be parallel to the boundary molecules to maintain the maximal display transparency. The generated helix structure of twisted nematic crystals then guarantees the change of the polarization state of the incident light. When the polarization of the incident light matches the entrance orientation of molecules, the polarization follows the twist of the molecules. Accordingly, the outgoing light leaves the LCs with a polarization that is perpendicular to the entrance one. In this setting, the light will pass through the exit analyzer without any change when no voltage is applied and is fully blocked with maximal adjusted voltage. The partial amplitude transmission is then limited by the dynamic range of analog/digital converter specific for the used SLM device. The schematic representation of such amplitude-only SLM is depicted in Figure 3.4 [142].

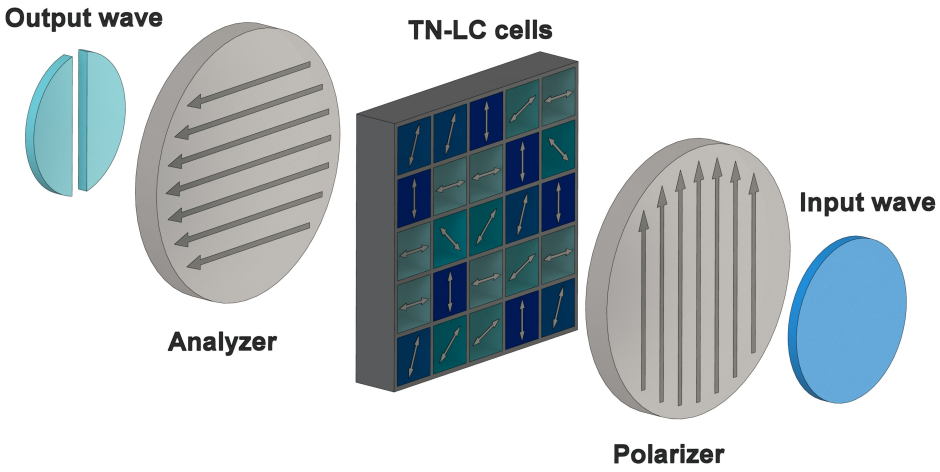

Figure 3.4: Scheme of application of amplitude-only SLM using twisted nematic liquid crystals. The SLM chip is overlaid by the crossed polarizers. By application of diverse electrical voltage, the rotation of internal molecules produces the change of incident polarization state which implicates the amplitude modulation.

Unfortunately, nowadays these types of SLMs are almost impossible to buy. One of the potential device model LC2012 [143] is produced by the Holoeye Photonics company. This modulator is more likely for educational purposes and familiarization with SLM technology.

A representative example can be the CRL OPTO XGA3 from CRL Opto company (now known as Forth Dimension Displays), which was used in the experiment in Chapter 4. This transmissive amplitude-only modulator using an active TFT screen with twisted nematic liquid crystals with the attached analyzer at the output plane. The screen consists of 1024×768 pixels with pixel size of 18×18 μm, fill factor around 40% and addressing depth of 8-bits, i.e., adjustable 256 gray levels.

Thanks to the low fill factor and used manufacturing process, the overall transmission is around 14% (for 600 nm) of the total incident light. This value is even more reduced when the display diffraction effects are taken into account. The diffraction pattern of a non-addressed modulator consists of N copies of zero diffraction order separated by a distance equal to the combination of parameters of a display. If we simply addressed the modulator by some function, i.e., send computer-generated hologram (CGH) as an image, the modulator transfer the result directly into the 0^{th} diffraction order, which may be undesirable. The solution can be in the mixing of extra lens phase or plane wave with the demanded function in the hologram generation process. The additional lens phase provides the defocus of the 0^{th} order intensity and plane wave creates new 1^{st} *working* diffraction order, which spatially shifts the resulting distribution out of the 0^{th} order. Nevertheless, these manipulations lower the total transmission efficiency of the modulator down to 2.5% of total incident light and make this modulator to be less practical in state-of-the-art application.

3.3.3 Phase-only spatial light modulators

The reflective phase-only spatial light modulators are mostly based on the LCOS technology with a reflective coating on the silicon substrate. This reflective mirror, with the concurrently oriented molecules on cell boundaries, allows to operate these modulators in a double-path regime and provides phase modulation of incoming light. The phase modulation is achieved by the application of the electric field on the LC molecules, where the differently rotated molecules induce the different refractive indices without changing the input polarization state. This associates different optical path lengths in liquid crystal cells and causes the desired phase retardation. However, another important aspects need to be considered to guarantee the phase-only modulation. At this point, it is necessary to provide a linear polarization state of incident light and its proper aligning with the entrance molecule's long axes. If both of these conditions are not met, the light polarization state changes and leads to the undesired cross modulation between the phase and amplitude of incident light. For illustration, the scheme of the LCOS chip structure is depicted in Figure 3.5.

Nowadays, this category of spatial light modulators is one of the most widespread.

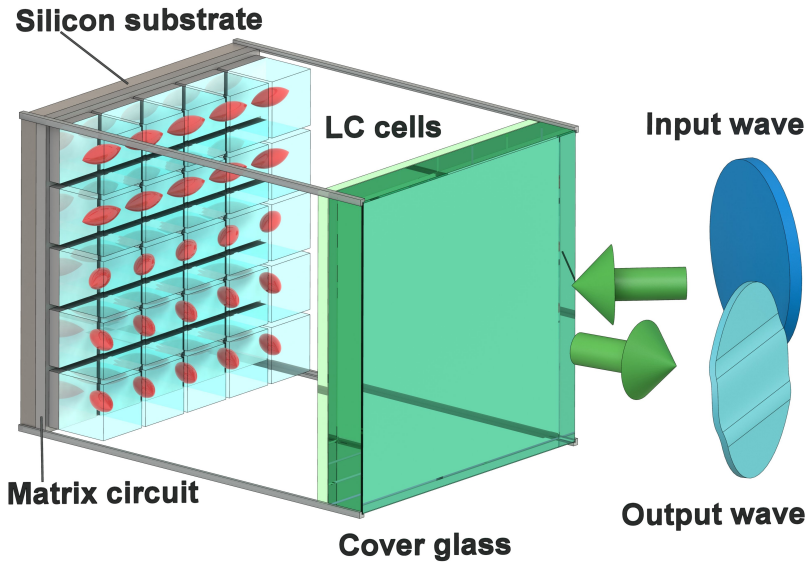

Figure 3.5: Illustration of phase-only SLM chip structure. The ground silicon substrate and matrix circuit are manufactured by CMOS technology with top-dashed reflective coating and electrically interconnected liquid crystals cells. The cell molecules, with parallel boundaries orientation rotate around their long axes inducing the phase retardation of linearly polarized incoming light.

There exist several companies developing and manufacturing a wide range of SLM models for different spectral regions and applications. Main differences are in cell thickness, phase stability, display size, reflection coatings, pixel size as well as used LC material. Typical examples are Meadowlark [144], Pluto-2 from Holoeye Photonics [145], and X13138 form Hamamatsu Photonics [146]. For the experiment in Chapter 5. we used the model X10468-01 from Hamamatsu Photonics. This phase-only modulator with the LCOS screen with parallel-aligned liquid crystals and a dielectric mirror installed on the rear side of the LC layer. Such a dielectric mirror increases the light-utilization efficiency up to 90%. The screen consists of 800×600 pixels with pixel size of 20×20 µm, 98% fill factor and 8-bits input signal levels.

Out of the box, the phase or amplitude modulation is influenced by highly nonlinear response of the liquid crystals depending on the applied voltage level. To reach the linear phase response, it is essential to implement the correction look-up-table, which mediates the voltage conversion between addressed digital signals and SLM control transducer. Besides, the maximal phase modulation is wavelength-dependent. Our model X10468-01 has the default look-up-tables for 2π at 633 nm and 2.8π modulation at 532 nm.

Despite the pixel structure of the LCOS display and its characteristic high order diffraction phenomena, this type exhibits excellent diffraction efficiency close to the theoretical limits. The diffraction efficiency is defined as the ratio between the 1^{st} and the 0^{th} diffraction

order intensities when no modulation is performed. This high efficiency can be managed by mixing multilevel blaze grating with the desired phase mask during computer hologram generation. Moreover, this phase grating serves like the plane wave in the amplitude modulator and associated grating period brings the overall diffraction efficiency up to 90%.

Most microdisplay components are not enough optically flat and introduce certain aberration terms to the incident wavefront. The most affected are the LC cells and covering glass plates. Typically, the contributed deformation is mainly spherical and in general not more than 2λ for central wavelength. Moreover, this error can be for the class of application minor problem with no effect on the result modulation. On the other hand, this supplementary phase can be effectively compensated thanks to the phase compensation mask. This compensation phase function can be superimposed in the same manner as the above-mentioned plane wave or blaze grating to all addressed functions.

One of the straightforward method how to mathematically generate this compensation mask is the Gerchberg-Saxton algorithm [147]. This iterative algorithm is based on retrieving the phase distribution between a couple of light transversal planes related by optical propagation function expressed by Fourier transform with the essential prior knowledge of both plane intensities. Of course, there exist many algorithm modifications. For our modulators, we chose one of the fastest and easy-to-use method based on the application of a single optical vortex [148]. With this type of compensation mask, one is able to flatten the modulated wavefront up to $\lambda/10$ in the central display region.

3.3.4 Digital micromirror displays

The digital light projection (DLP) display is an innovative technology originally developed by Texas Instruments in 1987. This electro-optical solution, known as the digital micromirror device, is based on the micro-electro-mechanical systems (MEMS) that can be used for high speed and efficient modulation of the amplitude of light. These microchips are arrays of independently controlled highly reflective aluminum micromirrors built on top of associated CMOS memory cells, which can be sequentially synchronized with chromatic illumination unit to create compact projector modules. Nowdays, the DLP technology finds a place in a wide variety of advanced light control applications, from micro projection modules embedded in smartphones to high powered projectors as well as 3D printers and augmented reality displays [149, 150].

Besides, the DMD and illumination engine, the overall system is managed by the DMD controller chip, which is the hearth of each module. During the active operation, the DMD controller adjusts each micromirror memory cell between two operational states "ON" or

"OFF". These two conditions are controlled by clocking pulse, which causes each micromirror to be electrostatically deflected about a central hinge to the associated tilted states. These angles depend on the used pixel architecture, where the standard VSP pixel architecture has $\pm 12°$ tilt with diamond pixel orientation or newer TRP pixel architecture $\pm 17°$ tilt with orthogonal pixel orientation. A comparison between these two architectures is depicted in Figure 3.6. This newer architecture adopting a higher resolution by smaller pixel pitch down to 5.4 µm and enhances modulation processing features by an increased tilt angle. In a common projection system, the "$+$" landed state corresponds to an “ON” pixel, and the "$-$" state corresponds to an “OFF” pixel. In advanced applications, the "$\pm$" states offer two general output ports with the desired pattern and its inverse, which is normally blocked in the projector modules by aperture stop [151].

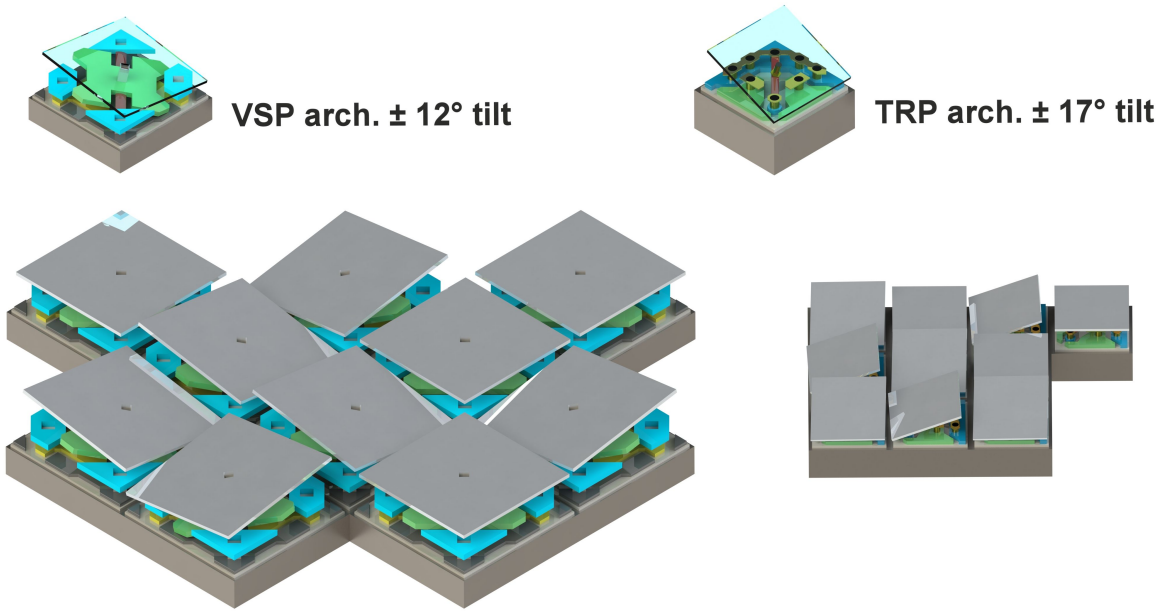

Figure 3.6: Comparison between VSP and TRP DMD pixel architectures and their typical array ordering. The VSP architecture (left) is organized into a diamond ($45°$ rotated square micromirrors) orientation. The initial state (parked position) is $0°$ and "ON"/"OFF" states are electrostatically tilted $\pm 12°$ around the central hinge. The newer TRP architecture (right) is organized into an orthogonal pixel array. The initial state is again flat and for "ON"/"OFF" states the mirrors are firstly electrostatically tilted about $17°$ in one diagonal and then additionally tilted to the difference of $90°$.

The addressing part of the DMD chips works through computer-generated patterns, similarly as for the spatial light modulators. These patterns are normally uploaded as images into internal memory or streaming thought video interface. For a grayscale (binary) projection, the controller synchronized the ON/OFF cycles (set permanent $\pm$ positions) of each mirror mostly in 8, 12, or 16-bits (1-bit) depths. Accordingly, the RGB color images are

produced by additional synchronization with multiple light sources, typically LED modules.

The Texas Instruments affords an extensive selection of fully configured standalone solutions called DLP LightCrafter evaluation modules (DLP EVM) or independent DMD chips. These EVM modules and DMD chips differ mainly in pixel and DMD size, illumination and projecting systems, and applied DMD controllers with associated switching rate speed and addressable bit depth. For experiments performed in Chapters 4, 5, and 8 the DLP3000 LightCrafter evaluation module was used. This evaluation module includes 0.3-inch micromirror VSP diagonal array of 608×684 aluminum mirrors with effective pixel pitch of 10.8 μm (diagonally 7.6 μm) and fill factor of 92%. The main advantage is in the used DLPC300 digital controller, which allows one-to-one mapping of input image data to micromirror array for 1-bit (8-bits) patterns with switching rates up to 4000 Hz (120 Hz).

For implementation in laboratory and illumination by different light sources, it is necessary to make the DMD chip fully accessible by dismounting the illumination engine and projection objective. Nevertheless, this modification also removes the aperture stop blocking the inverse output pattern and contributes together with the coherent illumination to overall diffraction effects. When a DMD is illuminated with a coherent source, the chip itself acts as a reflective diffraction grating with the tilted grooves and reflected light results into a 2D pattern of diffraction orders. The orders locations are then determined by the light incident angle, micromirrors pitch, wavelength as well as micromirrors tilt angle. Generally, if the incident illumination angle is fixed, variations in additional tilt do not cause the movement of diffraction orders but cause the energy distribution shifts between them. Consequently, there exist two limiting conditions called *blaze* and *anti-blaze*. A blaze condition occurs when the incident angle and the micromirror tilt are arranged so that center of diffraction envelope lines up with the specific diffraction order. When this arises, a majority of the energy is directed into this blazed order. On the other hand, for the anti-blaze condition, the envelope center falls between diffraction orders and leads to an equal energy distribution between multiple orders. Considering the character of our experiments and the fact that the blaze condition of the used model required higher incident angles, which induces the deformation of reflected patterns, we always worked in the anti-blaze condition.

Chapter 4

Achieving the ultimate optical resolution

This chapter is based on following publication:

[1] M. Paúr, B. Stoklasa, Z. Hradil, L. L. Sánchez-Soto and J. Řeháček. '*Achieving the ultimate optical resolution*'. In: *Optica* **3.10** (2016), pp. 1144–1147.

In this chapter, we experimentally examine a new method for resolving two close incoherent optical point sources. The minimum separation between two sources, that may be resolved into distinct objects, has been generally specified by the well-known Rayleigh's criterion for over a century [14, 152]. Quite recently, a groundbreaking proposal [6] has revisited this problem from the viewpoint of quantum optics, quantum metrology and statistical image processing with the comprehension of estimation theory [6, 41, 43].

The main idea is based on the computation of the quantum Fisher information, which determines how well the separation between two incoherent points can be estimated optimized over all possible measurements. When only the conventional intensity scan in the image plane is taken, the associated Cramér-Rao lower bound diverges as the separation between sources tends to zero, an effect that has been dubbed as *Rayleigh's course*. Surprisingly enough, the quantum Cramér-Rao lower bound maintains a constant value for any separation of the sources.

Here, we present the optimal strategies that can lift this curse and introduce one of the suitable measurements for Gaussian and slit apertures accomplished by digital holographic technique. Our results confirm immunity to the Rayleigh's curse and estimation of two point separation from the far field almost as precisely as conventional methods do for locating isolated sources.

4.1 Theoretical background

Let us first set the stage for our simplified model. We follow Lord Rayleigh's lead [14] and assume quasimonochromatic paraxial waves with one specified polarization and one spatial dimension x, denoting the image-plane coordinate. Moreover, we consider a spatially invariant unit-magnification imaging system characterized by its PSF, which represents its normalized intensity response to a point light source, i.e., $I(x) = |\langle x|\Psi\rangle|^2 = |\Psi(x)|^2$.

Then we presume, that two incoherent point sources are imaged by this optical system. For simplicity, we consider them to have equal intensities and to be located at two unknown positions $X_1 = \mathfrak{s}/2$ and $X_2 = -\mathfrak{s}/2$ in the image plane. The objective is to give the best estimate of the separation $\mathfrak{s} = X_1 - X_2$. The relevant coherence matrix, which embodies the image-plane modes, can be noted down as

$$\varrho_{\mathfrak{s}} = \frac{1}{2}(|\Psi_1\rangle\langle\Psi_1| + |\Psi_2\rangle\langle\Psi_2|), \tag{4.1}$$

where $|\Psi_{1,2}\rangle = \exp\left(\pm i\hat{\mathbf{P}}\mathfrak{s}/2\right)|\Psi\rangle$ and $\hat{\mathbf{P}}$ is the momentum operator, that generates displacement in the x variable. In the x-representation, the coherence matrix appears as normalized probability distribution of detected photons in the image plane, namely $\varrho_{\mathfrak{s}}(x) = \frac{1}{2}(|\Psi(x+\mathfrak{s}/2)|^2 + |\Psi(x-\mathfrak{s}/2)|^2)$. The scheme of the coherence matrix for the Gaussian point sources is displayed in Figure 4.1

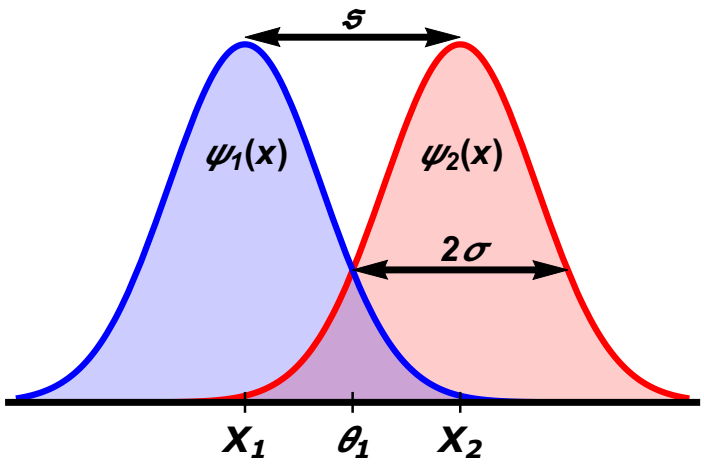

Figure 4.1: Two Gaussian wave functions in the image plane, each expanding from a point source, on positions X_1 and X_2. θ_1 is their centroid, $\mathfrak{s}$ is the separation between PSFs and σ is its width.

For points close enough together, ($\mathfrak{s} \ll 1$), which is the most interesting case, a linear expansion gives

$$|\Psi_{1,2}\rangle = \mathcal{N}(1 \pm i\hat{\mathbf{P}}\mathfrak{s}/2)\,|\Psi\rangle\,, \tag{4.2}$$

where $\mathcal{N} = (1 + \langle\Psi|\,\hat{\mathbf{P}}^2\,|\Psi\rangle\,\mathfrak{s}^2/4)^{-1/2}$ is a normalization constant. The hearth of all difficulties of this problem is, that these two states are not orthogonal, i.e., $\langle\Psi_1|\Psi_2\rangle \neq 0$, which physically means that these two modes cannot be separated by independent measurements.

To circumvent this problem, we come up with the definition of symmetric (+) and antisymmetric (-) states

$$\begin{aligned} |\Psi_+\rangle &= \mathcal{C}_+(|\Psi_1\rangle + |\Psi_2\rangle) \simeq |\Psi\rangle\,, \\ |\Psi_-\rangle &= \mathcal{C}_-(|\Psi_1\rangle - |\Psi_2\rangle) \simeq \frac{\hat{\mathbf{P}}\,|\Psi\rangle}{\sqrt{\langle\Psi|\,\hat{\mathbf{P}}^2\,|\Psi\rangle}}, \end{aligned} \tag{4.3}$$

where $\mathcal{C}_+$ and $\mathcal{C}_-$ are normalization constants. When $\langle\Psi|\,\hat{\mathbf{P}}\,|\Psi\rangle = 0$ these modes are orthogonal which typically happens when the PSF is inversion symmetric.

Direct imaging, denoted as the classical measurement method, is one particular measurement method permitted by quantum mechanics. Following Eq. (3.19), the relevant Fisher information for this standard image-plane intensity detection (or photon counting, in the quantum regime) reads as

$$\mathcal{F}_{std}(\mathfrak{s}) = N \int_{-\infty}^{\infty} \frac{1}{\varrho_{\mathfrak{s}}(x)} \left[\frac{\partial \varrho_{\mathfrak{s}}(x)}{\partial \mathfrak{s}}\right]^2 dx, \tag{4.4}$$

where N denotes the total amount of detected photons in the image plane [76, 135], which can be approximately taken as Poissonian with a mean $N\varrho_{\mathfrak{s}}(x)$. Here, the Fisher information is a mathematical measure of the sensitivity of an observable quantity (PSF) to changes in its underlying parameters (emitters) position. It is important to point, that the number of detected photons N is necessary for further computation because it scales the resulting CRLB (qCRLB) quantity. Performing again a first-order expansion in $\mathfrak{s}$, $\mathcal{F}_{std}$ can be expressed in terms of the $I(x)$:

$$\mathcal{F}_{std}(\mathfrak{s}) \simeq N\mathfrak{s}^2 \int_{-\infty}^{\infty} \frac{[I''(x)]^2}{I(x)} dx. \tag{4.5}$$

Consequently, the Fisher information goes to zero quadratically as $\mathfrak{s} \to 0$ and CRLB goes to infinity, respectively, which clearly shows a progressively worse estimation of the separation for closer sources. This divergent behavior has been termed the *Rayleigh's curse* [6]. In the other words, there is much more information available about the separation of the sources in the phase of the field than in the intensity alone.

With the above formalism, the quantum estimation theory can be directly applied to this classical problem. The pivotal quantity is the quantum Fisher information [33, 153]. It

is defined as $\mathcal{F} = \mathrm{Tr}\left[\varrho_{\mathfrak{s}} L_{\mathfrak{s}}^2\right]$, where the symmetric logarithmic derivative $L_{\mathfrak{s}}$ is a self-adjoint operator [76]. A direct calculation for one photon finds that

$$\mathcal{F} = 2\left[\frac{1}{p_-}\left\langle\Psi_-\right|\left(\frac{\partial\varrho_{\mathfrak{s}}}{\partial\mathfrak{s}}\right)^2\left|\Psi_-\right\rangle + \frac{1}{p_+}\left\langle\Psi_+\right|\left(\frac{\partial\varrho_{\mathfrak{s}}}{\partial\mathfrak{s}}\right)^2\left|\Psi_+\right\rangle\right] \simeq \left\langle\Psi\right|\hat{\mathbf{P}}^2\left|\Psi\right\rangle, \tag{4.6}$$

where p_+ and p_- are eigenvalues of coherence matrix constituted by modes in Eq. 4.3. Interestingly, the quantum Fisher information turns out to be independent of $\mathfrak{s}$ and the associated qCRLB, defined by Eq. (3.25), remains constant too. Moreover, considerable improvement can be obtained if an optimal measurement, saturating the Eq. (4.6), is implemented. The example of the Fisher information quantity for two Gaussian point sources is depicted in Figure 4.2.

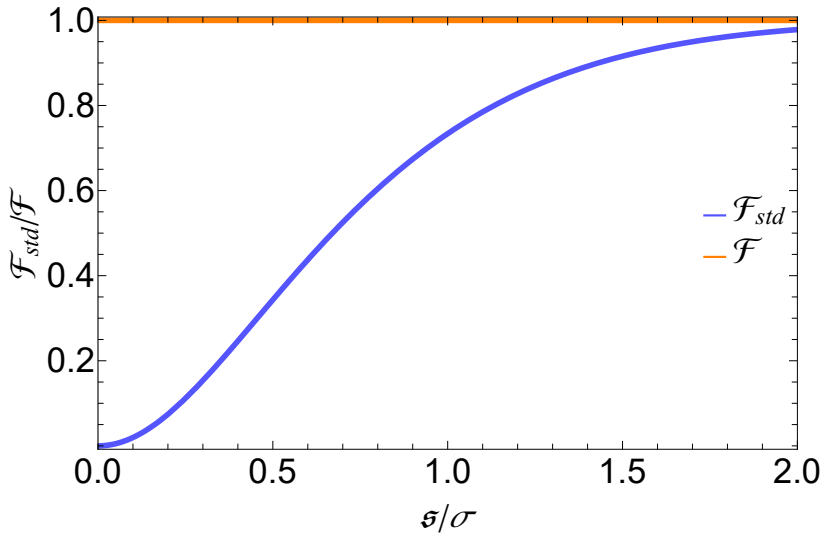

Figure 4.2: Example of normalized Fisher information for two Gaussian incoherent point sources with $\sigma = 0.5$ mm. For standard intensity detection (blue line), the quadratic decay when $\mathfrak{s} \to 0$ is apparent. Contrariwise, the quantum Fisher information (orange line) embodies the constant behavior, i.e., independence on separation $\mathfrak{s}$.

4.2 Optimal Strategies

From our previous discussion, it is clear that the projectors $\prod_j = |\Psi_j\rangle\langle\Psi_j|$ $(j = +, -)$ comprise the optimal measurements of the parameter $\mathfrak{s} \ll 1$ [44]. From Eq. (4.6), it can be seen that the antisymmetric mode p_- gives the leading contribution, and thus, most useful information can be extracted from the $\prod_-$ channel. As a consequence, the wave function

of the optimal measurement becomes

$$\Psi_{opt}(x) = \langle x|\Psi_-\rangle = \frac{\Psi'(x)}{\sqrt{\mathcal{F}}}, \tag{4.7}$$

where

$$\mathcal{F} = \langle\Psi|\,\hat{\mathbf{P}}^2\,|\Psi\rangle = \int_{-\infty}^{\infty} [\Psi'(x)]^2\,dx. \tag{4.8}$$

Let us consider two relevant examples of PSFs, the Gaussian and the sinc,

$$\begin{aligned} \Psi^G(x) &= \frac{1}{(2\pi\sigma^2)^{\frac{1}{4}}} \exp\left(-\frac{x^2}{4\sigma^2}\right), \\ \Psi^S(x) &= \frac{1}{\sqrt{w}} \frac{\sin \pi x/w}{\pi x/w}, \end{aligned} \tag{4.9}$$

where σ and w are effective widths that depend on the wavelength. From the Eq. (4.8) it is easy to obtain the quantum Fisher information for these two cases: $1/(4\sigma^2)$ and $\pi/(3w^2)$. The optimal measurements are then

$$\begin{aligned} \Psi^G_{opt}(x) &= \frac{-1}{(2\pi)^{\frac{1}{4}}\sigma^{\frac{3}{2}}} x \exp\left(-\frac{x^2}{4\sigma^2}\right), \\ \Psi^S_{opt}(x) &= \sqrt{3}\left[\frac{w^{\frac{1}{2}}}{\pi x}\cos\left(\frac{\pi x}{w}\right) - \frac{w^{\frac{3}{2}}}{\pi^2 x^2}\sin\left(\frac{\pi x}{w}\right)\right]. \end{aligned} \tag{4.10}$$

4.3 Experimental realization

To project two incoherent points on optimal functions from Eq. (4.10), one needs to separate the image-plane field in terms of the desired spatial modes. This has been provided in the laboratory with the setup sketched in Figure 4.3. The incoherent point-like sources were generated by a digital light projector (DLP) Lightcrafter evaluation module (Texas Instruments), which uses a digital micromirror chip (DMD) with square micromirrors of 7.6 µm size each. This allows for precise control of the points separation by individually addressed two particular micromirrors regions. The DMD chip was illuminated by intensity-stabilized He-Ne laser with installed beam expander to provide a sufficiently uniform beam. The spatial incoherence was ensured by switching between the two object points, so that only one was "ON" at a time, keeping the switching time well below the detector time exposition.

The two point sources were imaged by a low numerical-aperture lens and shaped by an aperture placed behind the lens. A circular diaphragm produced Airy rings, but these are well approximated by a Gaussian PSF. The sinc PSF was obtained by inserting a square slit.

We experimentally measured the values $\sigma = 0.05$ mm and $w = 0.15$ mm. The Rayleigh criteria for these values are 2.635σ and w, respectively. The two-point separations $\mathfrak{s}$ were varied in steps of 0.01 mm, which corresponds to steps 0.2σ for the Gaussian and $0.067w$ for the sinc PSF.

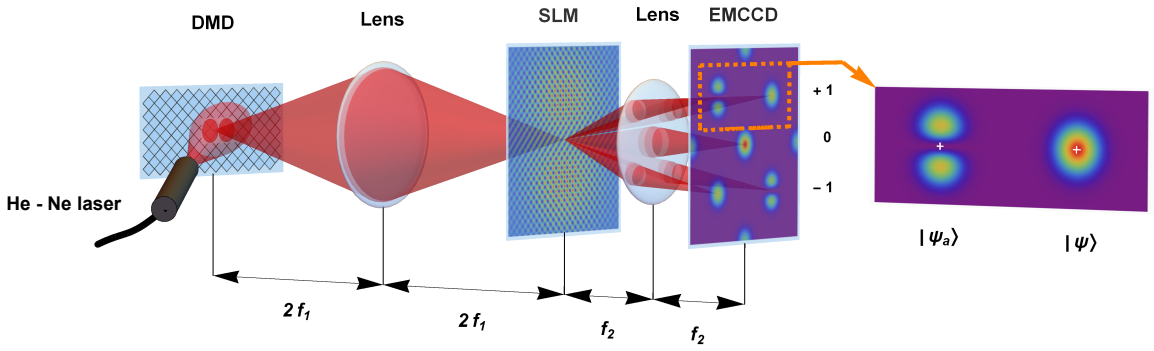

Figure 4.3: Schematic diagram of the experimental setup. Two incoherent point sources are created with a high frequency switch mode of DMD illuminated with an intensity-stabilized He-Ne laser. The sources are imaged by a low-aperture lens. In the image plane, projection onto different modes is performed with a digital hologram created with an amplitude spatial light modulator (SLM). Information about the desired projection is carried by the first-order diffraction spectrum, which is mapped by a lens onto an EMCCD camera.

The projection onto any basis was performed with an amplitude-only spatial light modulator (CRL OPTO). We prepared a hologram at the image plane of the lens as a product of the interference between a tilted reference plane wave and the desired projection function Ψ_{opt}. When this was illuminated by two point sources, the intensity in the propagation direction of the reference wave was

$$\left|\int_{-\infty}^{\infty}\Psi^{*}_{opt}(x)\Psi(x+\mathfrak{s}/2)dx\right|^{2}+\left|\int_{-\infty}^{\infty}\Psi^{*}_{opt}(x)\Psi(x-\mathfrak{s}/2)dx\right|^{2}. \tag{4.11}$$

Different projections can be obtained with different reference waves. For the Gaussian PSF, we prepared projection on both the zero- and first-order Hermite-Gaussian (HG) modes, which matches Ψ^{G} and Ψ^{G}_{opt}. Interestingly, for small separations, the mode HG_{10} attaining more than 90% of quantum Fisher information quantity itself. This means, that the additional HG modes projections are not needed and the whole measurement is considerably simplified. For clarity, the normalized Fisher information for the first five HG modes is illustrated in Figure 4.4. For the sinc PSF, the points were also projected on the PSF itself and its first derivative. Moreover, the measurement of the zero-order mode is used to assess the total number of photons in each measurement run.

The desired projection is carried by the first diffraction order. To get the information,

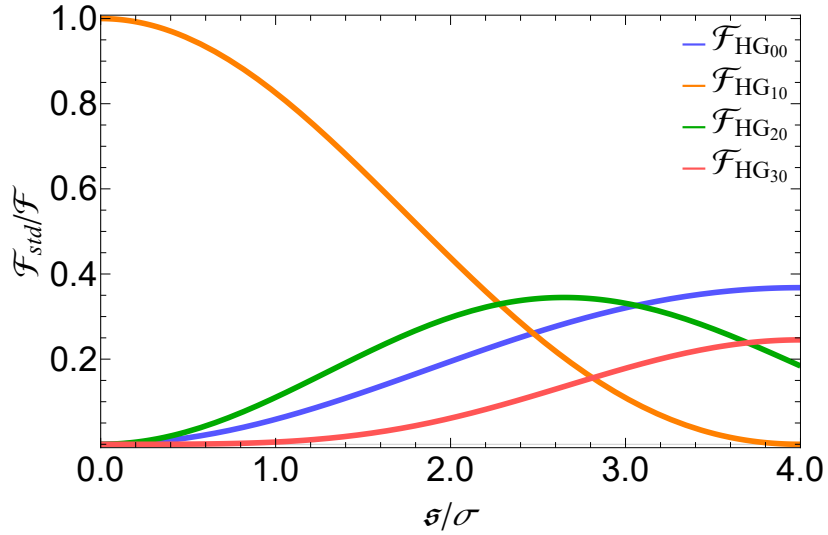

Figure 4.4: Comparison of normalized Fisher information quantities for projections into the first five Hermite-Gaussian modes. For small separations, the HG_{01} mode attains the quantum Fisher information bound which is sufficient for estimation of separation parameter $\mathfrak{s}$. However, for larger separations, the information overflows into higher modes which evoke the necessity of their detection.

the signal is Fourier transformed by a short focal lens and detected by a cooled electron-multiplying CCD camera (EMCCD) (Raptor Photonics) working in the linear mode with on-chip gain g to suppress the effects of read-out noise and dark noise. As depicted in Figure 4.3, the outcome of measurement consists of two photon counts detected from the Fourier spectrum points representing spatial frequencies connected with the reference waves. These data carry information about the separation of the two incoherent point sources.

The noise from a final number of detection events is further increased by the excess noise due to the random nature of the EMCCD gain, the background noise caused by the scattered photons reaching the detector, and by a slight misalignment of the SLM hologram with respect to the two-point image. While the excess camera noise tends to increase the measurement errors uniformly across the measured range of separations, the constant background noise affects mostly the smallest separations.

4.4 Results and discussion

The numbers of photons n_0 and n_- detected in the PSF $|\Psi\rangle$ and antisymmetric (optimal) modes $|\Psi_-\rangle$, respectively, was determined by using the EMCCD pixel capacity and camera gain g. The relative frequency of measuring the antisymmetric projection was calculated as $f_- = n_-/(n_0+n_-)$, the denominator n_0+n_- reports the total number of detected photons. The estimator of the separation is then obtained by solving the relation $f_- = \langle\Psi_-|\,\varrho_{\mathfrak{s}}\,|\Psi_-\rangle$

for $\mathfrak{s}$. Moreover, we didn't make any assumption about the smallness of $\mathfrak{s}$, which helps to produce unbiased estimates of larger separations.

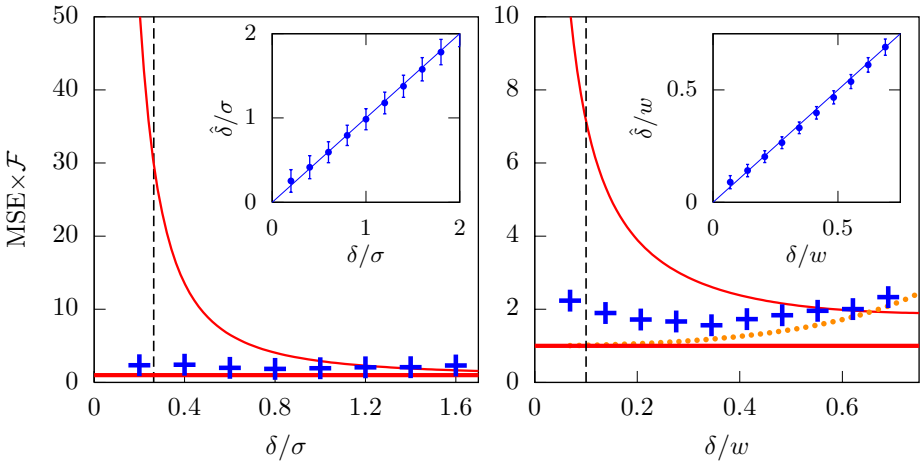

Figure 4.5: The mean-square error of estimated separation for Gaussian (left) and sinc (right) PSFs. Separations are expressed in units of PSF widths σ and w and the MSE in units of the qCRLB. The main graph compares the performance of our experimental method (blue symbols) with the theoretical lower bound for the CCD measurement (thin red curve) and the ultimate quantum limit (thick red line). The vertical dotted lines delimit the 10% of the Rayleigh limit for each PSF. The insets show the statistics of the experimental estimates with its error bars.

To determine estimator characteristics, 500 measurements for each separation were carried out. The results are summarized in Figure 4.5. The optimal method overcomes the direct position measurement for small and moderate separations. For the Gaussian PSF (left panel) and the smallest separation 0.2σ, the experimental mean square estimator (MSE) is 2.35x qCRLB i.e. more than 20 times smaller than the error of the standard intensity measurement (51.2x qCRLB). For the sinc, the experimental MSE is 2.23x qCRLB for the smallest separation, which is 4.5 times lower than the error of the position measurement (10.1x qCRLB).

Two different effects increase the error slightly above the theoretical limit. For small and moderate separations, the background and excess noise discussed above become important. For large separations, this type of two-mode measurement is no longer optimal. However in this regime, the direct intensity detection becomes nearly optimal, so any setup attaining the theoretical limit would bring only minimal improvement.

In conclusion, we have developed and demonstrated a simple technique that surpasses traditional imaging techniques in its ability to resolve two closely separated point sources. The method does not require any "exotic" illumination and is applicable to classical incoher-

ent sources. Our results verify that the diffraction resolution limits are not a fundamental constraint but, instead, the consequence of traditional imaging techniques discarding the phase information.

Chapter 5

Tempering Rayleigh's curse with PSF shaping

This chapter is based on following publication:

[2] M. Paúr, B. Stoklasa, J. Grover, A. Krzic, L. L. Sánchez-Soto, Z. Hradil and J. Řeháček. '*Tempering Rayleigh's curse with PSF shaping*'. In: *Optica* **5.10** (2018), pp. 1177–1180.

In this chapter, we further develop the methods and results from the previous chapter. Again, we are focusing on the resolution of two close incoherent point sources using spatially invariant imaging systems. We revisit the scenario of direct detection, for it is the cut-and-dried method used in the laboratory. As mentioned before, the information one can gain about the separation between two point sources decays quadratically to zero with decreasing separation, effect denominated as the *Rayleigh's curse*.

Contrary to this belief, we identify a class of PSFs with a linear decrease of Fisher information for small separations. Moreover, we show that any "well-behaved" symmetric PSF can be easily converted into such a form with a simple nonabsorbing signum filter.

Here, we experimentally demonstrate the application of a simple signum phase mask, i.e., *signum filter* with the conjunction of a direct detection scheme, which confirms the linear Fisher information drop-off. This scaling law opens new space for significant superresolution capabilities and reflects that the advantage of the previously mentioned quantum schemes with separation-independent Fisher information over classical techniques is smaller than previously thought.

5.1 Theoretical background

Firstly, we set our theoretical model, analogous to that of the previous Chapter. We work with a spatially invariant imaging system and two equally bright incoherent point sources separated by a distance $\mathfrak{s}$. We assume quasimonochromatic paraxial waves with one specified polarization and one spatial dimension, with x denoting the image-plane coordinate in the direction of separation. This simplified 1D geometry is sufficient to make the procedure clear and it works for some applications such as spectroscopy. The more realistic 2D case can be processed along the same lines, although at the price of dealing with a two-parameter estimation.

When we denote $I(x)$ as the spatial distribution of the image plane intensity generated by a point source, called the PSF [83], the resulting image can be written as

$$\varrho_{\mathfrak{s}}(x) = \frac{1}{2}\left[I(x+\mathfrak{s}/2) + I(x-\mathfrak{s}/2)\right], \tag{5.1}$$

where $\varrho_{\mathfrak{s}}(x)$ is the same probability density function for detecting light as in Chapter 4. We model light emission (detection) as a Poissonian random process (shot noise) [154]. The precision in estimating $\mathfrak{s}$ is again governed by the Fisher information aforementioned in Eq. (4.4). Without loss of generality, we set $N = 1$ and evaluated the precision per single detected photon. Consequently, the parameter N is then reintroduced in the final results. The CRLB ensures that the variance of any unbiased estimator $\hat{\mathfrak{s}}$ of the quantity $\mathfrak{s}$ is bounded by the reciprocal of the Fisher information viz. Eq. (3.14).

Since we are primarily interested in a case of small separations, we expand $\varrho_{\mathfrak{s}}(x)$ getting $\varrho_{\mathfrak{s}}(x) = I(x) + I''(x)/8\mathfrak{s}^2 + O(\mathfrak{s}^4)$, where a prime denotes derivative with respect to the variable $\mathfrak{s}$. It is useful to remark that the odd powers in the above expansion do not contribute, because these powers cancel each other from two PSF components. The associated Fisher information becomes

$$\mathcal{F}_{std}(\mathfrak{s}) = \int_{-\infty}^{\infty} \frac{\mathfrak{s}^2\left[I''(x)\right]^2}{16I(x)} + O(\mathfrak{s}^2)dx. \tag{5.2}$$

Commuting the order of integration and summation immediately yields a quadratic behavior for all PSFs: $\mathcal{F}(\mathfrak{s}) \propto \mathfrak{s}^2 + O(\mathfrak{s}^4)$. However, such an operation is not always admissible [155], which leaves room for tempering Rayleigh's curse with PSF shaping techniques.

5.2 PSF shaping using signum phase mask

To illustrate this point, let us assume, for the time being, that our PSF is well approximated by a parabolic profile near the origin, i.e., $I(x) \simeq ax^2$, which infers to

$$\varrho_{\mathfrak{s}}(x) \simeq a(x^2 + \frac{\mathfrak{s}^2}{4}), \qquad x, \mathfrak{s} \ll 1. \tag{5.3}$$

When this holds true, the integrand in Eq. (4.4) diminishes to a Lorentzian function:

$$\mathcal{F}_{std}(\mathfrak{s}) \simeq \int \frac{\alpha^2 \mathfrak{s}^2}{4x^2 + \mathfrak{s}^2} dx. \tag{5.4}$$

Because of the strong peak at $x = 0$ and when $\mathfrak{s} \ll 1$ the tails of the Lorentzian do not contribute eminently and can be neglected. As a result, we get

$$\mathcal{F}_{std} \simeq \lambda \mathfrak{s}, \tag{5.5}$$

with $\lambda = \pi\alpha/2$ and the information is indeed linear rather than quadratic at small separation.

Now, we want to show that any PSF can be converted to the form of Eq. (5.4) by applying a simple non-absorbing spatial filter at the output of the system. In what follows, $\Psi(x)$ indicates the amplitude of the PSF and $\Psi(f)$ its Fourier transform. We process the image by a coherent processor, such as a standard $4f$ system [83] schematized in Figure 5.1.

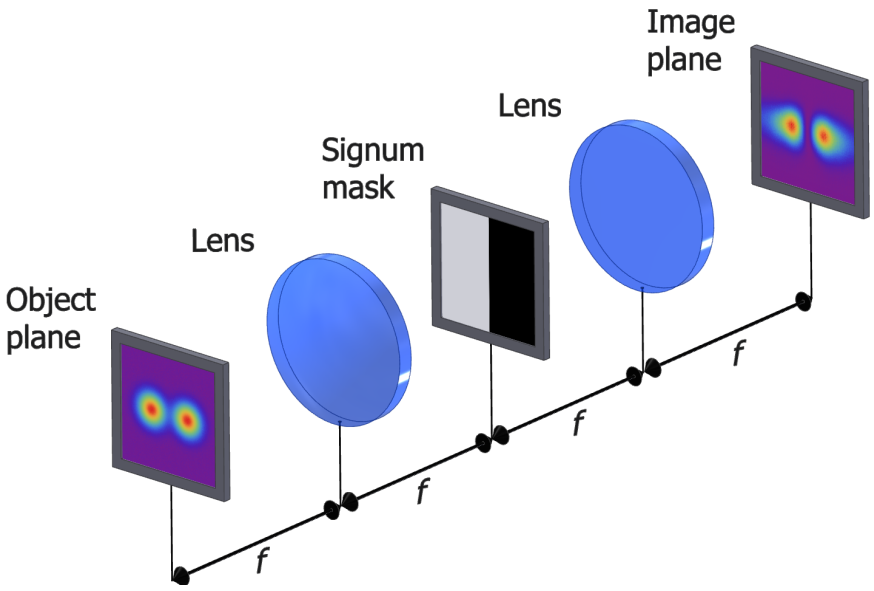

Figure 5.1: Scheme of an optical coherent $4f$ processor, with a signum phase mask in its Fourier plane.

In the Fourier plane, each incoherent point source gives rise to $\Psi(x \pm \mathfrak{s}/2) \mapsto \Psi(f)$ $\exp(\pm i\pi f s)$. In that plane we apply a signum mask: $\mathrm{sgn}(f)\psi(f)\exp(\pm i\pi f s)$, where the sgn function holds for a real number and $t \neq 0$ $\mathrm{sgn}(t) = |t|/t$ and $\mathrm{sgn}(0) = 0$ for $t = 0$. As the signum is a pure phase filter, no photons are absorbed. The signal components are then convolved with the inverse Fourier transform of the signum function, which is $\mathfrak{F}^{-1}\{\mathrm{sgn}(f)\} = -i/(\pi x)$. In this way, the processor performs

$$\Psi_{\pm}^{sgn}(x, \mathfrak{s}) = -\frac{i}{\pi} \int \frac{\Psi(x' \pm \mathfrak{s}/2)}{x - x'} dx', \tag{5.6}$$

which is the Hilbert transform of the signal. The optical implementation of this type of transformation has a long history [156–158]. It has been used in several fields, but most particularly in image processing of edge enhancement because it emphasizes the derivatives of the image.

Applying the change of variable $\xi = x' - x$, expanding Ψ to second order under the assumption of small separation and using the spatial symmetry of Ψ, we can approximate the detection probability density function near the origin by above-mentioned parabolic shape

$$\varrho_{\mathfrak{s}}^{sgn}(x, \mathfrak{s}) = \frac{1}{2}\left[|\Psi_{-}^{sgn}(x, \mathfrak{s})|^2 + |\Psi_{+}^{sgn}(x, \mathfrak{s})|^2\right] \simeq \alpha(x^2 + \mathfrak{s}^2/4), \tag{5.7}$$

with $\alpha = \left[\int \Psi'(\xi)/\xi d\xi\right]^2/\pi^2$. It is appropriate to mention that the parabolic behavior of Eq. (5.7) is general, but the value of the coefficient α depends on the explicit form of the PSF. Thus, we have a linear Fisher information such as in Eq. (5.5). In physical terms, this happens because the Fourier-space processing integrates the phase information. Besides, the combined system consisting of the imaging and PSF reshaping steps remains spatially invariant and so the information about separation is not degraded by misaligning of the signal and detection devices, as it happens, for example, when the centroid of the two-component signal is not perfectly controlled.

For completeness, we can verify our proposal with the relevant example of a system characterized by a Gaussian PSF: $\Psi(x) = (2\pi\sigma^2)^{-1/4}\exp\left(-\frac{1}{4}x^2/\sigma^2\right)$, where σ is an effective width of Gaussian function. Henceforth, we take this parameter as our basic unit length, so the corresponding magnitudes ($\mathfrak{s}$, $\Delta\mathfrak{s}^2$, etc.) appear dimensionless. Apart from its computational efficiency, the Gaussian PSF approximates fairly well the Airy distribution when illumination is done by a Gaussian distribution that apodizes the circular aperture.

Then the standard Fisher information associated with the classical direct imaging scheme can be obtained from (4.4) resulting in:

$$\mathcal{F}_{std}(\mathfrak{s}) \simeq \frac{(\mathfrak{s}/\sigma)^2}{8\sigma^2}, \tag{5.8}$$

which confirms once again the quadratic scaling of Rayleigh's curse. Now let's compare this result with information accessible by signum-filter-enhanced detection. We first perform the Hilbert transform of the Gaussian PSF:

$$|\Psi_{\pm}^{sgn}(x,\mathfrak{s})|^2 = \frac{2\sqrt{2}D(\frac{x\pm\mathfrak{s}/2}{2\sigma})^2}{\pi^{3/2}\sigma}, \tag{5.9}$$

where $D(z)$ denotes Dawson's integral [159]. Similar results have been reported for the dispersion relations of a Gaussian profile [160]. In particular, $D(-z) = -D(z)$ and $D(z) \simeq z(1 - \frac{2}{3}z^2)$ for $z \to 0$, so the dominant behavior is indeed linear. Therefore, the expansion in (5.7) holds with $\alpha = (2\pi^3)^{-1/2}\sigma^{-3}$ and as a consequence, the corresponding Fisher information is

$$\mathcal{F}_{sgn}(\mathfrak{s}) \simeq \frac{\mathfrak{s}}{2\sqrt{2\pi}\sigma^3}. \tag{5.10}$$

The detection probabilities and Fisher information densities typical for signum-enhanced detection with a Gaussian PSF are shown in Figure 5.2 for two different values of σ.

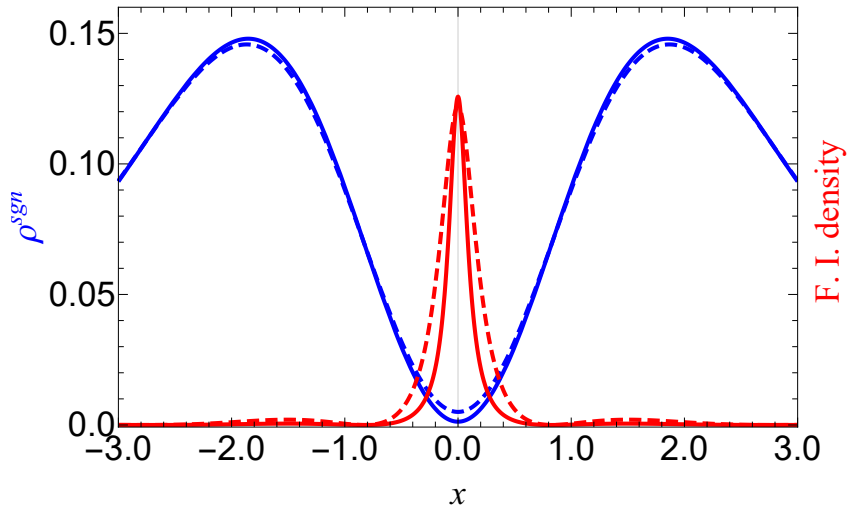

Figure 5.2: Detection probabilities (blue line) and Fisher information densities (red) corresponding to a Gaussian PSF modified by the signum filter for separations 0.2σ (solid lines) and 0.4σ (dashed lines).

Note that nonzero separation is evidenced by nonzero readings at the center of the image. Interestingly, most of the information about the separation comes from detections near the origin, and this region extenuates with decreasing $\mathfrak{s}$.

The superresolution potential of this technique is illustrated in Figure 5.3. The linear scaling can provide big advantages in terms of the resources required to measure very small separations. For example, to measure a $10\times$ smaller separation with a given precision, $100\times$ more detection events with the conventional setup are required, while just $10\times$ would do with the present technique. For a fixed photon flux this translates into shorter detection times. At the same time, the new technique is simple to apply in existing imaging devices, such as telescopes, microscopes, or spectrometers.

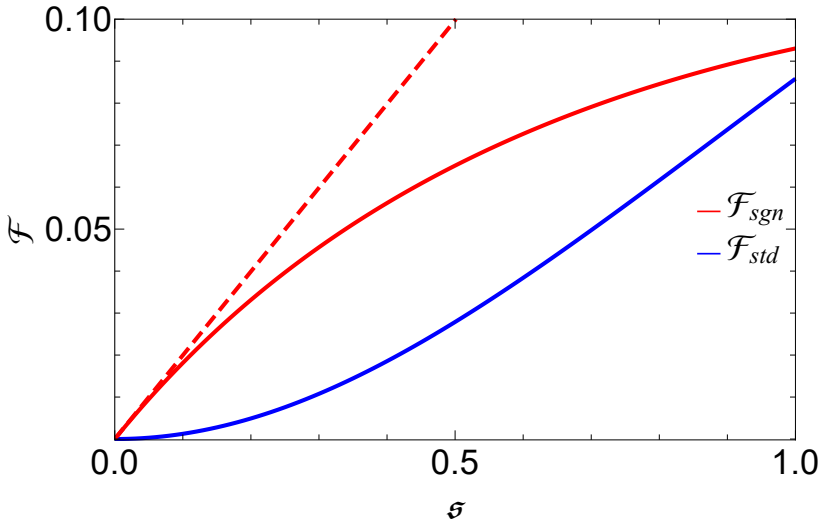

Figure 5.3: Fisher information about separation for imaging with a Gaussian PSF with (red solid line) and without (blue solid line) the signum filter. The asymptotic behavior of the superresolution given by the right-hand side of Eq. (5.10) is also shown (red dashed line.)

5.3 Experimental realization

The method was implemented with the setup sketched in Figure 5.4. Firstly, it was necessary to prepare mutually incoherent equally bright point sources with the controlled separation. The linearly polarized He-Ne laser beam (Thorlabs) was transformed by a system of microscope objectives and optical fiber into a uniform collimated beam. This transformation was carried out with respect to the size of the DMD chip. After this transformation, the intensity-stabilization back-loop system was applied because of a transferred laser pointing effect. This system was performed by motorized half-wave plate sandwiched by 2 linear polarizers, 90:10 beamsplitter, and fast power meter. This loop holds the intensity fluctuations well below 1% of total incident power.

Spatially coherent Gaussian beam prepared in this way was used to illuminate a DMD chip (Texas instruments) with a micro-mirror pitch of 10 µm. Two sinusoidal grating pat-

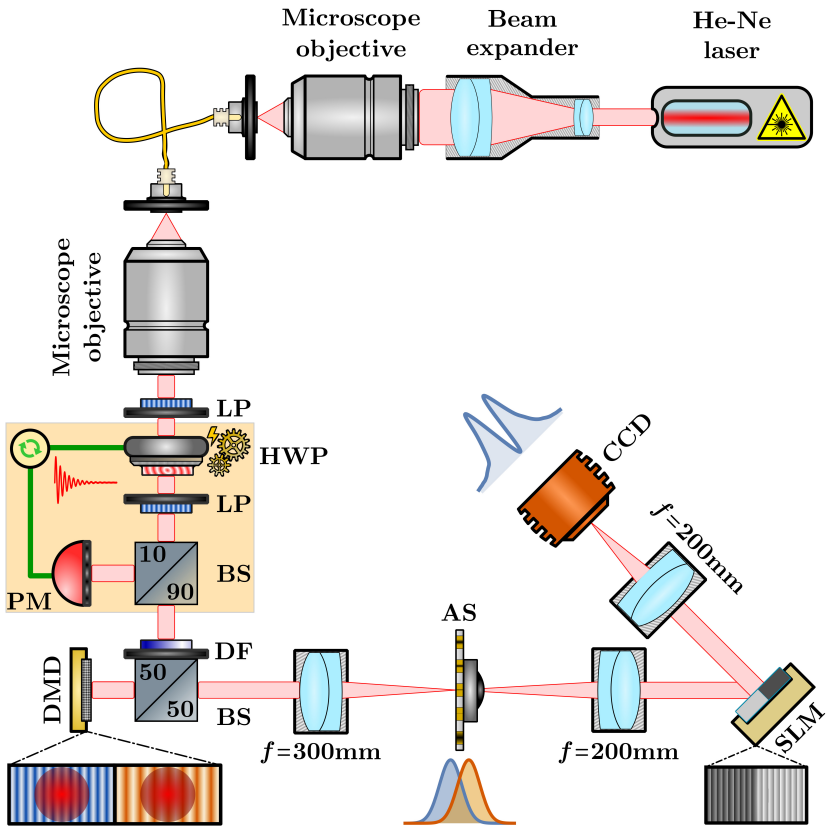

Figure 5.4: Experimental setup of the applied signum-enhanced protocol. The setup contains several substantial parts as uniform beam preparation, intensity stabilization, incoherent points preparation by DMD chip, $4f$ processor with the application of the signum filter by SLM, and CCD detection part. The abbreviated marks means: LP - linear polarizer, HWP - half-wave plate, BS - beamsplitter, PM - power meter, DF - density filter and AS - aperture stop.

terns with very close spatial frequencies were created, allowing very precise control of the angular separation in a chosen diffraction order. Resulting angular separations, with a minimal reached angle of 4.6 µrad corresponding to a linear separation of 0.042σ, were realized. To ensure incoherence between point sources, one pattern was ON at a time, while keeping the switching time well bellow the detector time resolution. Imaging with an objective of focal length $f = 300$ mm gave rise to two spatially separated Gaussian spots of $\sigma = 33.2$ µm. To cut off unwanted diffraction orders a standard aperture stop was used. This part completes the direct imaging stage.

In the signum-enhanced imaging part, a phase-only spatial light modulator (Hamamatsu) with square pixels of 20 µm $\times$ 20 µm was operated in the Fourier plane of a standard $4f$ optical system. The SLM implemented the signum mask hologram, calculated as an interference pattern between a phase unit-step and a blaze grating mask, allowing for over 0.9 optical transfer efficiency. Finally, the output signal was measured by a CCD camera

(Basler) with 7.4 µm $\times$ 7.4 µm pixels positioned at the output of the $4f$ processor. Because of the higher readout noise of the camera, we activated the vertical four-pixel binning regime. This regime effectively sums the charge in a specific number of pixels before the readout process and adds readout noise only once. The resulting effective pixel size was 7.4 µm $\times$ 29.6 µm. The corresponding signals used in the reconstruction process, resulting from summing three pixels, were in the range of $120 - 253$ photoelectrons in comparison to a sum of 3×7 photoelectrons readout noise. The camera exposure time was set to 100 ms to keep dark noise contribution negligible.

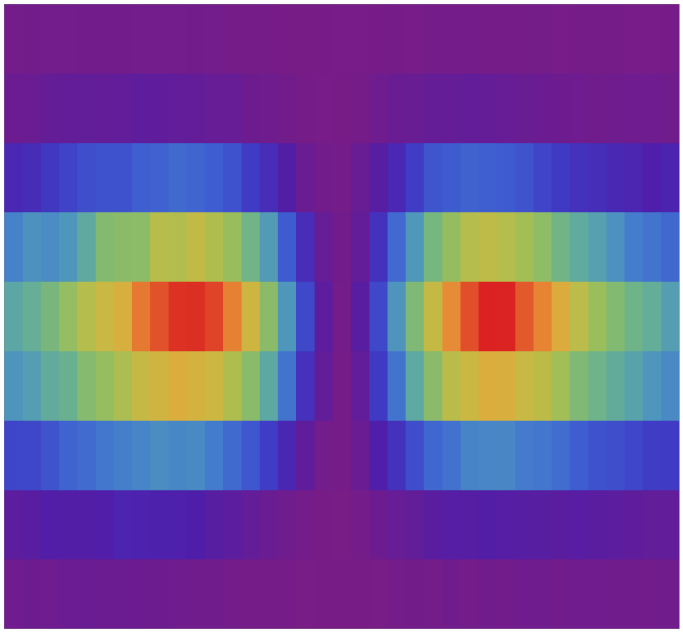

Figure 5.5: Example of the detected signal with a four-pixel binning regime. The resulting separation is estimated from the total number of detections registered in the central pixel column.

5.4 Results and discussion

To proof our model and setup several separations, ranging from about 0.042σ (1.4 µm) to 0.18σ (6 µm) were measured. For each separation setting, 200 intensity scans were recorded. One typical 2D intensity scan is depicted in Figure 5.5. Since the two incoherent points are separated horizontally, no information about separation is lost by collecting pixel counts column-wise. The resulting projections are samples from the theoretical intensity distribution $\rho_{\mathfrak{s}}^{sqn}(x, \mathfrak{s})$. Regarding small separations and conclusions from Figure 5.2, only the central parts of the projections contribute significant information. In particular, all pixel columns, except the central one, can be ignored in the raw data in Figure 5.5. Therefore,

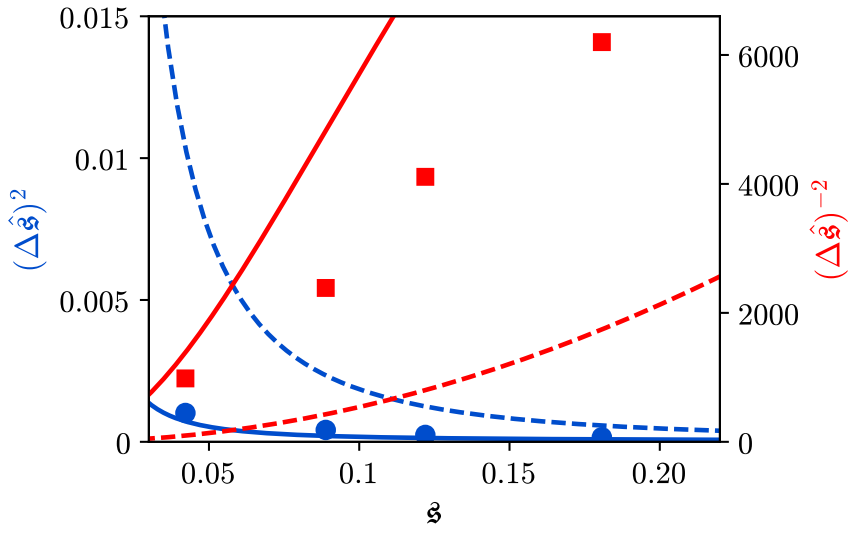

Figure 5.6: Experimental variances of the separation estimator (blue dots) compared with the direct detection (blue dashed lines) and the signum-enhanced limit (solid blue line). The latter is corrected for the finite pixel size of 7.6 μm. For completeness, the reciprocal of the variances, called precisions, are shown in red.

each 2D intensity scan is reduced to a single datum - the total number of detections in the central pixel column.

We expressed the response of the real measurement by a second-order polynomial on the separation $p(\mathfrak{s}) = a + b\mathfrak{s}^2$ and estimated the coefficients from the best fit of the mean experimental detections. For each separation, we calculated the estimator mean $\langle\hat{\mathfrak{s}}\rangle$ and variance $\langle\Delta\hat{\mathfrak{s}}^2\rangle$.

Experimental results are summarized in Figures. 5.6 and 5.7. Figure 5.6 compares the experimentally determined variances with the theoretical limits of the direct and signum-enhanced imaging for a Gaussian PSF and 434 000 detections per measurement. Reciprocal quantities (precisions) are also shown. Signum-enhanced imaging clearly breaks the quadratic Rayleigh curse in the whole range of measured separations, with variance improvements up to $10\times$ compared to the direct imaging. Note also the apparent linear behavior of experimental precision (red symbols) as compared to the quadratic lower bound predicted for the direct imaging (red dashed line).

Figure 5.7 shows more estimator statistics. Experimental estimates are nearly unbiased and not much worse than the theoretical limit calculated for the finite pixel size used in the experiment. The PSF engineering brings reliable separation estimates in the region, where direct imaging fails, as for example for separations $\mathfrak{s} \simeq 0.07\sigma$ in Figure 5.7.

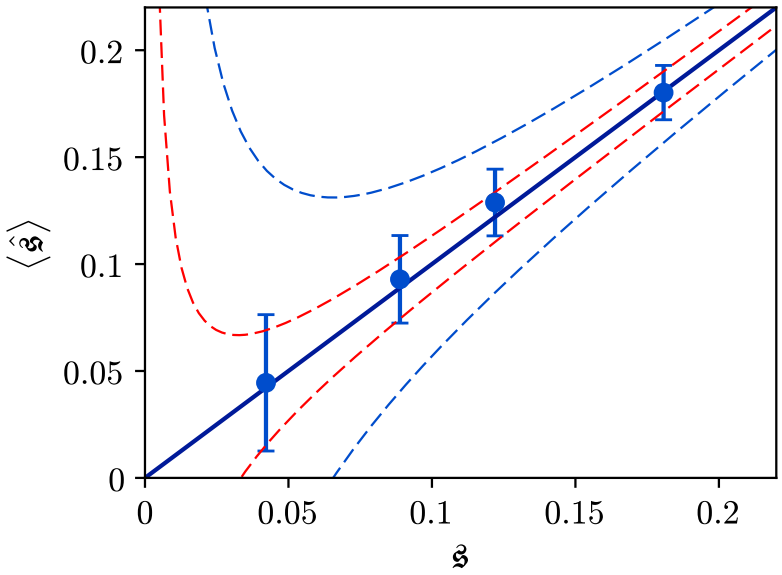

Figure 5.7: Estimation of the separation from signum-enhanced imaging. Estimator means (blue dots) and standard deviations (error bars) are shown. The same statistics are provided for the best unbiased estimators from direct (blue dashed lines) and signum-enhanced (red dashed lines) imaging as given by CRLB. The latter takes into account the finite size pixel used in the experiment.

In summary, we have demonstrated a robust experimental violation of Rayleigh's curse. Experimental imperfections prevent one from achieving the ultimate limit shown in Figure 5.3. For larger separations, systematic errors and setup instability make important contributions to the total (small) error. For very small separations, the measured signal is very weak and background noise becomes the limiting factor. Further improvements are possible by optimizing the noise statistics and resolution of the camera. Finally one could wonder whether a different filter could yield better scaling of the Fisher information using direct imaging. The dispersion relations suggest that this behavior is largely determined by the zeros of the PSF [161]. To explore all these issues, the deeper survey is needed, but the simplicity of the signum mask makes it very attractive for superresolution applications.

Chapter 6

Reading out Fisher information from the zeros of the PSF

This chapter is based on following publication:

[3] M. Paúr, B. Stoklasa, D. Koutný, J. Řeháček, Z. Hradil et al. '*Reading out Fisher information from the zeros of the point spread function*'. In: *Optics Letters* **44.12** (2019), pp. 3114–3117.

In the previous chapter we showed, that any well-behaved symmetric PSF can be easily converted into PSF with a single isolated information-rich zero region using a simple non-absorbing signum filter. Using this new PSF, the Fisher information one can gain about the separation between two incoherent point-like sources does not scale quadratically with the decreasing separation but only linearly. Moreover, the dominant contribution of the separation information comes from the area in the vicinity of this zero region.

In this chapter, we are extending this idea of isolated zeros. We demonstrate, that any optical system, whose PSFs exhibit those natural zeros, makes the Fisher information fall linearly for small separations. We focus on sinc PSF, which has a large number of natural zeros. We experimentally confirm the idea of linear scaling and demonstrate this behavior using two simple spectroscopic setups with naturally and artificially created spectral doublets.

6.1 Theoretical background

To establishing our model, we can follow the same theoretical model as in section 5.1 in the previous Chapter. For lucidity, we would like to remind the resulting Fisher information density, which is defined as $\mathcal{F}_{std}(\mathfrak{s}) = N \int_{-\infty}^{\infty} \mathfrak{F}\,(x|\mathfrak{s})\,dx$

$$\mathfrak{F}(x|s) = \frac{\mathfrak{s}^2\,[I''(x)]^2}{16I(x)} + O(\mathfrak{s}^2), \tag{6.1}$$

where the leading term is quadratic in $\mathfrak{s}$. When $I(x)$ is a Gaussian function with no zeros, which is often used as a pretty good approximation to the Airy distribution, integrating over x persists the same scaling of the Fisher information. However, this is not always the case.

Let us assume that the PSF has second-order zeros at a positions x_k ($k = 1, 2...$). This is a natural assumption due to the analyticity of the associated complex amplitudes around such points. In this case, the Fisher information exists only as the Cauchy principal [162]. Consequently, the power expansion of the integral around $\mathfrak{s} = 0$ does not make any sense, since it cannot be integrated term by term. Instead, one should find the dominant term of the integrand near the kth zero by locally approximating $I(x)$ with $\frac{1}{2}I''(x_k)(x - x_k)^2$. This finally gives

$$\mathfrak{F}(x|s) = \frac{1}{8}\frac{I''(x_k)\mathfrak{s}^2}{(x - x_k + i\mathfrak{s}/2)(x - x_k - i\mathfrak{s}/2)}, \tag{6.2}$$

which is true for $\mathfrak{s} \ll 1$. By analytic continuation to the complex plane, each zero x_k gives rise to two simple poles symmetrically placed with respect to the real axis $z_k^{\pm} = x_k \pm i\mathfrak{s}/2$. The integral in (4.4) can be evaluated by the method of residues [163]. We can deform the real axis inserting small semicircles that enclose the poles z_k^+. The leading terms are then the contributions from z_k^+, and since $2\pi i\mathrm{Res}(\mathfrak{F}, z_k^+) = \frac{1}{4}\pi I''(x_k)\mathfrak{s}$, the Fisher information appears as a sum of the contributions of all the poles and we get

$$\mathcal{F}_{sinc}(\mathfrak{s}) = \left[\frac{\pi}{4}\sum_k I''(x_k)\right]\mathfrak{s}. \tag{6.3}$$

This confirms a linear scaling of the information accessible with an imaging system, which directly stems from the existence of second-order zero regions of the PSF. As an example, we examine the normalized PSF

$$I(x) = \frac{1}{w}\frac{sin^2(\pi x/w)}{(\pi x/w)^2}, \tag{6.4}$$

which appears when dealing with the diffraction by a slit. Here, w is an effective width that depends on the used wavelength. This PSF has an infinite number of zeros located at $x_k = kw$ ($k = \pm 1, \pm 2, ...$), so that the associated Fisher information is

$$\mathcal{F}_{sinc}(\mathfrak{s}) = \left(\frac{\pi}{2w^3} \sum_{k \neq 0} \frac{1}{k^2} \right) \mathfrak{s} = \frac{\pi^3}{6w^3} \mathfrak{s}, \tag{6.5}$$

of which more than 60% ($6/\pi^2$) resides in the first ($k = \pm 1$) diffraction minima.

It is worth stressing that, in practice, deviations from the Poissonian statistics might occur. For example, on decreasing separation, an unavoidable small amount of a Gaussian additive noise component starts to dominate the Poissonian one,inducing a transition from a linear to a standard quadratic scaling at very small separations. The coarse graining due to detector pixelization leads to a similar effect. In the following, we assume that the parameters of the detection scheme are such that those effects can be ignored in the range of separations of interest.

To exemplify the theory suggested above, two spectroscopic setups were realized. Both setups tried to resolve two close spectral lines with wavelength separation well bellow the standard diffraction-limited resolution. Furthermore, each configuration tested the results in a different context.

6.2 Experimental configurations for resolving spectral doublets

In the first experiment, a spectral doublet generator with controllable separation between two lines was used. By varying the separation and repeatedly measuring it, the scaling of measurement error with the true separation was determined.

The experimental setup is sketched in Figure 6.1. The spectroscopic setup consisted of a swept-wavelength tunable laser (Superlum) with a central wavelength of $\lambda = 840$ nm, laser collimation optics, diffraction grating, focusing optics with rectangular aperture slit, and a detection CMOS camera. We set the laser to operate in two-wavelength modulation mode with modulation frequency $f = 1000$ Hz - two orders of magnitude above the detection camera exposure time, which allowed us to effectively generate equally bright doublets. The collimated laser beam was analyzed with a transmission diffraction grating with a groove density of 600 lines/mm working in the first diffraction order. The slit aperture of the focusing lens was set to catch $N = 1080$ grating lines, which translates into a standard spectral resolution limit of $\lambda/N = 0.77$ nm. Whereas the minimum wavelength separation

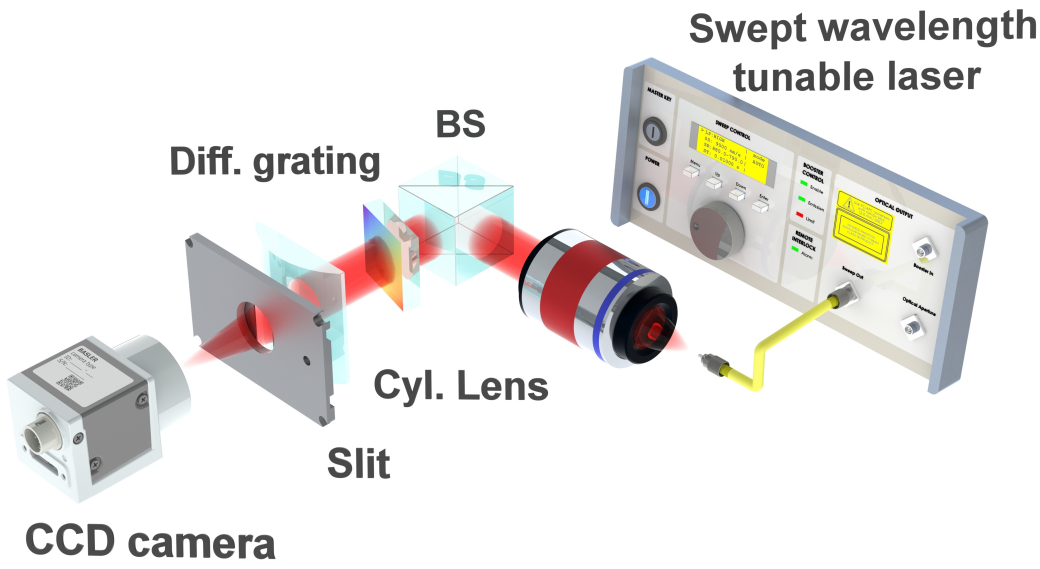

Figure 6.1: Experimental setup for measuring the spectral separation of artificial lines generated by a swept-wavelength tunable laser. BS - beamsplitter

achievable with the used laser was $\Delta\lambda = 0.05$ nm, which is about 15 times below the standard limit. Spectrograms generated at the focus of a cylindrical lens of focal length of $f = 250$ mm were recorded by a CMOS camera (Basler) with 1.67 µm $\times$ 1.67 µm pixels, with pixel capacity of 2000 electrons, and readout noise about 3 electrons. Due to the cylindrical symmetry, a data-set of separation estimates can be obtained from single-shot measurements by processing rows of the CMOS camera reading individually, which helps to avoid laser stability issues and other systematic errors.

The second experiment was aimed to resolving the longitudinal mode spacing of a laser cavity. Here, the gain curve of a linearly polarized He-Ne laser (Thorlabs) was characterized by the central wavelength $\lambda = 632.8$ nm, and the width that covers the cavity, the gain curve can start fluctuating above these modes. When the doublet centroid coincides with the maximum of the gain curve, two equally intense spectral lines would be emitted. A single spectral line is emitted, when centroid moves to the edge of gain curve. Switching between the single-line and two-line situation was done via an attached cooling fan. Output light was dispersed by a reflective holographic diffraction grating with a groove density of 2400 lines/mm, working in the first order with an angle of incidence of $49°$. A rectangular slit aperture of the focusing lens was set to catch $N = 12960$ grating lines corresponding to a spectral resolution of $\lambda/N = 48.7$ pm. The nominal cavity mode spacing of 1090 MHz equals to the wavelength difference of 1.45 pm, producing a separation 33 times below the standard resolution limit. The resulting spectrogram was recorded by the same CMOS camera as in the previous experiment, at the focus of a cylindrical lens of $f = 1000$ mm.

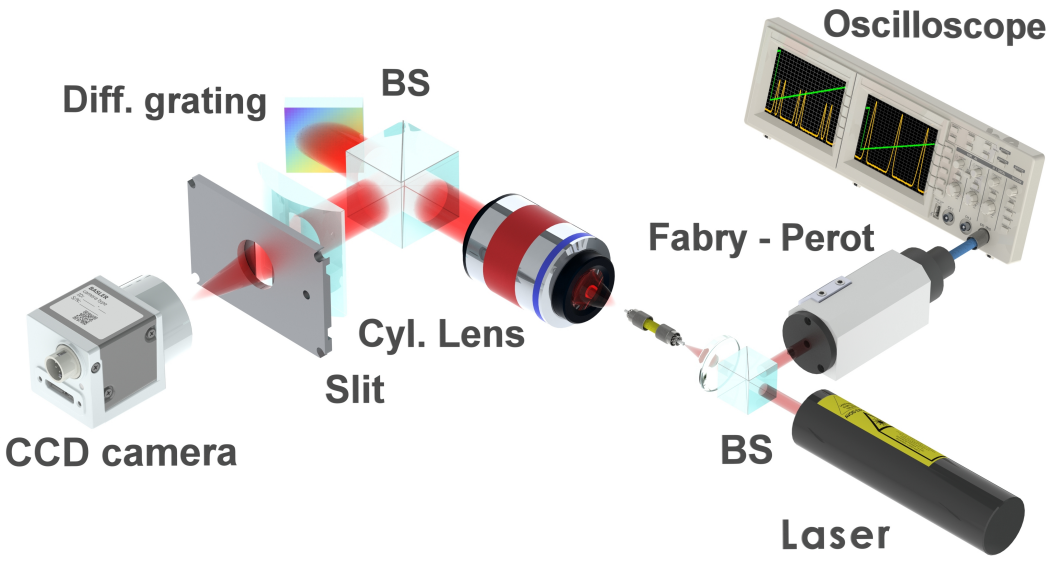

Figure 6.2: Experimental setup for resolving the longitudinal cavity modes of He-Ne laser. BS - beamsplitter

Moreover, the true doublet mode spacing and centroid were independently measured by a piezoelectrically controllable scanning cavity Fabry-Perot interferometer (Toptica) connected to an oscilloscope (Singlent), providing a free spectral range and resolution of 4 GHz and 10 MHz, respectively. The whole setup is schematized in Figure 6.2.

6.3 Results and discussion

With the first setup depicted in Figure 6.1, the spectral doublets were generated with a sinc PSF with $w = 114$ µm and true separations of $\mathfrak{s} = \{0.076, 0.15, 0.23, 0.31\}\, w$. An image was captured for each separation, and the total intensity was set such that each row contained $N = 50000$ detections on average. The data processed to yield an estimate $\hat{\mathfrak{s}}$ of true separation $\mathfrak{s}$ were the set of intensities (detections) registered at individual pixels in a given row. The relevant statistic was evaluated from 100 rows corresponding to repeated measurements on N copies of the signal state. The comparison of the experimental error to the theoretical bounds required scaling of the Fisher information with the number of total detections in the whole intensity pattern $F_{sinc}(\mathfrak{s}) \to NF_{sinc}(\mathfrak{s})$. The estimator $\hat{\mathfrak{s}}$ is obtained by a generalized least-squares technique implemented as a nonlinearly constrained optimization subject to $\hat{\mathfrak{s}} \geq 0$ [164]. Background and finite size of camera pixels are incorporated into the model. To illustrate the importance of zero intensity points, we processed the data both in global and local mode, as outlined in Figure 6.3. In the former case, a broad patch (extending from about $-2.4w$ to $+2.4w$) of the PSF was processed to estimate the total in-

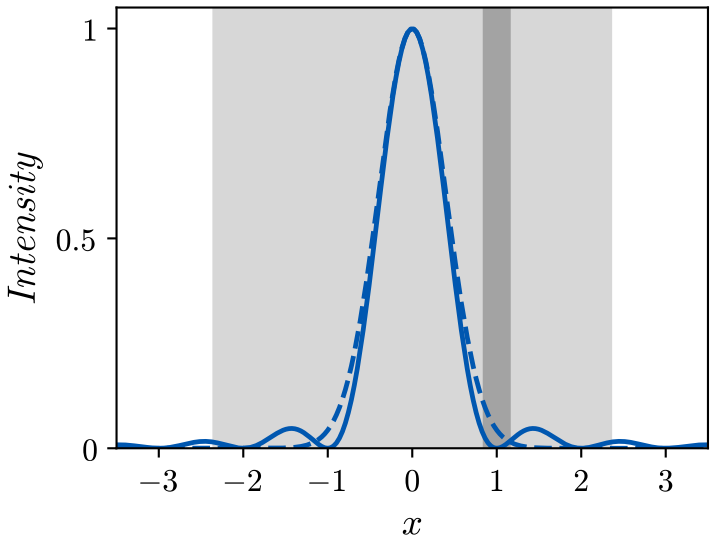

Figure 6.3: Sinc PSF, as given in Eq. (6.4), depicting the sensor areas that define global (light gray) and local (dark gray) measurements of spectral separation. The broken line represents a Gaussian PSF with the same normalization and the same peak value. The horizontal axis is drawn in units of w.

formation accessible in the data. In the latter case, only a small neighborhood of a single PSF zero was considered.

The results are summarized in Figure 6.4. We plotted precision $H(\mathfrak{s})$ [165] so that we avoid potential divergences as $\mathfrak{s} \to 0$. We can clearly appreciate the linear falloff and a significantly better resolution for very small separations obtained with the sinc PSF compared to what theory predicts for a strictly positive Gaussian PSF with roughly the same width, which drops at a much faster quadratic pace. The latter was calculated by numerically integrating the Fisher information equation with normalized Gaussian profile $I_{Gauss}(x) \propto exp\,[-x^2/(2\sigma)]$, where the Gaussian width σ was chosen to have equal peak intensity as the normalized sinc profile. Additionally, we compared the experimental results with their theoretical upper limits given by the Fisher information calculated for local and global measurements and Gaussian PSF. This clearly confirms that the local estimates are nearly optimal in the measured range of separations.

The moderate under-performance of global estimates seen in Figure 6.4 mainly stems from two factors. First, the realized PSF shows a slight asymmetry. The image half-plane with better (deeper) zero regions was selected for local measurements. The other half-plane only entered the global measurements. Second, for the largest measured separations, the theoretical resolution limits of a global estimation become a fraction of µm, which is already comparable to the level of the setup stability. Considering similar performances

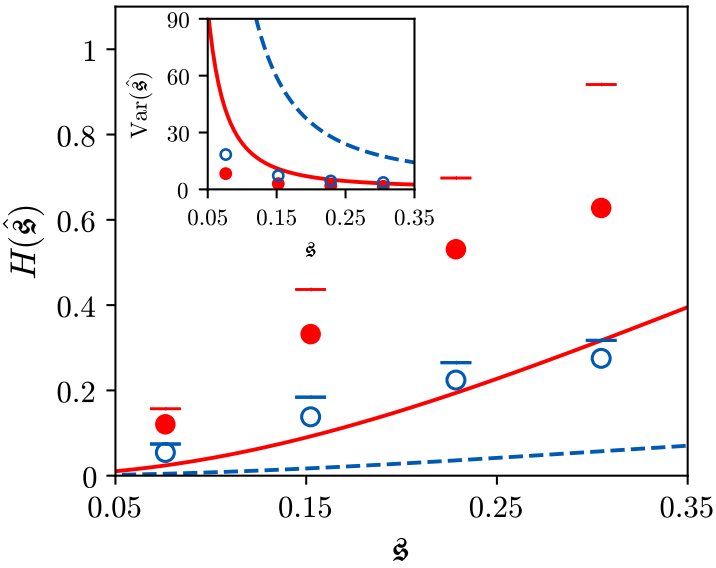

Figure 6.4: Experimentally determined precisions for the separation of two incoherent objects with a sinc PSF. The separation estimation was done globally (red solid symbols) from 322 pixels ($\sim 4.7w$) centered on the centroid of the intensity pattern encompassing four PSF zeros ($k = \pm 1, \pm 2$) or locally (blue open symbols) from 22 pixels ($\sim 0.3w$) cropped around a single $k = +1$ intensity minimum. The symbols are capped by the theoretical upper limits given by the Fisher Information. The red solid (blue broken) line shows the corresponding the theoretical limit such a global (local) measurement applied to a normalized Gaussian PSF of the same peak and total intensity. Variances are included in the inset for a clearer picture of what happens at very small separations. Precisions, variances, and separations are drawn in units of w^{-2}, w^2, w, respectively, and variances and precisions are normalized per photon detection in the full uncropped 1D image.

of the global and local estimates despite the huge difference in the number of detections, the experiment remains consistent with our main theoretical results, namely the bulk of information about small separations gets concentrated around the zeros of the PSF. Other parts of the image can be ignored, reducing the complexity of any post-processing manipulation, or not detected at all and used for other purposes, saving precious resources.

With the second setup represented in Figure 6.2, only two separations were measured, corresponding to single and double-line operation, making it difficult to characterize the measurement and establish the correct detection model. We estimated the true PSF of the setup from single-line data by averaging detections over an ensemble of 100 rows, and expressed the theoretical model in terms of the resulting PSF estimate $\hat{\mathbf{I}}(x_i) : \rho(x_i|\mathfrak{s}) = \hat{\mathbf{I}}(x_i - \mathfrak{s}/2) + \hat{\mathbf{I}}(x_i + \mathfrak{s}/2)/2$.

The robustness of the model follows from the absence of any unknown parameters - the double-line data being explained from the averaged single-line data and the latter serving as

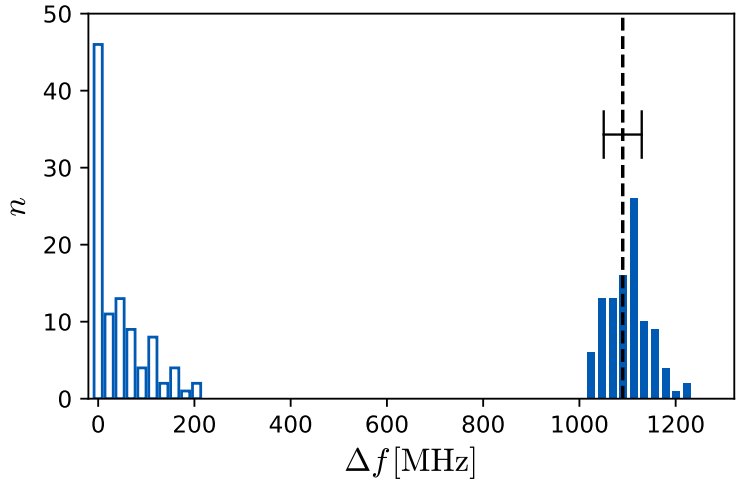

Figure 6.5: Histograms of experimentally determined frequency differences for single-line (open bars) and double-line (solid bars) He-Ne laser operation. The true separation of 1090 MHz of the spectral doublet is marked by the vertical broken line.

a null detection. We also made a cross-check by estimating the (nominally zero) single-line separations with the same model.

The results are condensed in Figure 6.5, where we show histograms of the separation estimates for each data set. The He-Ne doublet was clearly resolved with the best estimate of 1113 ± 44 MHz for two lines and 50 ± 57 MHz for a single line. Some positive bias seen in the single-line estimates was due to the strict enforcement of the physical constraint $\hat{\mathfrak{s}} \geq 0$, which become active at very small true separations.

In summary, we had provided a general argument, that links the zero regions of the PSF with the Fisher information and predicts a linear scaling. This can provide a significant advantage in terms of the resources required to measure very small separations, as we had demonstrated with two simple experiments. Moreover, this seems to call for appropriate engineering of the zeros of arbitrary PSFs (via suitable masks), to control the accessible information. In this sense, our results constitute a new concept of superresolution that requires very simple instrumentation.

Chapter 7

Intensity-based axial localization at the quantum limit

This chapter is based on following publication:

[4] J. Řeháček, M. Paúr, B. Stoklasa, D. Koutný, Z. Hradil and L. L. Sánchez-Soto. '*Intensity-Based Axial Localization at the Quantum Limit*'. In: *Physical Review Letters* **123.19** (2019), p. 193601.

In this chapter, we study overcoming classical precision bounds of single-point axial localization. In classical microscopy, the maximum spatial resolution is usually determined by the Abbe-Rayleigh criterion [14, 57]. However, this criterion is based on rudimentary notions, which are an inappropriate performance measure for current quantitative imaging [154].

Indeed, several modern techniques falling into the category of superresolution microscopy [58, 60, 65] are capable of achieving an increased resolution by more than one order of magnitude in comparison with the scale set by the Abbe-Rayleigh criterion.

For 3D imaging, the knowledge of the emitter axial position is also important. Finding the optimal depth precision attainable by any such microscope engineering approach has been only recently investigated [74, 166, 167]. The basic idea is to use the quantum Fisher information and QCRLB to find a measurement-independent limit, much in the same temper as was done in previous chapters.

Here, we present the fundamental precision bounds of single-point axial localization derived for Gaussian beams. These ultimate limits can be strikingly reached with a single intensity scan, provided by the camera placed at one of two optimal transverse detection planes. This prompts for axial localization, there is no need for more complicated detection schemes. The theory was verified with an experimental demonstration of axial resolution three orders of magnitude below the depth of focus, using a simple microscopy setup.

7.1 Theoretical background

Once again, we focus on direct imaging, which is the simplest method available in the laboratory. Of course, as we mentioned in Chapter 4 and proved in Chapters 5 and 6, discarding the phase information is not the proper way how to get beyond the standard resolution limits. Surprisingly, in this optical scenario, it can be shown, that the direct detection scheme can saturate the quantum limits with a single intensity scan, as long as the camera is placed in an optimal transverse detection plane.

To simplify our theoretical model, we take the waist of a focused beam as the object. The challenge is to estimate the distance from this object to a detection plane. To generalize the theory, we shall use the Dirac notation to describe the field and extent it to any type of possible light source.

If the beam in the object plane is represented by the pure state $|\Psi(0)\rangle$, the axial displacement can be described by a unitary operation $|\Psi(z)\rangle = e^{iGz}|\Psi(0)\rangle$, where the Hermitian operator G being the corresponding generator. To clarify the action of G in a more accurate way, it is convenient to use the transverse-position representation $\Psi(x,y;z) = \langle x,y|\Psi(z)\rangle$. Given our unitary parametrization, it holds

$$\partial_z \Psi(x,y;z) = iG\Psi(x,y;z), \tag{7.1}$$

which is consistent with the paraxial wave equation $2ik\partial_z\Psi(x,y;z) = \nabla_T^2\Psi(x,y;z)$ if $G \to \frac{1}{2k}\nabla_T^2$. For more tractable analysis and experiment, we assume a normalized Gaussian beam in the form

$$\Psi(r;z) = \frac{\sqrt{2}}{\sqrt{\pi}w(z)} e^{-\frac{r^2}{w^2(z)}} \exp\left(-i\left[kz + \frac{kr^2}{2R(z)} - \phi(z)\right]\right). \tag{7.2}$$

Although the final results are independent of this choice. Notice, that using the cylindrical symmetry, the beam depends on the radial coordinate r exclusively. The field distribution in Eq. (7.2) is determined by the beam waist w_0 and the Rayleigh range z_R through $w^2(z) = w_0^2\left[1 + (z/z_R)^2\right]$, $R(z) = z\left[1 + (z_R/z)^2\right]$, $\phi(z) = \arctan(z/z_R)$, and $z_R = \pi w_0^2/\lambda$, where detection plane is placed in z position. To enumerate the information about z available in the measured signal we use the quantum Fisher information, which, for our case of pure states, is given by $\mathcal{F}(z) = 4\mathrm{Var}(G)$, where Var is the variance computed in the initial state. With the standard form of G in the transverse representation, a direct calculation shows that for the Gaussian beam one gets

$$\mathcal{F}(z) = \frac{1}{z_R^2}, \tag{7.3}$$

which reveals to be a constant. Moreover, the QCRLB [167] assures, that the resulting variances of any unbiased estimator $\hat{\mathbf{z}}$ is bounded by reciprocal of quantum Fisher information.

7.2 Direct detection and saturation of quantum limit

The basic model of detected light is generally described by the probability density function, which in our case is interpreted by normalized beam intensity $\varrho(r|z) = |\Psi(r;z)|^2$. Since the detection is a random process, the shot noise is a limiting factor, obeying the Poisson statistic. Ignoring most of the non-classical effects, which are neglectable for applied microscopy, and oversight the finite spatial extent and nonzero pixel size, the resulting standard Fisher information about z in polar coordinates and for single detection can be written as

$$\mathcal{F}_{std}(z) = \left[\frac{\partial_z w^2(z)}{w^2(z)}\right]^2 = \frac{4}{R^2(z)} = \frac{4}{z^2\left[1+(z_R/z)^2\right]^2}. \tag{7.4}$$

Regarding this result, the optimal detector positions are at the Rayleigh range $z_{opt} = \pm z_R$, which are the planes of the maximal wavefront curvature. Also, at these optimal planes, the Fisher information saturates the quantum limit, i.e., $\mathcal{F}_{std}(z_R) = 1/z_R^2$ and confirms, that all information about axial waist localization is coded in the intensity distribution and can be extracted with conventional direct measurement without more complicated techniques.

Potential applications of this consequence profit from using a relay optical system to reimage the object and obtain a more suitable detector position. Figure 7.1 sketches one of the simplest possible schemes using a thin lens placed at distance z from the waist of the object beam. Here the plane (prime) symbols characterize parameters in object (image) plane.

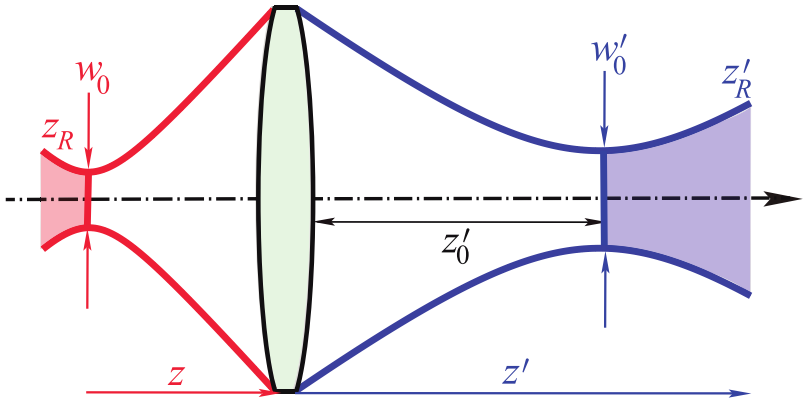

Figure 7.1: Scheme of the axial localization setup using a simple relay optical system.

In consideration of the unitary transformation of an ideal imaging system, the quantum Fisher information does not change from the object to image space, i.e., $\mathcal{F}' = \mathcal{F}$. Recapping the standard relations for Gaussian beam lens transformation [168]

$$w_0'^2 = m^2 w_0^2, \qquad z_R' = m^2 z_R, \qquad z_0' = m^2(z-f)+f, \tag{7.5}$$

where $m = f/\left[(z-f)^2 + z_R^2\right]^{1/2}$ is the magnification of the system, we can find new beam width at the detection plane z' as

$$w'^2(z') = w_0'^2\left[1 + \left(\frac{z'-z_0'}{z_R'}\right)^2\right]. \tag{7.6}$$

And the associated Fisher information is express in term

$$\begin{aligned}\mathcal{F}'_{std}(z) &= \left[\frac{\partial_z w'^2(z)}{w'^2(z)}\right]^2 = \\ &= \frac{4(f-z')^2\left[zz' - f(z+z')\right]^2}{\left\{(z^2+z_R^2)z'^2 - 2fz'(z^2+z_R^2+zz') + f^2\left[(z+z')^2+z_R^2\right]\right\}^2}.\end{aligned} \tag{7.7}$$

The characteristic distribution of $\mathcal{F}'_{std}$ around the beam waist w_0' is displayed in Figure 7.2 with the presence of two asymmetric maxima (saturating $\mathcal{F}'$) and one minimum $\mathcal{F}'_{std,min} = 0$. While the beam is symmetric about the waist in the image area, the response of the beam width to small changes of the true distance z is different inside and outside the waist, which makes the Fisher information asymmetrical with respect to the image waist. These maxima are located at

$$z'_{opt} = z_0' + \alpha z_R', \qquad z'_{opt} = z_0' - \frac{1}{\alpha} z_R', \tag{7.8}$$

where $\alpha = (f - z - z_R)/(f - z + z_R)$. Nevertheless, in the geometrical limit $f - z \gg z_R$, we get $\alpha \simeq 1$ and optimal planes are in the Rayleigh range of the beam, so the asymmetry disappears.

We should also take notice of the single minimum at $z'_{min} = fz/(z-f)$, where the information about axial displacement tends to zero. This behavior is closely adherent to the information about transversal beam localization. In this situation, a small lateral shift Δr of a Gaussian object of width w_0 leads to the corresponding lateral shift of $\Delta r' = [(f-z')/f]\Delta r$ of the detected Gaussian profile. A straightforward calculation can show that the resulting $\mathcal{F}'_{std\Delta r}$ about Δr is maximized by placing the detector into the plane of the geometrical image z'_{min}, where the quantum limit is achieved $\mathcal{F}_{\Delta r} = 1/w_0^2$. In this sense, the optimal axial localization (requiring considerable image blur) and transverse localization

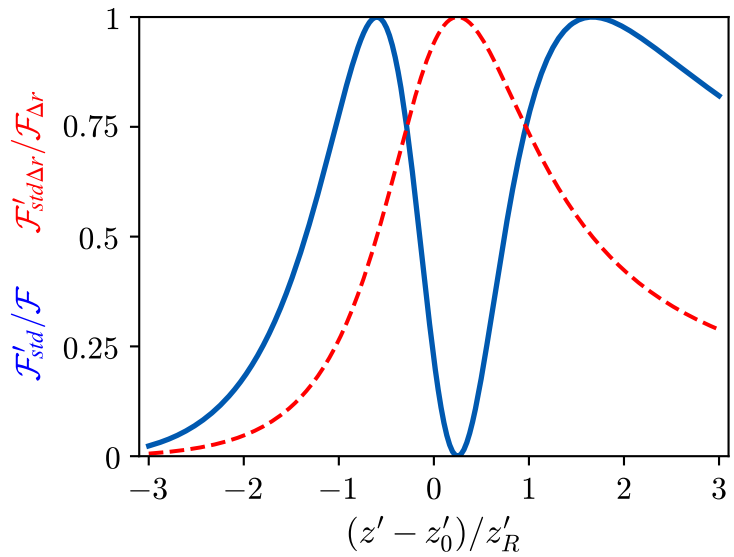

Figure 7.2: Image space Fisher information distribution of axial (blue solid) and transversal (red broken line) positions of the object beam waist. Curves are normalized respective to the quantum Fisher information for different placements of the detector. For chart, the parameters $z = 5$, $f = 1$, and $z_R = 1$ were used and the x-axis is relative to beam waist in units of z'_R.

(benefiting from sharpness) complement each other, as can be checked in Figure 7.2. The equilibrium between these two components can be reached through PSF engineering, which provides a good three-dimensional resolution. Therefore, these methods always broaden the PSF, even more than our z_R defocusing method.

7.3 Experimental Realization

To validate the above-mentioned theory, we invoked a classical microscopy setup, as schematized in Figure 7.3. The setup was constructed from an objective (Olympus) corrected for infinity and a tube lens (Thorlabs), all together providing a $20\times$ magnification of the output end of a single-mode fiber representing a Gaussian point-like source. The fiber was coupled with a 632.8 nm He-Ne laser (Lasos). The Used fiber had mode field diameter around 4 µm and the corresponding Rayleigh range was then 18.9 µm. Used CMOS camera (Basler) with 5.5 µm pixel size was moved 7.6 µm out of the image beam waist to become aligned with one of the optimal detection planes given by Eq. (7.8). The axial distances z of fiber were realized by the translation stage (Thorlabs) with a piezo actuator controlled by the close-loop tensometer with a resolution of 1 nm.

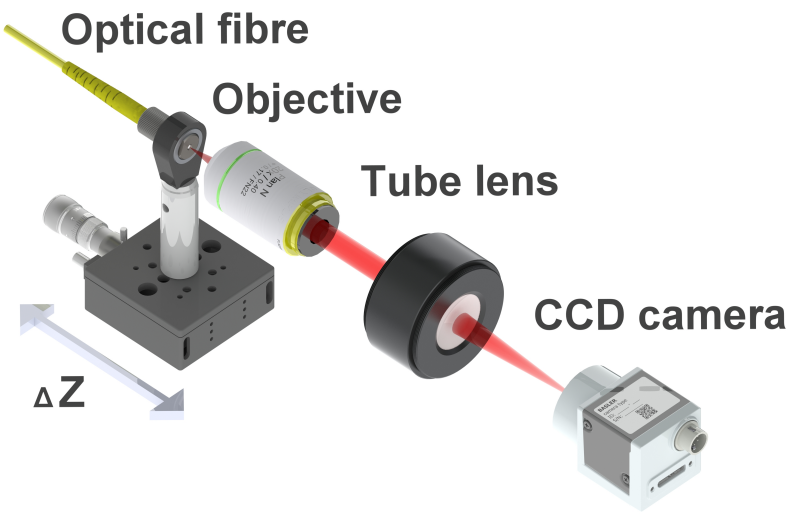

Figure 7.3: An experimental setup used to measure the axial displacement z of an optical fiber. The output face of the fiber served as the point-like Gaussian source, which was linearly transformed by a microscope composed of an objective and a tube lens. The camera was positioned in one of the optimal detection planes to obtain the maximum of the available information.

To construct the most robust estimator, it is convenient to compare radial Fisher information density with the normalized Gaussian beam intensity profile in the image plane. These magnitudes are shown in Figure 7.4 for the optimal detection plane z'_{opt}. The information falls to zero at $r_b = w'_{opt}/\sqrt{2}$ and the amount of information ($2/e \simeq 74\%$) resides outside this bound in the remaining segment of the Gaussian intensity distribution. The residual intensity outside this boundary can be labeled as $I_{det}(z)$, for the axial object distance z. Then, for small displacement δ_z from nominal position z, we have

$$I_{det}(z + \delta_z) I_{det}(z)(1 - \delta_z/z_R). \tag{7.9}$$

This linear definition can be easily transposed to acquire an estimate $\hat{\delta}_{\mathbf{z}}$ of δ_z from I_{det}.

Of course, we tried to use the maximum likelihood estimator based on the full profile. However, this estimator was a bit noisy due to the systematic errors [169]. Nonetheless it is important to remark, that we were interested in the proof-of-concept experiment, and our estimator from intensity I_{det} is simple and sufficient despite small deviations from the theoretical best performance.

We would like to notice, that we presumed the knowledge of the nominal axial distance. When this is not true, there can be the potential loss of precision in the z estimate due to

an inaccurate detector positioning. Naturally, this shouldn't be am overwhelming problem because one can perform a calibration process as we did in our experiment. Our calibration was done by placing the fiber forehead in the focal length of the microscope objective, which was our initial position $\delta_z = 0$. Afterward, the transformed beam waist w_0' was found, and the resulting parameters, i.e., z_R' were calculated. When this is not applicable, one can adopt an adaptive approach, where a small part of total detections (photons) is allocated on a nonoptimal detection, and the optimal detector position is corrected in according to the first estimation of z. This process can be iteratively repeated until the optimal plane is reached.

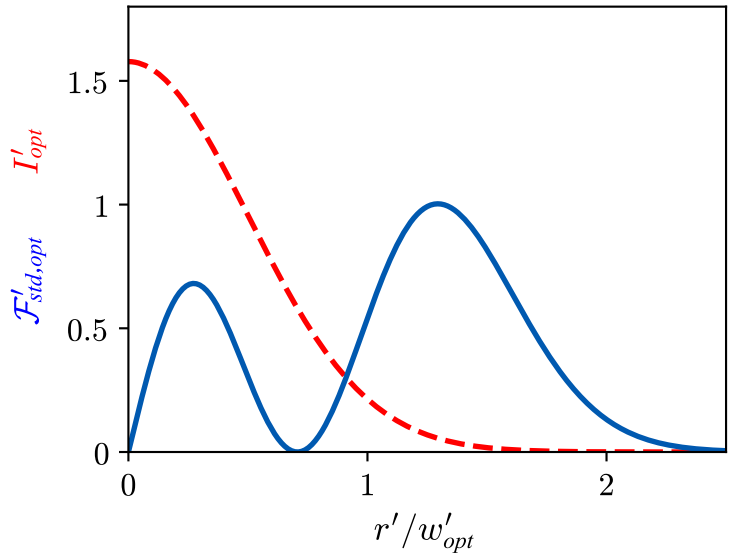

Figure 7.4: Normalized radial Fisher information density (solid blue line) and normalized beam intensity profile (dashed red line) in the optimal detection plane, where the beam has a width w'_{opt}. Parameters of the curves correspond with parameters in Figure 7.2.

7.4 Results and discussion

Attained experimental results are summarized in Figure 7.5. We measured the full range of axial displacements $\delta_z \in [10\text{ nm}, 1650\text{ nm}]$ with increasing displacement between adjacent values. Measurement errors were consistent across the whole interval, averaging 24.8 nm. This is about $800\times$ well below the depth of focus z_R and slightly above the quantum limit of 14.9 nm matching the total number of 1.6×10^6 registered photons for each δ_z setting.

Now, let us investigate what happened when the source is *uncooperative*. In this scenario, the source generates a spherical (parabolic) wavefront, which after a radiating distance z enters an imaging system that truncates the unbounded wave with a pupil function. If

we consider the Gaussian pupil transmissivity of width w_l , the wave transmitted by this pupil holds on

$$U(x,y;z) = \sqrt{\frac{2}{\pi w_l^2}} \exp\left[-\frac{r^2}{w_l^2} + i\frac{kr^2}{2}\left(\frac{1}{z} - \frac{1}{f}\right)\right]. \tag{7.10}$$

The aperture state is not exactly axial propagation from the point source because pupil acts as a filter and the state should be renormalized. The process is not unitary anymore and the quantum Fisher information cannot be calculated in terms of the generator G. In contrast with Gaussian source, the resulting quantum Fisher information now reads

$$\mathcal{F}(z) = \frac{k^2 w_l^4}{4z^4}, \tag{7.11}$$

which intensely depends on the true distance z.

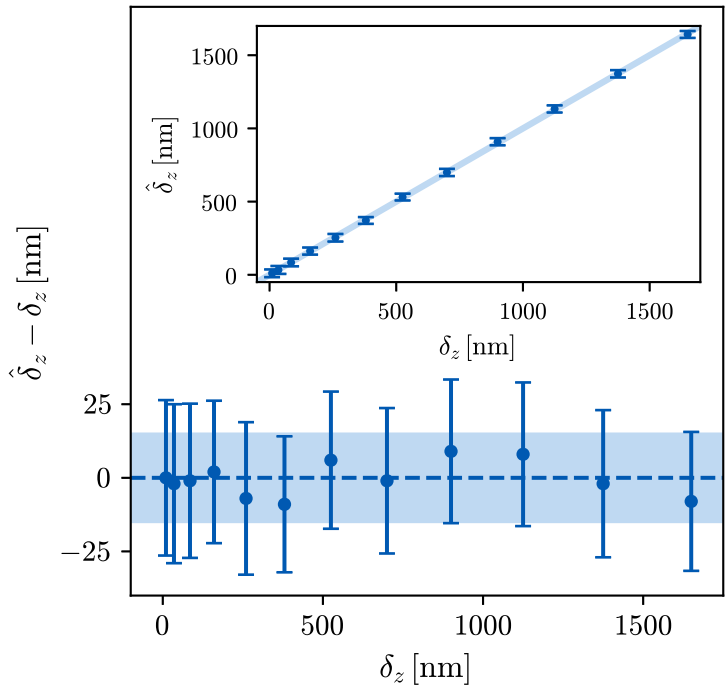

Figure 7.5: Experimental estimation of axial displacement δ_z from the nominal object plane with respect to optimally placed CMOS camera. The inset shows the statistic of the estimator $\hat{\delta}_\mathbf{z}$ as defined in Eq. (7.9). In the main plot, the true distance was subtracted from the estimates to get a more convenient scale on the vertical axis. The blue stripes depict the quantum bound for the 1.6×10^6 detections and $z_R = 18.9$ µm.

So far, we were interested in Gaussian beams and apodized lens. Now, it is intriguing to remark that $n = 2 \times 10^6$ detections, used in our experiment, detected with one meter aper-

ture $w_l = 1$ m in visible light $k = 10^7$ m^{-1} would theoretically provide axial localization of a point source in low Earth orbit $z = 200$ km with about 5 m accuracy.

In conclusion, we have theoretically and experimentally demonstrated the axial superresolution technique provided by a direct detection scheme. The quantum limits for Gaussian beams or apertures can be easily saturated with a single intensity scan, provided by the camera placed in one of two optimal transversal detection planes. For this reason, the axial localization problem does not need to adopt more complicated detection schemes. Our method makes 3D superresolution imaging promising and can be potentially useful for enhancing the resolution of optical microscopes.

Chapter 8

Unraveling beam self-healing

This chapter is based on following publication:

[5] A. Aiello, G. S. Agarwal, M. Paúr, B. Stoklasa, Z. Hradil et al. '*Unraveling beam self-healing*'. In: *Optics Express* **25**.**16** (2017), pp. 19147–19157.

In this chapter, we are concerned with the self-reconstruction mechanism of Gaussian beams. This extraordinary property, frequently called self-healing, leads to an overall reconstruction of the optical beam intensity profile after impinging on an opaque obstacle.

Self-healing has been considered as a peculiar attribute of non-diffracting beams [90], especially Bessel beams [103, 170, 171], Airy [172], caustic beams[123] and other special forms for a long time. Recently, a complete description of the self-healing mechanism for Bessel beams has been defined in terms of wave optics [127]. This makes the self-reconstruction process possible to reassign in terms of plane waves with radial wave vectors lying on the ring.

Here, we continue with wave-optics methodology, which leads us to the conclusion that self-healing property may potentially occur for almost any kind of beam, focusing primarily on common Gaussian beams. We introduce an appropriate degree that quantifies the similarity between the field of the unperturbed beam, a beam that would propagate as the obstacle is not present and the field of the perturbed one, the beam that propagates behind the obstruction. Moreover, we suggest a novel definition for the minimum reconstruction distance beyond geometric optics, applicable for any optical beam that concedes an angular spectrum representation. This is achieved via investigation of the entire spatial distribution of the beam, i.e., its intensity and phase segments.

We experimentally verify these novel metrics on a Gaussian beam, whose intensity and phase were measured by means of CCD camera and Shack-Hartmann wavefront sensor, showing an accurate agreement with the theoretical predictions.

8.1 Theoretical background

Firstly, we briefly introduce our theoretical model pursuing the wave optics methods, mainly angular spectrum representation. We anticipate a scalar field $\Psi(x, y, 0)$ propagating along the z-axis. Here, an obstacle can be considered any physical object that decreases the intensity of a light beam in a space-dependent manner without changing the phase and polarization state directly. This kind of obstruction can be characterized by an amplitude transmission function $t_O(x, y)$. The resulting amplitude of the obstructed field $\Psi_O(x, y, 0)$ in the initial plane $z = 0$ can be described as

$$\Psi_O(x, y, 0) = t_O(x, y)\Psi(x, y, 0). \tag{8.1}$$

Accordingly to the angular spectrum propagation [84], the amplitude of the field transmitted at a distance z from the initial plane can be expressed as the plane-wave superposition

$$\Psi_O(x, y, z) = \frac{1}{(2\pi)^2} \iint_{-\infty}^{\infty} \exp(i\boldsymbol{\rho} \cdot \boldsymbol{\kappa}) \exp(ik_z z) \left[\iint_{-\infty}^{\infty} \widehat{t_O}(\boldsymbol{\kappa} - \boldsymbol{\kappa'})\widehat{\Psi}(\boldsymbol{\kappa'}) \right] d^2\boldsymbol{\kappa}, \tag{8.2}$$

where bold symbols denote real ($\boldsymbol{\rho} = x\hat{\mathbf{x}}+y\hat{\mathbf{y}}$) and Fourier space ($\boldsymbol{\kappa} = k_x\hat{\mathbf{x}}+k_y\hat{\mathbf{y}}$) coordinate vectors. Wide hat symbols characterize corresponding spatial Fourier transform (angular spectrum) functions evaluated in the plane $z = 0$.

With respect to the Babinet principle [173], we can always define the transmission function t_A of an aperture complementary to the obstructed one, which holds the equation $t_O(x, y) + t_A(x, y) = 1$. Then the Eq. (8.1) can be rewritten to the form

$$\Psi_O(x, y, 0) = [1 - t_A(x, y)]\, \Psi(x, y, 0) \equiv \Psi(x, y, 0) - \Psi_A(x, y, 0). \tag{8.3}$$

Performing the squared absolute value of the above equation and integrating over the whole space, we get the average beam intensity at plane z

$$I[\Psi_0] = I[\Psi] + I[\Psi_A] - 2Re \iint_{-\infty}^{\infty} \Psi^*(x, y, 0)\Psi_A(x, y, 0)\, dxdy. \tag{8.4}$$

Generally, the self-healing capability of the beam conveys to recovering its amplitude or intensity profile after hitting an obstacle. Evidently, the ideal reconstruction is physically inaccessible. This is apparent from previous equation, where the consequent intensity of the transmitted field is reduced unless $I[\Psi_A] = 0$. Then, the Ψ_O can be approximated by the form

$$\Psi_0(x, y, z) \approx \lambda_0 \Psi(x, y, z), \qquad \forall z \geq z_0, \tag{8.5}$$

where z_0 denotes the so-called minimum reconstruction distance and the scaling factor $\lambda_0 = (I[\Psi_O]/I[\Psi])^{1/2}$ represents the average intensity reduction caused by an obstacle. This means that the Eq. (8.5) can be satisfied only by those beams, whose angular spectrum is unaffected by the interaction with the obstruction.

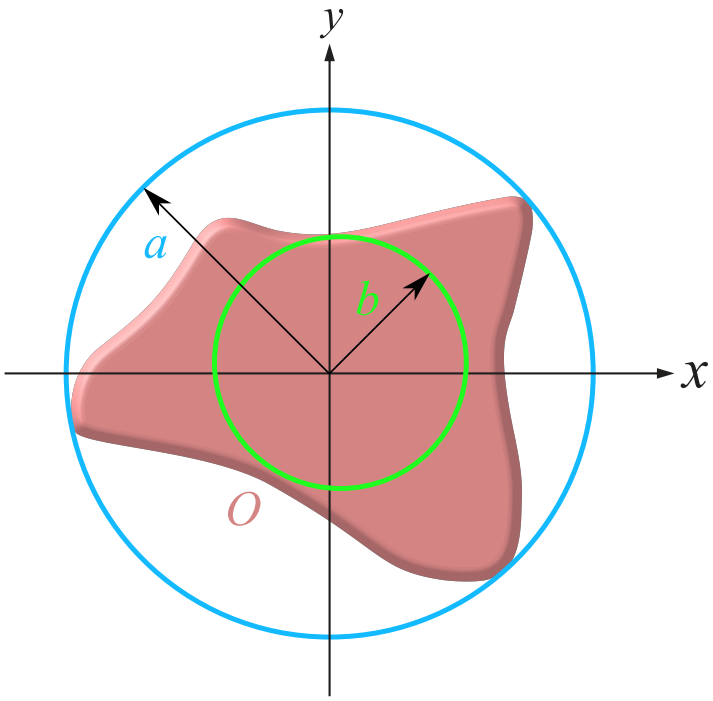

Figure 8.1: Obstruction of area O represented in red. This region is bounded by the blue circle of radius a (exradius) and inscribes the green circle of radius b (inradius). Both circles are centered along the z-axis of the beam

Let's take a closer look at a minimum reconstruction distance z_0, after which a self-reconstructing beam is supposed to reproduce its profile. Let us consider an arbitrary obstacle on the xy-plane with area O. This situation is sketched in Figure 8.1. For the simple enclosed region O, it can always be found the incircle (the largest circle inscribed O) with radius b and the excircle (the smallest circumscribed circle) with radius a, both centered on the axis [174]. Then fundamental considerations lead us to [104, 175]

$$z_0 \propto \frac{a}{\tan \phi}, \tag{8.6}$$

where the proportionality factor depends on the shape of the obstruction.

Naturally, we can rewrite the z_0 as a function of $\kappa = (k_x^2 + k_y^2)^{1/2}$ in the Fourier space namely

$$z_0 \sim aZ(\kappa) := a\frac{\sqrt{(k^2-\kappa^2)}}{\kappa}. \tag{8.7}$$

For an arbitrary beam, the transverse wave vector $\boldsymbol{\kappa}$ has a density distribution function given by $|\widehat{\Psi}(\boldsymbol{\kappa})|^2$. So, the minimum reconstruction distance can be formulated as the expected value of the function $Z(\kappa)$

$$\frac{z_0}{a} = \langle Z(\kappa)\rangle = \frac{\iint \frac{\sqrt{(k^2-\kappa^2)}}{\kappa}|\widehat{\Psi}(\boldsymbol{\kappa})|^2 d^2\kappa}{\iint |\widehat{\Psi}(\boldsymbol{\kappa})|^2 d^2\kappa}, \tag{8.8}$$

where both integrals ale limited to the disk $k_x^2 + k_y^2 \leq k^2$. This formula assigns a decisive value of z_0 to any density $|\widehat{\Psi}(\boldsymbol{\kappa})|^2$, which means that self-healing may occur for any beam.

8.2 Self-healing quantification of Gaussian beams

To test our suggested ideas, we choose the Gaussian beam as the simplest example. The Gaussian beam is an essential transversally unbounded (TEM_{00}) diffracting mode, which describes the typical output of most laser devices. Furthermore, the Gaussian beam is the fundamental solution of the paraxial wave equation, and it can be written as

$$\Psi(x,y,z) = \exp(ikz)\frac{1}{z-z_R}\exp\left[i\frac{k(x^2+y^2)}{2(z-iz_R)}\right], \tag{8.9}$$

where z_R is the Rayleigh range and w_0 beam waist. To simplify the enumeration, the soft-edge Gaussian obstacle of full width $2a$ and location at plane $z = 0$ can be assumed. This obstruction can be described by transmission function

$$t_O(x,y) = 1 - \exp\left(-\frac{(x-x_0)^2+(y-y_0)^2}{2a^2}\right), \tag{8.10}$$

where x_0 and y_0 represent the displacement of the obstacle with respect to the beam axis.

Concerning the above transmission function, we can define resulting complementary field Ψ_A namely as

$$\Psi_A(x,y,z) = \frac{a_R}{z_R}\frac{1}{z-ia_R}\exp\left[i\frac{k}{2}\left(\frac{x^2+y^2}{z-ia_R}\right)\right], \tag{8.11}$$

where we have defined the modified Rayleigh range a_R as

$$a_R = \frac{z_R}{1+\frac{z_R}{ka^2}} \leq z_R. \tag{8.12}$$

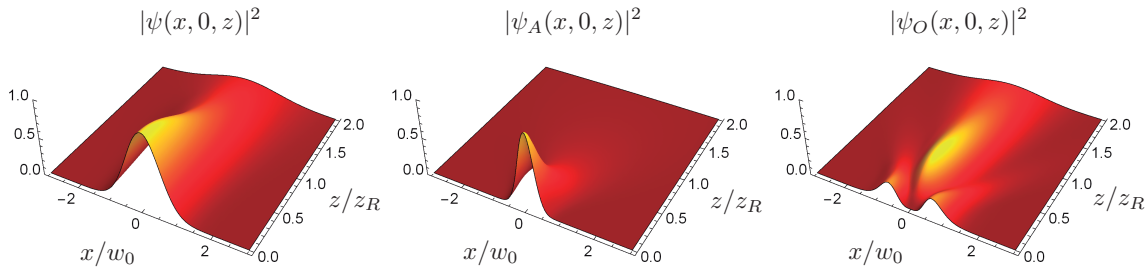

Figure 8.2: Intensity distribution (evaluated for $y = 0$) of the incident field $\Psi(x, 0, z)$, the complementary field $\Psi_A(x, 0, z)$ and obstructed one $\Psi_O(x, 0, z)$. The plots correspond to the Gaussian beam with $w_0 = 0.26$ mm and a soft-edge obstacle with full width $a/w_0 = 0.28$. At $z/z_R = 2$ the obstructed field embodies a very good degree of self-reconstruction.

The self-healing mechanism of the Gaussian beam is unambiguously depicted in Figure 8.2. Upon closer examination of this figure, we can clearly identify how the self-reconstruction process works. The requirement $a_R \leq z_R$ from Eq. (8.12) means that the complementary field $\Psi_A(x, y, z)$ during the propagation along the z-axis spreads much more rapidly than the unperturbed field $\Psi(x, y, z)$. For distance $z = 2z_R$, the intensity profile of the obstructed beam almost matches the profile of unperturbed one.

The reconstruction distance z_0 can be analytically found from Eq. (8.8). After evaluating the integrals, we get final result

$$\frac{z_0}{a} = \frac{\pi}{2\theta_0^2} \frac{I_0(1/\theta_0^2) + I_1(1/\theta_0^2)}{\sinh(1/\theta_0^2)}, \tag{8.13}$$

where $\theta_0 = 2/(kw_0)$ is the divergence of the beam and $I_x(z)$ is the modified Bessel function of the first kind of order x. In the paraxial regime $\theta_0 \ll 1$, z_0 can be approximated as

$$\frac{z_0}{a} \approx \frac{\sqrt{2\pi}}{\tan\theta_0}, \tag{8.14}$$

which is equivalent to our geometrical prediction in Eq. (8.6). It is good to note that z_0 is larger for smaller θ_0, which is caused by the connection of beam divergence and Rayleigh range z_R.

Nevertheless, it is useful to remind, that the concept of self-healing and minimum reconstruction distance suffer from impossible simultaneous satisfaction of (8.1) and (8.5) in the whole xy-plane. In other words, if the (8.5) is satisfied at specific distance z, in plane $z = 0$ this cannot be true by definition $\Psi_0(x, y, 0) = t_O(x, y, 0)\Psi(x, y, 0) \neq \Psi(x, y, 0)$.

Then, as an indispensable condition, we need to restrict the area where these equations should be satisfied. This arises because of an imperfect self-healing, where the beam shape becomes more like what it would have been without the obstacle because the influence of obstacle promptly vanishes.

Now, we need to define a metric that somehow quantifies the similarity between the obstructed and the unobstructed field. In quantum information theory [176], there are many possibilities of how to measure the *closeness* of two normalized states. Probably one of the most popular is fidelity, as may the application of a modified version in the context of self-healing [126] indicate. However, the standard fidelity fails to afford a quantitative description of self-healing because of integration upon the whole xy-plane, which erases the z-dependence.

Here, we apply a metric in the notion of relative distance, which can be defined as

$$\mathbb{D}_r(\Psi, \Psi_O) = \frac{\parallel \Psi - \Psi_O \parallel}{\parallel \Psi + \Psi_O \parallel} = \frac{\langle \Psi_A | \Psi_A \rangle^{1/2}}{[\langle \Psi_A | \Psi_A \rangle + 4 \langle \Psi | \Psi \rangle - 4\mathrm{Re} \langle \Psi | \Psi_A \rangle]^{1/2}}. \tag{8.15}$$

A direct application of the parallelogram law [177] [$\parallel f - g \parallel^2 + \parallel f + g \parallel^2 = 2(\parallel f \parallel^2 + \parallel g \parallel^2]$) immediately confirms that $0 \leq \mathbb{D}_r^2 \leq 1$. Moreover, considering Eq. (8.5) and assuming $0 \leq \lambda_0 \leq 1$, the relative distance can be simplified to the form

$$\mathbb{D}_r(\Psi, \Psi_O) \approx \frac{1 - \lambda_0}{1 + \lambda_0}. \tag{8.16}$$

In the sense of previous results, it is convenient to define a z-dependent degree of self-healing as follows

$$D_{SH}(z) = \sqrt{1 - \mathbb{D}_r^2(\Psi, \Psi_O)}. \tag{8.17}$$

We would like to emphasize that this concept of distance measure has been successfully applied in numerous fields of quantum optics [177–180]. In general, this type of metric quantifies how two physical states behave in the same way.

For a Gaussian beam with cylindrical symmetry, the degree of self-healing can be computed analytically and expressed in the asymptotic form

$$D_{SH}(z) = \zeta \sqrt{[\frac{1 - \beta^2}{\beta^2 + \zeta^2}}, \tag{8.18}$$

where we have used the dimensionless variables $\zeta = z/z_R$, $\alpha = a/w_0$ and $\beta = \alpha^2/(1+\alpha^2)$.

8.3 Experimental realization

The previous theoretical predictions were checked in the laboratory. The main prompt was in a generation of the Gaussian beam with a central obstruction. Our setup was based on the He-Ne laser (Thorlabs), where the outgoing Gaussian beam illuminated DMD chip (Texas instruments) with square micromirrors of 7.6 μm size each. The obstruction was generated as an off-state region on this chip. Then, the reflected beam propagated back through the beamsplitter and the resulting complex amplitude was subsequently measured by CCD camera and Shack-Hartmann (S-H) wavefront sensor. A sketch of the setup is presented in Figure 8.3.

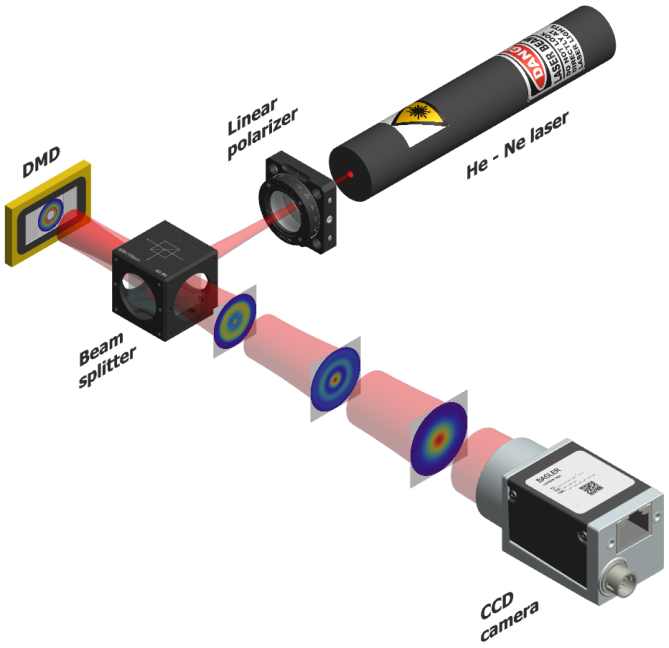

Figure 8.3: The experimental setup used to check the self-healing property of a naturally generated Gaussian beam using He-Ne laser. The obstruction was established by DMD, and the resulting complex amplitude was measured by a CCD camera and Shack-Hartmann wavefront sensor.

Firstly, we observed the self-reconstructed intensity profiles of a Gaussian beam of waist $w_0 = 0.24$ mm, divergence $\theta_0 = 0.84$ mrad, and Rayleigh range $z_R = 285$ mm. The beam was propagated to the distance $z = z_R$, where the beam width extended to the size $w_{z_R} = 0.34$ mm. In this plane, the DMD was inserted into a beam path to produce a centered obstruction of either circular or square shape of half-widths $a = 0.09$ mm. Then, the intensity scans were captured in several positions in the interval $0 - 2$ m by a CCD camera (Basler) with 5.5 μm pixel size. Some of these intensities for both square and circular obstructions are depicted in Figure 8.4.

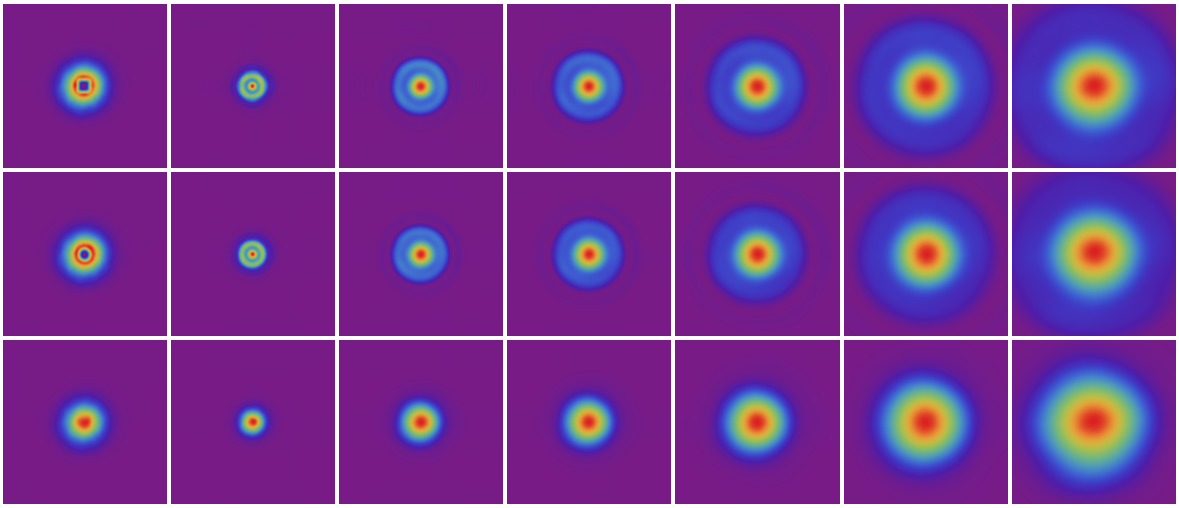

Figure 8.4: Intensity scans recorded by the CCD camera at increasing distances $\zeta = 0, 0.3, 0.5, 1, 3.5, 5, 6.5$. The beam has a waist $w_0 = 0.24$ mm, divergence $\theta_0 = 0.84$ mrad, and Rayleigh range $z_R = 285$ mm. The upper row corresponds to the squarely obstructed beam, middle row to circularly obstructed beam, both with $\alpha = 0.206$, whereas the lower row is the unobstructed beam. The first scans ($\zeta = 0$), reimagined to detection plane by the 1:1 achromatic doublet lens pair, are cropped and enlarged for better recognition of the patterns.

8.4 Results and discussion

To experimentally evaluate the degree of self-healing $D_{SH}(\zeta)$, we must be able to measure the whole complex amplitude for both the obstructed and the unobstructed fields, as is obvious from Eq. (8.15). To improve the measurement, a calibrated beam expander was used, which changed beam parameters into values $w_0 = 0.6$ mm and $z_R = 1787$ mm. This new beam was measured by the same CCD camera and a Shack-Hartmann wavefront sensor, consisting of a microlens array with 150 μm pitch. Both sensors were individually placed in the same detection planes from DMD and measure the intensity and wavefront profiles of an unobstructed beam. To increase wavefront measurement resolution, another beam expander coupled directly to the wavefront sensor was used.

The field complex amplitudes were then reconstructed from these measurements that were interpolated to the same resolution. To measure an obstructed beam, the DMD at distance of 560 mm from the waist with half-width $w_z = 0.635$ was placed. For this measurement, we used the circular obstruction with $\alpha = 0.14$, and detection planes in the range $\zeta \in 0.05 - 0.61$. Some of the resulting amplitudes are shown in Figure 8.5, where the real and imaginary parts are plotted.

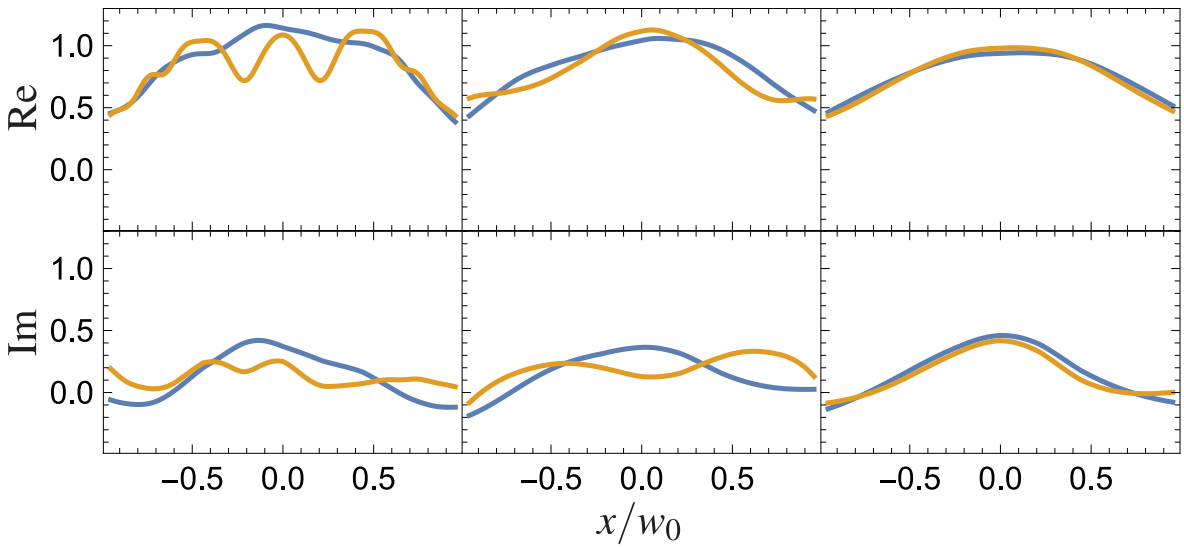

Figure 8.5: Real and imaginary parts of the energy-normalized field amplitudes at the positions $\zeta = 0.05, 0.28$, and 0.56 (from left to right). The obstructed field is represented in orange, while the unobstructed is in blue. The obstruction is characterized by $\alpha = 0.14$.

Once the complex amplitudes were experimentally determined, we could evaluate the degree of self-healing. For this purpose, we took the integration region as a disk of radius $b = a = 0.09$ mm, which corresponded to the full size of the obstacle. The experimental results are presented in Figure 8.6. For each detection plane, the measurements had been repeated over 100 times, with statistics characterized by error bars.

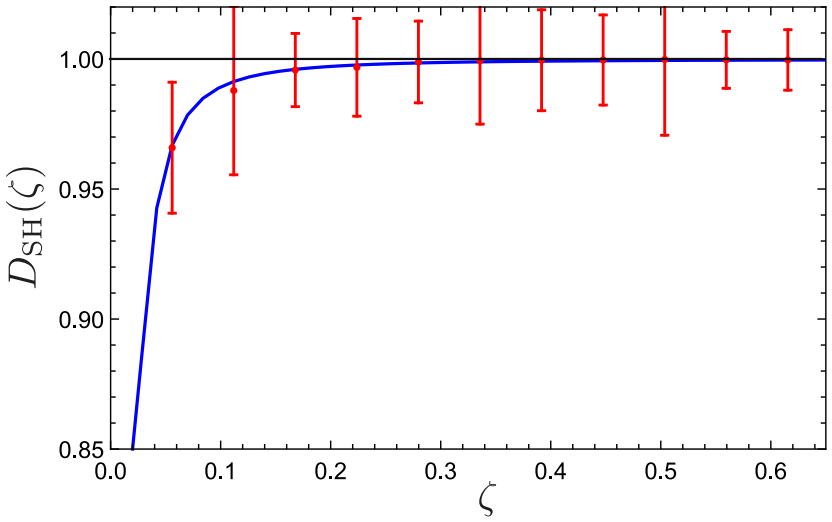

Figure 8.6: Experimentally determined degree of self-healing $D_{SH}(\zeta)$ obtained from measurements shown in Figure 8.5. The integration region is a disk of radius $b = a = 0.09$ mm. The error bars represent standard deviations.

In conclusion, we presented a general theory of the so-called self-healing property appearing when optical beams start to be partially obstructed. We showed that this capability is not only restricted to diffractionless beams as, e.g., Bessel beams, but can be applied theoretically to any optical beam. From a careful analysis of the involved physical mechanisms, we formulated the minimum propagation distance from the obstacle after which an optical beam recovers its initial intensity profile. Moreover, we quantified the degree of self-healing as a measure of closeness between obstructed and unobstructed beams. This metric proposes a suitable measure that was experimentally tested on Gaussian beams.

In the first part, we measured intensity self-healing using squarely and circularly obstructed beams, which confirmed a good agreement with the theoretical prediction. In the second part, we measured and verified the degree of self-healing, for which the whole complex amplitude was needed, which was measured by a standard CCD camera and Shack-Hartmann wavefront sensor. The results again confirm the proposed theory.

Chapter 9

Conclusions

This Thesis, based on five original publications [1–5], summarizes my previous experimental research realized during my Ph.D. studies. The introduced Chapters mainly deal with the optical two-point resolution phenomena and self-healing property of optical fields. The discussed issues are aimed at optimizing the external degrees of freedom of optical systems by novel methods within the wide subject of optical metrology. Both experimental and theoretical results are presented with the application of quantum protocols surpassing the traditional two-point resolution criteria, i.e., utilization of new superresolution methods and innovative analysis with characterization of self-healing mechanism of Gaussian beams.

At the beginning of the dissertation, the main goals are outlined together with a brief survey of current state of research. Nonetheless, it is appropriate to note, that the results themselves contribute to relatively new scientific topics and may serve as pivotal stepping stones for future more specialized applications.

In *Chapter 4*, one of the first experimental realization of new superresolution method called spatial-mode demultiplexing was demonstrated. Aside from the well-known classical resolution criteria, designating the minimal resolvable distance between two incoherent point sources, this method revisited this problem from the perspective of statistical estimation theory, Fisher information theory and their quantum analogies. Strikingly, when quantum protocols were applied, the quantum Fisher information for separation parameter maintained constant value for any separation. This is in contrast to an ordinary detection schemes, where the classical Fisher information quadratically falls to zero as the separation diminishes, effect known as *Rayleigh's course*. The core of developed experimental technique is based on input signal decomposition into Hermite-Gaussian basis. Here, the examined scenario of estimation of one parameter facilitated the decomposition only into the first two HG modes. This was mainly due to the concentration of Fisher's information in the HG_1 mode, which attained the ultimate quantum bound for small separation.

The decomposition itself was realized by the holographic projection by an amplitude-only spatial light modulator. As the result, we were able to estimate the smallest separation of two incoherent Gaussian point sources about 10% of Rayleigh's limit with error more than $20\times$ below the error for standard intensity detection schemes. This innovative measuring protocol has a far-reaching potential to be widely used in optical applications, especially astronomy, microscopy and spectroscopy.

Subsequently, *Chapter 5* was dedicated to the progressive research focused on two point resolution from the viewpoint of direct intensity detection. For this most widely used detection technique, novel optimal measurement scheme was introduced, using simple phase non-absorbing signum filter. This approach allows to transform any well-behaved symmetric point spread function into the particular form with zero intensity information-rich region, which makes Fisher information drop-off linear instead of quadratic for small separations. The realized experiment successfully demonstrated the application of such signum phase mask using phase-only spatial light modulator, and validated the linear scaling of Fisher information. Once again, we were able to estimate the distances deep in sub-Rayleigh region with the estimation variance improvement up to $10\times$ compared to direct imaging. Nevertheless, the experimental imperfections, such as systematic errors and setup instability, prevented from full attainment of theoretical limits. These conclusions also reflected, that the advantage of quantum schemes might be smaller than previously thought.

Chapter 6 referred to advanced exploitation of isolated zero information-rich regions, research primarily oriented towards superresolution in spectroscopy applications. We experimentally demonstrated the connection of linear decline of Fisher information for Sinc PSF, containing large number of natural zero regions, using two simple experiments. In these experiments, the spacing of natural longitudinal modes of a He-Ne laser cavity and separation of artificially generated spectral doublets were successfully measured well below the standard resolution limit.

Chapter 7 was intended on surpassing classical criteria of the longitudinal (axial) localization of one Gaussian point source using direct intensity detection. It was shown both theoretically and experimentally, that if the measuring camera was placed in one of two optimal transverse detection planes, it was possible to reach a quantum limit only by single intensity scan. The experimental verification was performed by simple microscopic setup with fiber-end as Gaussian point source, with the distance estimation ranging within tens of nanometers.

Finally in *Chapter 8*, the self-reconstruction mechanism of Gaussian beams was studied. For overall description of this property, the wave optics formalism with Babinet principle was used. There has been also introduced a suitable novel metric, that quantifies similarity between obstructed and unobstructed beams and new definition of minimal reconstruction

distance for beams that propagates behind the obstacle. These were acknowledged by experimental realization, in which the total complex amplitude of obscured and unobscured Gaussian beam was measured by the CCD camera and the Shack-Hartmann wavefront sensor.

Stručné shrnutí v češtině

Tato dizertační práce shrnuje můj dosavadní experimentální výzkum, který byl realizován v průběhu mého doktorského studia. Představené hlavní výsledky základního výzkumu, vycházející z pěti původních vědeckých publikací [1–5], jsou primárně orientovány do oblasti dvou-bodového optického rozlišení a mechanismu samorekonstrukce optických polí. Diskutovaná problematika si rovněž klade za cíl optimalizaci vnějších stupňů volnosti světla optických systémů a to s rozsáhlejším uplatněním v optické metrologii. Představené teoretické, ale i experimentální výsledky využívají kvantových protokolů překonávající tradiční dvou-bodové rozlišovací kritéria, t.j. použití moderních metod superrozlišení a inovativní analýzu a kvantifikaci mechanismu samoobnovení s aplikací na Gaussovské svazky.

Na začátku předložené disertační práce jsou nastíněny její hlavní cíle společně se stručným přehledem aktuálního výzkumu. Nicméně je třeba poznamenat, že dosažené výsledky samy o sobě tvoří relativně nová vědecká témata a zůstávají základními odrazovými můstky pro budoucí specializovanější aplikace.

V kapitole 4 byla demonstrována jedna z prvních experimentálních realizací nové metody superrozlišení, nazývané rozklad do sady prostorových modů (SPADE, z angl. Spatial-mode demultiplexing). Tato metoda vedle známých klasických rozlišovacích kritériích, určujících minimální rozlišitelnou vzdálenost mezi dvěma nekoherentními bodovými zdroji, pohlíží na tento problém z hlediska teorie statistického odhadu, Fisherovy informační teorie a jejich kvantových analogií. Překvapivě bylo zjištěno, že při aplikaci kvantových protokolů nabývá hodnota kvantové Fisherovy informace pro parametr separace téměř konstantních hodnot, a to pro jakoukoliv zdálenost mezi bodovými zdroji. To je ve značném protikladu s běžně používanými detečním schématy, kde hodnota klasické Fisherovy informace kvadraticky klesá k nule, jestliže se vzdálenost bodových zdrojů blíží k nule, efekt známý jako *Rayleighova kletba*. Jádro této moderní experimentální techniky je založeno na dekompozici vstupního signálu do báze Hermit-Gaussovských módů. Zde zkoumaný scénář, estimace pouze parametru separace, usnadňuje dekompozici pouze do prvních dvou HG módů. Toto bylo možné díky vysoké koncentraci Fisherovy informace v módu HG_1, který dosahoval pro malé separace mezního kvantového limitu. Samotná dekompozice byla poté realizována pomocí holografické projekce skrze amplitudový prostorový modulátor světla. Výsledkem

byla schopnost estimovat nejmenší separaci dvou nekoherentních bodových zdrojů dosahující 10% Rayleighova limitu a s variancí $20\times$ nižší než by bylo možné dosáhnout při použití klasické intenzitní detekce. Tato měřící technika celkově vykazuje slibný aplikační potenciál a to převážně v oblastech jako je astronomie, mikroskopie nebo spektroskopie.

Následující kapitola 5 byla věnována navazujícímu výzkumu zaměřeného na dvou-bodové rozlišení z pohledu přímé intenzitní detekce. Pro tento nejrozšířenější postup detekce bylo vyvinuto nové optimální měřící schéma využívající jednoduchého fázového neabsorbujícího signum filtru. Tato technika umožňuje transformovat téměř jakoukoliv "dobře se chovající" symetrickou bodovou rozptylovou funkci do speciální formy, obsahující informačně bohatou oblast nulové intenzity, způsobující pro malé separace bodových zdrojů lineární pokles Fisherovy informace namísto kvadratického. Provedený experiment úspěšně demonstroval použití takové fázové signum masky za pomoci fázového modulátoru světla a potvrdil lineární škálování Fisherovy informace. Opětovně byl estimován parametr vzdálenosti dvou bodových zdrojů hluboko v sub-Rayleighově oblasti a to až s $10\times$ lepším rozptylem odhadu ve srovnání s přímou intenzitní detekcí. Navzdory dobrým výsledkům však nedokonalosti experimentu, jako systematické chyby a nestabilita měření, zabránily úplnému dosažení ultimátního limitu. Nicméně celkové závěry rovněž odrážely fakt, že celková výhoda kvantových protokolů může být menší něž se původně očekávalo.

Kapitola 6 se týkala pokročilého využití výše zmíněných informačně bohatých oblastí nulové intenzity, primárně orientovaného na superrozlišení ve spektroskopických aplikacích. Experimentálně bylo ukázáno spojení lineárního poklesu Fisherovy informace pro bodovou rozptylovou funkci popsanou funkcí Sinc, přirozeně obsahující velké množství oblastí nulové intenzity, pomocí dvou experimentů. V těchto experimentech byl úspěšně změřen jednak rozestup přirozených podélných módů kavity He-Ne laseru a jednak vzdálenost uměle vytvořených spektrálních dubletů hluboce pod standardním rozlišovacím limitem.

Předposlední kapitola 7 byla zaměřena na překonání klasického limitu v oblasti podélné (axiální) lokalizace jednoho Gaussovského bodového zdroje opět za pomoci klasické intenzitní detekce. Teoreticky i experimentálně bylo ukázáno, že pokud je kamera umístěna v jedné ze dvou optimálních detekčních rovin, je možné dosáhnout kvantového limitu pouze jediným intenzitním snímkem. Experimentální ověření bylo provedeno s využitím mikroskopické sestavy, kde byl Gaussovský bodový zdroj generován koncem optického vlákna, přičemž minimální odhad axiální vzdálenosti dosahoval hodnot v řádu desítek nanometrů.

V poslední kapitole 8 byl studován mechanismus samorekonstrukce u Gaussovských svazků. Pro celkový popis byl použit formalismus vlnové optiky s Babinetovým principem. Byla také zavedena vhodná metrika, která kvantifikuje podobnost mezi omezeným a neomezeným svazkem a nová definice minimální rekonstrukční vzdálenosti pro Gaussovské svazky šířící se za překážkou. Všechny předpoklady a definice byly experimentálně potvr-

zeny a to měřením celkové komplexní amplitudy omezeného a neomezeného Gaussovského svazku pomocí CCD kamery a Shack-Hatmannova senzoru vlnoplochy.

Publications of the author and a list of citations

The Thesis is based on the following publications:

- M. Paúr, B. Stoklasa, Z. Hradil, L. L. Sánchez-Soto and J. Řeháček. '*Achieving the ultimate optical resolution*'. In: *Optica* **3.10** (2016), pp. 1144–1147
- M. Paúr, B. Stoklasa, J. Grover, A. Krzic, L. L. Sánchez-Soto, Z. Hradil and J. Řeháček. '*Tempering Rayleigh's curse with PSF shaping*'. In: *Optica* **5.10** (2018), pp. 1177–1180
- M. Paúr, B. Stoklasa, D. Koutný, J. Řeháček, Z. Hradil et al. '*Reading out Fisher information from the zeros of the point spread function*'. In: *Optics Letters* **44.12** (2019), pp. 3114–3117
- J. Řeháček, M. Paúr, B. Stoklasa, D. Koutný, Z. Hradil and L. L. Sánchez-Soto. '*Intensity-Based Axial Localization at the Quantum Limit*'. In: *Physical Review Letters* **123.19** (2019), p. 193601
- A. Aiello, G. S. Agarwal, M. Paúr, B. Stoklasa, Z. Hradil et al. '*Unraveling beam self-healing*'. In: *Optics Express* **25.16** (2017), pp. 19147–19157

Other co-author publications:

- J. Řeháček, M. Paúr, B. Stoklasa, Z. Hradil and L. L. Sánchez-Soto. '*Optimal measurements for resolution beyond the Rayleigh limit*'. In: *Optics Letters* **42.2** (2017), pp. 231–234
- L. Moťka, M. Paúr, J. Řeháček, Z. Hradil and L. L. Sánchez-Soto. '*Efficient tomography with unknown detectors*'. In: *Quantum Science and Technology* **2.3** (2017), p. 035003

- J. Řeháček, Z. Hradil, B. Stoklasa, M. Paúr, J. Grover, A. Krzic and L. L. Sánchez-Soto. '*Multiparameter quantum metrology of incoherent point sources: Towards realistic superresolution*'. In: *Physical Review A* **96.6** (2017), p. 062107

- J. M. Donohue, V. Ansari, J. Řeháček, Z. Hradil, B. Stoklasa et al. '*Quantum-Limited Time-Frequency Estimation through Mode-Selective Photon Measurement*'. In: *Physical Review Letters* **121.9** (2018), p. 090501

List of citations (without self-citations):

- M. Paúr, B. Stoklasa, Z. Hradil, L. L. Sánchez-Soto and J. Řeháček. '*Achieving the ultimate optical resolution*'. In: *Optica* **3.10** (2016), pp. 1144–1147

  1. R. Nair and M. Tsang. '*Far-Field Superresolution of Thermal Electromagnetic Sources at the Quantum Limit*'. In: *Physical Review Letters* **117.19** (2016), p. 190801
  2. C. Lupo and S. Pirandola. '*Ultimate Precision Bound of Quantum and Subwavelength Imaging*'. In: *Physical Review Letters* **117.19** (2016), p. 190802
  3. W.-K. Tham, H. Ferretti and A. M. Steinberg. '*Beating Rayleigh's Curse by Imaging Using Phase Information*'. In: *Physical Review Letters* **118.7** (2017), p. 070801
  4. M. Tsang. '*Subdiffraction incoherent optical imaging via spatial-mode demultiplexing*'. In: *New Journal of Physics* **19.2** (2017), p. 023054
  5. K. A. Forbes, J. S. Ford and D. L. Andrews. '*Nonlocalized Generation of Correlated Photon Pairs in Degenerate Down-Conversion*'. In: *Physical Review Letters* **118.13** (2017), p. 133602
  6. S. Z. Ang, R. Nair and M. Tsang. '*Quantum limit for two-dimensional resolution of two incoherent optical point sources*'. In: *Physical Review A* **95.6** (2017), p. 063847
  7. A. Chrostowski, R. Demkowicz-Dobrzański, M. Jarzyna and K. Banaszek. '*On super-resolution imaging as a multiparameter estimation problem*'. In: *International Journal of Quantum Information* **15.08** (2017), p. 1740005
  8. F. Yang, R. Nair, M. Tsang, Ch. Simon and A. I. Lvovsky. '*Fisher information for far-field linear optical superresolution via homodyne or heterodyne detection in a higher-order local oscillator mode*'. In: *Physical Review A* **96.6** (2017), p. 063829
  9. Y. Zhou, M. Mirhosseini, D. Fu, J. Zhao, S. M. H. Rafsanjani, A. E. Willner and R. W. Boyd. '*Sorting Photons by Radial Quantum Number*'. In: *Physical Review Letters* **119.26** (2017), p. 263602

10. M. Tsang. '*Conservative classical and quantum resolution limits for incoherent imaging*'. In: *Journal of Modern Optics* **65.11** (2017), pp. 1385–1391

11. M. Tsang. '*Subdiffraction incoherent optical imaging via spatial-mode demultiplexing: Semiclassical treatment*'. In: *Physical Review A* **97.2** (2018), p. 023830

12. M. P. Backlund, Y. Shechtman and R. L. Walsworth. '*Fundamental Precision Bounds for Three-Dimensional Optical Localization Microscopy with Poisson Statistics*'. In: *Physical Review Letters* **121.2** (2018), p. 023904

13. M. Unternährer, B. Bessire, L. Gasparini, M. Perenzoni and A. Stefanov. '*Super-resolution quantum imaging at the Heisenberg limit*'. In: *Optica* **5.9** (2018), pp. 1150–1154

14. Z. Yu and S. Prasad. '*Quantum Limited Superresolution of an Incoherent Source Pair in Three Dimensions*'. In: *Physical Review Letters* **121.18** (2018), p. 180504

15. Y. Zhou, J. Zhao, Z. Shi, S. M. H. Rafsanjani, M. Mirhosseini et al. '*Hermite-Gaussian mode sorter*'. In: *Optics Letters* **43.21** (2018), p. 5263

16. W. Larson and B. E. A. Saleh. '*Resurgence of Rayleigh's curse in the presence of partial coherence*'. In: *Optica* **5.11** (2018), pp. 1382–1389

17. S. Pirandola, B. R. Bardhan, T. Gehring, C. Weedbrook and S. Lloyd. '*Advances in photonic quantum sensing*'. In: *Nature Photonics* **12.12** (2018), pp. 724–733

18. X.-M. Lu, H. Krovi, R. Nair, S. Guha and J. H. Shapiro. '*Quantum-optimal detection of one-versus-two incoherent optical sources with arbitrary separation*'. In: *npj Quantum Information* **4.1** (2018), p. 64

19. M. Parniak, S. Borówka, K. Boroszko, W. Wasilewski, K. Banaszek and R. Demkowicz-Dobrzański. '*Beating the Rayleigh Limit Using Two-Photon Interference*'. In: *Physical Review Letters* **121.25** (2018), p. 250503

20. I. M. Akhmedzhanov, D. V. Baranov, E. M. Zolotov and Yu I. Shupletsova. '*Superresolution effect on a microstep phase image in a laser heterodyne microscope*'. In: *Quantum Electronics* **49.7** (2019), pp. 698–706

21. S. Zhou and L. Jiang. '*Modern description of Rayleigh's criterion*'. In: *Physical Review A* **99.1** (2019), p. 013808

22. M. Tsang. '*Quantum limit to subdiffraction incoherent optical imaging*'. In: *Physical Review A* **99.1** (2019), p. 012305

23. S. Prasad and Z. Yu. '*Quantum-limited superlocalization and superresolution of a source pair in three dimensions*'. In: *Physical Review A* **99.2** (2019), p. 022116

24. I. R. Berchera and I. P. Degiovanni. '*Quantum imaging with sub-Poissonian light: challenges and perspectives in optical metrology*'. In: *Metrologia* **56**.**2** (2019), p. 024001
25. C. Napoli, S. Piano, R. Leach, G. Adesso and T. Tufarelli. '*Towards Superresolution Surface Metrology: Quantum Estimation of Angular and Axial Separations*'. In: *Physical Review Letters* **122**.**14** (2019), p. 140505
26. J. Yang, S. Pang, Y. Zhou and A. N. Jordan. '*Optimal measurements for quantum multiparameter estimation with general states*'. In: *Physical Review A* **100**.**3** (2019), p. 032104
27. K. A. G. Bonsma-Fisher, W.-K. Tham, H. Ferretti and A. M. Steinberg. '*Realistic sub-Rayleigh imaging with phase-sensitive measurements*'. In: *New Journal of Physics* **21**.**9** (2019), p. 093010
28. L. A. Howard, G. G. Gillett, M. E. Pearce, R. A. Abrahao, T. J. Weinhold, P. Kok and A. G. White. '*Optimal Imaging of Remote Bodies Using Quantum Detectors*'. In: *Physical Review Letters* **123**.**14** (2019), p. 143604
29. I. Peshko, D. Mogilevtsev, I. Karuseichyk, A. Mikhalychev, A. P. Nizovtsev, G. Ya. Slepyan and A. Boag. '*Quantum noise radar: superresolution with quantum antennas by accessing spatiotemporal correlations*'. In: *Optics Express* **27**.**20** (2019), pp. 29217–29231
30. E. Bisketzi, D. Branford and A. Datta. '*Quantum limits of localisation microscopy*'. In: *New Journal of Physics* **21**.**12** (2019), p. 123032
31. Y. L. Len, Ch. Datta, M. Parniak and K. Banaszek. '*Resolution limits of spatial mode demultiplexing with noisy detection*'. In: *International Journal of Quantum Information* **18**.**01** (2020), p. 1941015
32. C. Lupo. '*Subwavelength quantum imaging with noisy detectors*'. In: *Physical Review A* **101**.**2** (2020), p. 022323
33. C. Lupo, Z. Huang and P. Kok. '*Quantum Limits to Incoherent Imaging are Achieved by Linear Interferometry*'. In: *Physical Review Letters* **124**.**8** (2020), p. 080503
34. M. Tsang. '*Resolving starlight: a quantum perspective*'. In: *Contemporary Physics* **60**.**4** (2019), pp. 279–298
35. S. Prasad. '*Quantum limited super-resolution of an unequal-brightness source pair in three dimensions*'. In: *Physica Scripta* **95**.**5** (2020), p. 054004
36. F. Zhang, H. Wang, C. Wang, Y. Zhao and J. Duan. '*Direct femtosecond laser writing of inverted array for broadband antireflection in the far-infrared*'. In: *Optics and Lasers in Engineering* **129** (2020), p. 106062

37. M. Salit, J. Klein and L. Lust. '*Experimental characterization of a mode-separating photonic lantern for imaging applications*'. In: *Applied Optics* **59**. **17** (2020), pp. 5319–5324
38. W. Larson and B. E. A. Saleh. '*Quantum-enhanced estimation of the optical phase gradient by use of image-inversion interferometry*'. In: *Physical Review A* **102.1** (2020), p. 013712
39. I. A. Peshko. '*Avoiding the "Rayleigh Catastrophe" Using Asymmetric Antennas*'. In: *Journal of Applied Spectroscopy* **87.3** (2020), pp. 447–451
40. M. R. Grace, Z. Dutton, A. Ashok and S. Guha. '*Approaching quantum-limited imaging resolution without prior knowledge of the object location*'. In: *Journal of the Optical Society of America A* **37.8** (2020), pp. 1288–1299
41. M. Gessner, C. Fabre and N. Treps. '*Superresolution Limits from Measurement Crosstalk*'. In: *Physical Review Letters* **125.10** (2020), p. 100501
42. A. Pan, Ch. Zuo and B. Yao. '*High-resolution and large field-of-view Fourier ptychographic microscopy and its applications in biomedicine*'. In: *Reports on Progress in Physics* **83.9** (2020), p. 096101

■ M. Paúr, B. Stoklasa, J. Grover, A. Krzic, L. L. Sánchez-Soto, Z. Hradil and J. Řeháček. '*Tempering Rayleigh's curse with PSF shaping*'. In: *Optica* **5.10** (2018), pp. 1177–1180

1. M. Tsang. '*Quantum limit to subdiffraction incoherent optical imaging*'. In: *Physical Review A* **99.1** (2019), p. 012305
2. E. Bisketzi, D. Branford and A. Datta. '*Quantum limits of localisation microscopy*'. In: *New Journal of Physics* **21.12** (2019), p. 123032
3. C. Lupo. '*Subwavelength quantum imaging with noisy detectors*'. In: *Physical Review A* **101.2** (2020), p. 022323
4. C. Lupo, Z. Huang and P. Kok. '*Quantum Limits to Incoherent Imaging are Achieved by Linear Interferometry*'. In: *Physical Review Letters* **124.8** (2020), p. 080503
5. M. Tsang. '*Resolving starlight: a quantum perspective*'. In: *Contemporary Physics* **60.4** (2019), pp. 279–298
6. F. Albarelli, M. Barbieri, M. G. Genoni and I. Gianani. '*A perspective on multiparameter quantum metrology: From theoretical tools to applications in quantum imaging*'. In: *Physics Letters A* **384.12** (2020), p. 126311
7. M. R. Grace, Z. Dutton, A. Ashok and S. Guha. '*Approaching quantum-limited imaging resolution without prior knowledge of the object location*'. In: *Journal of the Optical Society of America A* **37.8** (2020), pp. 1288–1299

- M. Paúr, B. Stoklasa, D. Koutný, J. Řeháček, Z. Hradil et al. '*Reading out Fisher information from the zeros of the point spread function*'. In: *Optics Letters* **44.12** (2019), pp. 3114–3117

    1. M. Tsang. '*Resolving starlight: a quantum perspective*'. In: *Contemporary Physics* **60.4** (2019), pp. 279–298
    2. M. Salit, J. Klein and L. Lust. '*Experimental characterization of a mode-separating photonic lantern for imaging applications*'. In: *Applied Optics* **59**. **17** (2020), pp. 5319–5324
    3. M. R. Grace, Z. Dutton, A. Ashok and S. Guha. '*Approaching quantum-limited imaging resolution without prior knowledge of the object location*'. In: *Journal of the Optical Society of America A* **37.8** (2020), pp. 1288–1299

- J. Řeháček, M. Paúr, B. Stoklasa, D. Koutný, Z. Hradil and L. L. Sánchez-Soto. '*Intensity-Based Axial Localization at the Quantum Limit*'. In: *Physical Review Letters* **123.19** (2019), p. 193601

    1. M. Tsang. '*Resolving starlight: a quantum perspective*'. In: *Contemporary Physics* **60.4** (2019), pp. 279–298

- A. Aiello, G. S. Agarwal, M. Paúr, B. Stoklasa, Z. Hradil et al. '*Unraveling beam self-healing*'. In: *Optics Express* **25.16** (2017), pp. 19147–19157

    1. V. Arrizon, G. Mellado-Villase ñor, D. Aguirre-Olivas and H. M. Moya-Cessa. '*Mathematical and diffractive modeling of self-healing*'. In: *Optics Express* **26.9** (2018), pp. 12219–12229
    2. N. Mphuthi, R. Botha and A. Forbes. '*Are Bessel beams resilient to aberrations and turbulence?*' In: *Journal of the Optical Society of America A* **35.6** (2018), pp. 1021–1027
    3. E. Otte, I. Nape, C. Rosales-Guzmán, A. Vallés, C. Denz and A. Forbes. '*Recovery of nonseparability in self-healing vector Bessel beams*'. In: *Physical Review A* **98.5** (2018), p. 053818
    4. A. V. Volyar, M. V. Bretsko, Y. E. Akimova, Y. A. Egorov and V. V. Milyukov. '*Sectorial perturbation of vortex beams: Shannon entropy, orbital angular momentum and topological charge*'. In: *Computer Optics* **43.5** (2019), pp. 723–734
    5. Ch. Vetter, R. Steinkopf, K. Bergner, M. Ornigotti, S. Nolte, H. Gross and A. Szameit. '*Realization of Free-Space Long-Distance Self-Healing Bessel Beams*'. In: *Laser & Photonics Reviews* **13.10** (2019), p. 1900103

6. J. Mendoza-Hernández, M. L. Arroyo-Carrasco, M. D. Iturbe-Castillo and S. Chávez-Cerda. '*Structured light beams constituted of incoming and outgoing waves*'. In: *Physical Review A* **100.5** (2019), p. 053847

7. A. Volyar, M. Bretsko, Y. Akimova and Y. Egorov. '*Orbital angular momentum and informational entropy in perturbed vortex beams*'. In: *Optics Letters* **44.23** (2019), pp. 5687–5690

8. Z. Xu, X. Liu, Y. Chen, F. Wang, L. Liu et al. '*Self-healing properties of Hermite-Gaussian correlated Schell-model beams*'. In: *Optics Express* **28.3** (2020), pp. 2828–2837

9. S. Gorelick, D. M. Paganin, D. Korneev and A. de Marco. '*Hybrid refractive-diffractive axicons for Bessel-beam multiplexing and resolution improvement*'. In: *Optics Express* **28.8** (2020), pp. 12174–1218

10. S. Ryu, B. Seong, Ch. Lee, M. Y. Ahn, W. T. Kim, K.-M. Choe and Ch. Joo. '*Light sheet fluorescence microscopy using axi-symmetric binary phase filters*'. In: *Biomedical Optics Express* **11.7** (2020), pp. 3936–3951

11. G. Lasry, T. Melamed and Y. Brick. '*Manipulation and control of 3-D caustic beams over an arbitrary trajectory*'. In: *Optics Express* **28.14** (2020), pp. 20645–20659

Bibliography

[1] M. Paúr, B. Stoklasa, Z. Hradil, L. L. Sánchez-Soto and J. Řeháček. '*Achieving the ultimate optical resolution*'. In: *Optica* **3**.**10** (2016), pp. 1144–1147.

[2] M. Paúr, B. Stoklasa, J. Grover, A. Krzic, L. L. Sánchez-Soto, Z. Hradil and J. Řeháček. '*Tempering Rayleigh's curse with PSF shaping*'. In: *Optica* **5**.**10** (2018), pp. 1177–1180.

[3] M. Paúr, B. Stoklasa, D. Koutný, J. Řeháček, Z. Hradil et al. '*Reading out Fisher information from the zeros of the point spread function*'. In: *Optics Letters* **44**.**12** (2019), pp. 3114–3117.

[4] J. Řeháček, M. Paúr, B. Stoklasa, D. Koutný, Z. Hradil and L. L. Sánchez-Soto. '*Intensity-Based Axial Localization at the Quantum Limit*'. In: *Physical Review Letters* **123**.**19** (2019), p. 193601.

[5] A. Aiello, G. S. Agarwal, M. Paúr, B. Stoklasa, Z. Hradil et al. '*Unraveling beam self-healing*'. In: *Optics Express* **25**.**16** (2017), pp. 19147–19157.

[6] M. Tsang, R. Nair and X.-M. Lu. '*Quantum Theory of Superresolution for Two Incoherent Optical Point Sources*'. In: *Physical Review X* **6**.**3** (2016), p. 031033.

[7] E. R. Pike and G. de Villers. *The Limits of Resolution*. Taylor & Francis Inc, 2016. 546 pp.

[8] E. Hecht. *Optics*. 5th ed. Pearson, 2016. 728 pp.

[9] R. Irwan and R. G. Lane. '*Analysis of optimal centroid estimation applied to Shack-Hartmann sensing*'. In: *Applied Optics* **38**.**32** (1999), pp. 6737–6743.

[10] S. Thomas, T. Fusco, A. Tokovinin, M. Nicolle, V. Michau and G. Rousset. '*Comparison of centroid computation algorithms in a Shack-Hartmann sensor*'. In: *Monthly Notices of the Royal Astronomical Society* **371**.**1** (2006), pp. 323–336.

[11] C.-S. Liu and P. D. Lin. '*Computational method for deriving the geometric point spread function of an optical system*'. In: *Applied Optics* **49**.**1** (2009), pp. 126–136.

[12] A. J. den Dekker and A. van den Bos. '*Resolution: a survey*'. In: *Journal of the Optical Society of America A* **14**.**3** (1997), pp. 547–557.

[13] B. P. Ramsay, E. L. Cleveland and O. T. Koppius. '*Criteria and the Intensity-Epoch Slope*'. In: *Journal of the Optical Society of America* **31.1** (1941), p. 26.

[14] J. W. S. Rayleigh. '*XXXI. Investigations in optics, with special reference to the spectroscope*'. In: *The London, Edinburgh, and Dublin Philosophical Magazine and Journal of Science* **8.49** (1879), pp. 261–274.

[15] J. W. S. Rayleigh. '*XII. On the manufacture and theory of diffraction-gratings*'. In: *The London, Edinburgh, and Dublin Philosophical Magazine and Journal of Science* **47.310** (1874), pp. 81–93.

[16] J. G. Robertson. '*Quantifying Resolving Power in Astronomical Spectra*'. In: *Publications of the Astronomical Society of Australia* **30.E048** (2013).

[17] C. M. Sparrow. '*On Spectroscopic Resolving Power*'. In: *The Astrophysical Journal* **44** (1916), p. 76.

[18] R. Barakat and E. Levin. '*Application of Apodization to Increase Two-Point Resolution by the Sparrow Criterion II Incoherent Illumination*'. In: *Journal of the Optical Society of America* **53.2** (1963), pp. 274–282.

[19] A. Schuster. *An Introduction to the Theory of Optics*. 2nd ed. HardPress Publishing, 2013. 390 pp.

[20] W. V. Houston. '*A Compound Interferometer for Fine Structure Work*'. In: *Physical Review* **29.3** (1927), pp. 478–484.

[21] A. Buxton and M. A. Oxon. '*XLI. Note on optical resolution*'. In: *The London, Edinburgh, and Dublin Philosophical Magazine and Journal of Science* **23.154** (1937), pp. 440–442.

[22] W. R. Dawes. '*Catalogue of Micrometrical Measurements of Double Stars*'. In: *Monthly Notices of the Royal Astronomical Society* **27.6** (1867), pp. 217–238.

[23] G. W. Burr, H. Coufal, R. K. Grygier, J. A. Hoffnagle and C. M. Jefferson. '*Noise reduction of page-oriented data storage by inverse filtering during recording*'. In: *Optics Letters* **23.4** (1998), pp. 289–291.

[24] T. Daboczi and T. B. Bako. '*Inverse filtering of optical images*'. In: *IEEE Transactions on Instrumentation and Measurement* **50.4** (2001), pp. 991–994.

[25] B. Salahieh, J. J. Rodriguez and R. Liang. '*Direct superresolution for realistic image reconstruction*'. In: *Optics Express* **23.20** (2015), pp. 26124–26138.

[26] I. J. Cox and C. J. R. Sheppard. '*Information capacity and resolution in an optical system*'. In: *Journal of the Optical Society of America A* **3.8** (1986), pp. 1152–1158.

[27] T. Gureyev, Y. Nesterets and F. de Hoog. '*Spatial resolution, signal-to-noise and information capacity of linear imaging systems*'. In: *Optics Express* **24.15** (2016), pp. 17168–17182.

[28] E. Bettens, D. Van Dyck, A. J. den Dekker, J. Sijbers and A. van den Bos. '*Model-based two-object resolution from observations having counting statistics*'. In: *Ultramicroscopy* **77.1-2** (1999), pp. 37–48.

[29] M. J. Rust, M. Bates and X. Zhuang. '*Sub-diffraction-limit imaging by stochastic optical reconstruction microscopy (STORM)*'. In: *Nature Methods* **3.10** (2006), pp. 793–796.

[30] H. L. Van Trees, K. L. Bell and Z. Tian. *Detection Estimation and Modulation Theory, Part I*. 2nd ed. John Wiley & Sons Inc, 2013. 1176 pp.

[31] A. Fischer. '*Fisher information and Cramér-Rao bound for unknown systematic errors*'. In: *Measurement* **113** (2018), pp. 131–136.

[32] J. Řeháček and Z. Hradil. '*Uncertainty relations from fisher information*'. In: *Journal of Modern Optics* **51.6-7** (2004), pp. 979–982.

[33] C. W. Helstrom. *Quantum detection and estimation theory*. 1st ed. Vol. 123. Academic Press, 1976. 308 pp.

[34] V. Giovannetti, S. Lloyd and L. Maccone. '*Advances in quantum metrology*'. In: *Nature Photonics* **5.4** (2011), pp. 222–229.

[35] V. Giovannetti. '*Quantum-Enhanced Measurements: Beating the Standard Quantum Limit*'. In: *Science* **306.5700** (2004), pp. 1330–1336.

[36] M. Hayashi. *Asymptotic Theory of Quantum Statistical Inference*. World Scientific, 2005, p. 560.

[37] A. Fujiwara. '*Strong consistency and asymptotic efficiency for adaptive quantum estimation problems*'. In: *Journal of Physics A: Mathematical and General* **39.40** (2006), pp. 12489–12504.

[38] M. Tsang. '*Subdiffraction incoherent optical imaging via spatial-mode demultiplexing*'. In: *New Journal of Physics* **19.2** (2017), p. 023054.

[39] M. Tsang. '*Quantum limit to subdiffraction incoherent optical imaging*'. In: *Physical Review A* **99.1** (2019), p. 012305.

[40] R. Nair and M. Tsang. '*Interferometric superlocalization of two incoherent optical point sources*'. In: *Optics Express* **24.4** (2016), pp. 3684–3701.

[41] S. Z. Ang, R. Nair and M. Tsang. '*Quantum limit for two-dimensional resolution of two incoherent optical point sources*'. In: *Physical Review A* **95.6** (2017), p. 063847.

[42] H. Krovi, S. Guha and J. H. Shapiro. '*Attaining the quantum limit of passive imaging*'. In: (2016). arXiv: 1609.00684v1 (quant-ph).

[43] R. Nair and M. Tsang. '*Far-Field Superresolution of Thermal Electromagnetic Sources at the Quantum Limit*'. In: *Physical Review Letters* **117.19** (2016), p. 190801.

[44] C. Lupo and S. Pirandola. '*Ultimate Precision Bound of Quantum and Subwavelength Imaging*'. In: *Physical Review Letters* **117.19** (2016), p. 190802.

[45] J. Řeháček, M. Paúr, B. Stoklasa, Z. Hradil and L. L. Sánchez-Soto. '*Optimal measurements for resolution beyond the Rayleigh limit*'. In: *Optics Letters* **42.2** (2017), pp. 231–234.

[46] W.-K. Tham, H. Ferretti and A. M. Steinberg. '*Beating Rayleigh's Curse by Imaging Using Phase Information*'. In: *Physical Review Letters* **118.7** (2017), p. 070801.

[47] Z. S. Tang, K. Durak and A. Ling. '*Fault-tolerant and finite-error localization for point emitters within the diffraction limit*'. In: *Optics Express* **24.19** (2016), pp. 22004–22012.

[48] F. Yang, A. Tashchilina, E. S. Moiseev, Ch. Simon and A. I. Lvovsky. '*Far-field linear optical superresolution via heterodyne detection in a higher-order local oscillator mode*'. In: *Optica* **3.10** (2016), pp. 1148–1152.

[49] V. Torres-Company, J. Lancis and P. Andrés. '*Space-Time Analogies in Optics*'. In: *Progress in Optics*. Vol. 56. Elsevier, 2011. Chap. 1, pp. 1–80.

[50] R. Salem, M. A. Foster and A. L. Gaeta. '*Application of space-time duality to ultrahigh-speed optical signal processing*'. In: *Advances in Optics and Photonics* **5.3** (2013), pp. 274–317.

[51] J. M. Donohue, V. Ansari, J. Řeháček, Z. Hradil, B. Stoklasa et al. '*Quantum-Limited Time-Frequency Estimation through Mode-Selective Photon Measurement*'. In: *Physical Review Letters* **121.9** (2018), p. 090501.

[52] A. S. Holevo. *Probabilistic and Statistical Aspects of Quantum Theory*. 1st ed. Scuola Normale Superiore, 2011. 340 pp.

[53] M. Tsang. '*The Holevo Cramér-Rao bound is at most thrice the Helstrom version*'. In: (2019). arXiv: 1911.08359v1 (quant-ph).

[54] K Matsumoto. '*A new approach to the Cramér-Rao-type bound of the pure-state model*'. In: *Journal of Physics A: Mathematical and General* **35.13** (2002), pp. 3111–3123.

[55] F. Albarelli, M. Tsang and A. Datta. '*Upper bounds on the Holevo Cramér-Rao bound for multiparameter quantum parametric and semiparametric estimation*'. In: (2019). arXiv: 1911.11036v2 (quant-ph).

[56] K. Yamagata, A. Fujiwara and R. D. Gill. '*Quantum local asymptotic normality based on a new quantum likelihood ratio*'. In: *The Annals of Statistics* **41.4** (2013), pp. 2197–2217.

[57] E. Abbe. '*Ueber einen neuen Beleuchtungsapparat am Mikroskop*'. In: *Archiv für Mikroskopische Anatomie* **9.1** (1873), pp. 469–480.

[58] G. Huszka and M. A. M. Gijs. '*Super-resolution optical imaging: A comparison*'. In: *Micro and Nano Engineering* **2** (2019), pp. 7–28.

[59] L. V. Peedikakkal, A. Furley and A. J. Cadby. '*A Multimodal Adaptive Super-Resolution and Confocal Microscope*'. In: *Biorxiv* (2018).

[60] B. Huang, M. Bates and X. Zhuang. '*Super-Resolution Fluorescence Microscopy*'. In: *Annual Review of Biochemistry* **78.1** (2009), pp. 993–1016.

[61] L. Schermelleh, R. Heintzmann and H. Leonhardt. '*A guide to super-resolution fluorescence microscopy*'. In: *The Journal of Cell Biology* **190.2** (2010), pp. 165–175.

[62] B. O. Leung and K. C. Chou. '*Review of Super-Resolution Fluorescence Microscopy for Biology*'. In: *Applied Spectroscopy* **65.9** (2011), pp. 967–980.

[63] S. W. Hell and J. Wichmann. '*Breaking the diffraction resolution limit by stimulated emission: stimulated-emission-depletion fluorescence microscopy*'. In: *Optics Letters* **19.11** (1994), pp. 780–782.

[64] T. A. Klar and S. W. Hell. '*Subdiffraction resolution in far-field fluorescence microscopy*'. In: *Optics Letters* **24.14** (1999), pp. 954–956.

[65] S. W. Hell. '*Far-Field Optical Nanoscopy*'. In: *Science* **316.5828** (2007), pp. 1153–1158.

[66] A. von Diezmann, Y. Shechtman and W. E. Moerner. '*Three-Dimensional Localization of Single Molecules for Super-Resolution Imaging and Single-Particle Tracking*'. In: *Chemical Reviews* **117.11** (2017), pp. 7244–7275.

[67] G. Shtengel, J. A. Galbraith, C. G. Galbraith, J. Lippincott-Schwartz, J. M. Gillette et al. '*Interferometric fluorescent super-resolution microscopy resolves 3D cellular ultrastructure*'. In: *Proceedings of the National Academy of Sciences* **106.9** (2009), pp. 3125–3130.

[68] F. Tamburini, G. Anzolin, G. Umbriaco, A. Bianchini and C. Barbieri. '*Overcoming the Rayleigh Criterion Limit with Optical Vortices*'. In: *Physical Review Letters* **97.16** (2006), p. 163903.

[69] S. R. P. Pavani, M. A. Thompson, J. S. Biteen, S. J. Lord, N. Liu et al. '*Three-dimensional, single-molecule fluorescence imaging beyond the diffraction limit by using a double-helix point spread function*'. In: *Proceedings of the National Academy of Sciences* **106.9** (2009), pp. 2995–2999.

[70] S. Jia, J. C. Vaughan and X. Zhuang. '*Isotropic three-dimensional super-resolution imaging with a self-bending point spread function*'. In: *Nature Photonics* **8.4** (2014), pp. 302–306.

[71] P. A. Dalgarno, H. I. C. Dalgarno, A. Putoud, R. Lambert, L. Paterson et al. '*Multiplane imaging and three dimensional nanoscale particle tracking in biological microscopy*'. In: *Optics Express* **18.2** (2010), pp. 877–884.

[72] M. F. Juette, T. J. Gould, M. D. Lessard, M. J. Mlodzianoski, B. S. Nagpure et al. '*Three-dimensional sub-100 nm resolution fluorescence microscopy of thick samples*'. In: *Nature Methods* **5.6** (2008), pp. 527–529.

[73] S. Abrahamsson, J. Chen, B. Hajj, S. Stallinga, A. Y. Katsov et al. '*Fast multicolor 3D imaging using aberration-corrected multifocus microscopy*'. In: *Nature Methods* **10.1** (2012), pp. 60–63.

[74] Y. Zhou, J. Yang, J. D. Hassett, S. M. H. Rafsanjani, M. Mirhosseini et al. '*Quantum-limited estimation of the axial separation of two incoherent point sources*'. In: *Optica* **6.5** (2019), pp. 534–541.

[75] J. Řeháček, Z. Hradil, B. Stoklasa, M. Paúr, J. Grover, A. Krzic and L. L. Sánchez-Soto. '*Multiparameter quantum metrology of incoherent point sources: Towards realistic superresolution*'. In: *Physical Review A* **96.6** (2017), p. 062107.

[76] D. Petz and C. Ghinea. '*Introduction to quantum Fisher information*'. In: *Quantum Probability and Related Topics*. World Scientifc, 2011, pp. 261–281.

[77] M. Szczykulska, T. Baumgratz and A. Datta. '*Multi-parameter quantum metrology*'. In: *Advances in Physics: X* **1.4** (2016), pp. 621–639.

[78] M. Tsang. '*Subdiffraction incoherent optical imaging via spatial-mode demultiplexing: Semiclassical treatment*'. In: *Physical Review A* **97.2** (2018), p. 023830.

[79] R. Barakat. '*Application of Apodization to Increase Two-Point Resolution by the Sparrow Criterion I Coherent Illumination*'. In: *Journal of the Optical Society of America* **52.3** (1962), pp. 276–283.

[80] T. Asakura and T. Ueno. '*Apodization for increasing two-point resolution by the sparrow criterion under the partially coherent illumination*'. In: *Nouvelle Revue d'Optique* **5.6** (1974), pp. 349–359.

[81] V. P. Nayyar and N. K. Verma. '*Two-point resolution of Gaussian aperture operating in partially coherent light using various resolution criteria*'. In: *Applied Optics* **17.14** (1978), pp. 2176–2180.

[82] A. N. K. Reddy. '*Two-point resolution of asymmetrically apodized optical systems*'. In: *Optica Pura y Aplicada* **46**.textbf3 (2013), pp. 215–222.

[83] J. W. Goodman. *Introduction to Fourier Optics*. 3rd ed. Roberts and Company Publishers, 2004. 491 pp.

[84] L. Mandel and E. Wolf. *Optical coherence and quantum optics*. Cambridge University Press, 1995. 1194 pp.

[85] W. Larson and B. E. A. Saleh. '*Resurgence of Rayleigh's curse in the presence of partial coherence*'. In: *Optica* **5.11** (2018), pp. 1382–1389.

[86] M. Tsang and R. Nair. '*Resurgence of Rayleigh's curse in the presence of partial coherence: comment*'. In: *Optica* **6.4** (2019), pp. 400–401.

[87] W. Larson and B. E. A. Saleh. '*Resurgence of Rayleigh's curse in the presence of partial coherence: reply*'. In: *Optica* **6.4** (2019), pp. 402–403.

[88] Z. Hradil, J. Řeháček, L. L. Sánchez-Soto and B.-G. Englert. '*Quantum Fisher information with coherence*'. In: *Optica* **6.11** (2019), pp. 1437–1440.

[89] J. Durnin. '*Exact solutions for nondiffracting beams I The scalar theory*'. In: *Journal of the Optical Society of America A* **4.4** (1987), pp. 651–654.

[90] J. Durnin, J. J. Miceli and J. H. Eberly. '*Diffraction-free beams*'. In: *Physical Review Letters* **58.15** (1987), pp. 1499–1501.

[91] C. A. McQueen, J. Arlt and K. Dholakia. '*An experiment to study a "nondiffracting" light beam*'. In: *American Journal of Physics* **67.10** (1999), pp. 912–915.

[92] Y.-Y. Yu, D.-Z. Lin, L.-S. Huang and Ch.-K. Lee. '*Effect of subwavelength annular aperture diameter on the nondiffracting region of generated Bessel beams*'. In: *Optics Express* **17.4** (2009), pp. 2707–2713.

[93] D. DeBeer, S. R. Hartmann and R. Friedberg. '*Comment on "Diffraction-Free Beams"*'. In: *Physical Review Letters* **59.22** (1987), p. 2611.

[94] J. Durnin, J. J. Miceli and J. H. Eberly. '*Durnin, Miceli, and Eberly Reply*'. In: *Physical Review Letters* **59.22** (1987), p. 2612.

[95] J. E. Harvey and J. L. Forgham. '*The spot of Arago: New relevance for an old phenomenon*'. In: *American Journal of Physics* **52.3** (1984), pp. 243–247.

[96] J. H. McLeod. '*The Axicon: A New Type of Optical Element*'. In: *Journal of the Optical Society of America* **44.8** (1954), p. 592.

[97] G. Indebetouw. '*Nondiffracting optical fields: some remarks on their analysis and synthesis*'. In: *Journal of the Optical Society of America A* **6.1** (1989), pp. 150–152.

[98] J. A. Davis, E. Carcole and D. M. Cottrell. '*Nondiffracting interference patterns generated with programmable spatial light modulators*'. In: *Applied Optics* **35.4** (1996), pp. 599–602.

[99] Z. Bouchal. '*Controlled spatial shaping of nondiffracting patterns and arrays*'. In: *Optics Letters* **27.16** (2002), pp. 1376–1378.

[100] N. Chattrapiban, E. A. Rogers, D. Cofield, W. T. Hill. III and R. Roy. '*Generation of nondiffracting Bessel beams by use of a spatial light modulator*'. In: *Optics Letters* **28.22** (2003), pp. 2183–2185.

[101] J. Wu, Z. Wu, Y. He, A. Yu, Z. Zhang, Z. Wen and G. Chen. '*Creating a nondiffracting beam with sub-diffraction size by a phase spatial light modulator*'. In: *Optics Express* **25.6** (2017), pp. 6274–6282.

[102] A. J. Cox and Dean C. Dibble. '*Nondiffracting beam from a spatially filtered Fabry-Perot resonator*'. In: *Journal of the Optical Society of America A* **9.2** (1992), pp. 282–286.

[103] Z. Bouchal, J. Wagner and M. Chlup. '*Self-reconstruction of a distorted nondiffracting beam*'. In: *Optics Communications* **151.4-6** (1998), pp. 207–211.

[104] D. McGloin and K. Dholakia. '*Bessel beams: Diffraction in a new light*'. In: *Contemporary Physics* **46.1** (2005), pp. 15–28.

[105] R. Jáuregui and S. Hacyan. '*Quantum-mechanical properties of Bessel beams*'. In: *Physical Review A* **71.3** (2005), p. 033411.

[106] J. Arlt, V. Garces-Chavez, W. Sibbett and K. Dholakia. '*Optical micromanipulation using a Bessel light beam*'. In: *Optics Communications* **197.4-6** (2001), pp. 239–245.

[107] V. Garcés-Chávez, D. McGloin, H. Melville, W. Sibbett and K. Dholakia. '*Simultaneous micromanipulation in multiple planes using a self-reconstructing light beam*'. In: *Nature* **419.6903** (2002), pp. 145–147.

[108] T. Čižmár, V. Kollárová, X. Tsampoula, F. Gunn-Moore, W. Sibbett, Z. Bouchal and K. Dholakia. '*Generation of multiple Bessel beams for a biophotonics workstation*'. In: *Optics Express* **16.18** (2008), pp. 14024–14035.

[109] F. O. Fahrbach, P. Simon and A. Rohrbach. '*Microscopy with self-reconstructing beams*'. In: *Nature Photonics* **4.11** (2010), pp. 780–785.

[110] F. O. Fahrbach and A. Rohrbach. '*Propagation stability of self-reconstructing Bessel beams enables contrast-enhanced imaging in thick media*'. In: *Nature Communications* **3.1** (2012), p. 632.

[111] F. O. Fahrbach, V. Gurchenkov, K. Alessandri, P. Nassoy and A. Rohrbach. '*Self-reconstructing sectioned Bessel beams offer submicron optical sectioning for large fields of view in light-sheet microscopy*'. In: *Optics Express* **21.9** (2013), pp. 11425–11440.

[112] S. H. Moosavi, C. Gohn-Kreuz and A. Rohrbach. '*Feedback phase correction of Bessel beams in confocal line light-sheet microscopy: a simulation study*'. In: *Applied Optics* **52.23** (2013), pp. 5835–5842.

[113] M. McLaren, T. Mhlanga, M. J. Padgett, F. S. Roux and A. Forbes. '*Self-healing of quantum entanglement after an obstruction*'. In: *Nature Communications* **5.1** (2014), p. 3248.

[114] M. Duocastella and C. B. Arnold. '*Bessel and annular beams for materials processing*'. In: *Laser & Photonics Reviews* **6.5** (2012), pp. 607–621.

[115] C. Paterson and R. Smith. '*Helicon waves: propagation-invariant waves in a rotating coordinate system*'. In: *Optics Communications* **124.1-2** (1996), pp. 131–140.

[116] A. Dudley and A. Forbes. '*From stationary annular rings to rotating Bessel beams*'. In: *Journal of the Optical Society of America A* **29.4** (2012), pp. 567–573.

[117] D. B. Ruffner and D. G. Grier. '*Optical Conveyors: A Class of Active Tractor Beams*'. In: *Physical Review Letters* **109.16** (2012), p. 163903.

[118] B. Hadad, S. Froim, H. Nagar, T. Admon, Y. Eliezer, Y. Roichman and A. Bahabad. '*Particle trapping and conveying using an optical Archimedes' screw*'. In: *Optica* **5.5** (2018), pp. 551–556.

[119] Ch. Vetter, T. Eichelkraut, M. Ornigotti and A. Szameit. '*Optimization and control of two-component radially self-accelerating beams*'. In: *Applied Physics Letters* **107.21** (2015), p. 211104.

[120] Ch. Vetter, T. Eichelkraut, M. Ornigotti and A. Szameit. '*Generalized Radially Self-Accelerating Helicon Beams*'. In: *Physical Review Letters* **113.18** (2014), p. 183901.

[121] P. Birch, I. Ituen, R. Young and Ch. Chatwin. '*Long-distance Bessel beam propagation through Kolmogorov turbulence*'. In: *Journal of the Optical Society of America A* **32.11** (2015), pp. 2066–2073.

[122] W. Wang, Z. Wu, Q. Shang and B. Lu. '*Propagation of multiple Bessel Gaussian beams through weak turbulence*'. In: *Optics Express* **27.9** (2019), pp. 12780–12793.

[123] M. Anguiano-Morales, A. Martínez, M. D. Iturbe-Castillo, S. Chávez-Cerda and N. Alcalá-Ochoa. '*Self-healing property of a caustic optical beam*'. In: *Applied Optics* **46**.**34** (2007), pp. 8284–8290.

[124] S. Vyas, Y. Kozawa and S. Sato. '*Self-healing of tightly focused scalar and vector Bessel-Gauss beams at the focal plane*'. In: *Journal of the Optical Society of America A* **28**.**5** (2011), pp. 837–843.

[125] X. Chu. '*Analytical study on the self-healing property of Bessel beam*'. In: *The European Physical Journal D* **66**.**10** (2012), p. 259.

[126] X. Chu and W. Wen. '*Quantitative description of the self-healing ability of a beam*'. In: *Optics Express* **22**.**6** (2014), pp. 6899–6904.

[127] A. Aiello and G. S. Agarwal. '*Wave-optics description of self-healing mechanism in Bessel beams*'. In: *Optics Letters* **39**.**24** (2014), pp. 6819–6822.

[128] J. R. Jiménez and E. Hita. '*Babinet's principle in scalar theory of diffraction*'. In: *Optical Review* **8**.**6** (2001), pp. 495–497.

[129] V. Arrizon, G. Mellado-Villase ñor, D. Aguirre-Olivas and H. M. Moya-Cessa. '*Mathematical and diffractive modeling of self-healing*'. In: *Optics Express* **26**.**9** (2018), pp. 12219–12229.

[130] Ch. Vetter, R. Steinkopf, K. Bergner, M. Ornigotti, S. Nolte, H. Gross and A. Szameit. '*Realization of Free-Space Long-Distance Self-Healing Bessel Beams*'. In: *Laser & Photonics Reviews* **13**.**10** (2019), p. 1900103.

[131] R. Bracewell. *The Fourier Transform & Its Applications*. 3rd ed. McGraw-Hill Science, 1999. 640 pp.

[132] I. N. Bronshtein, K. A. Semendyayev, G. Musiol, H. Muehlig and H. Mühlig. *Handbook of Mathematics*. 5th ed. Springer, 2004.

[133] C. R. Timothy and G. S. Kino. *Confocal scanning optical microscopy and related imaging systems*. San Diego: Academic Press, 1996, p. 335.

[134] D. G. Smith. *Field Guide to Physical Optics*. SPIE, 2013. 130 pp.

[135] S. M. Kay. *Fundamentals of Statistical Processing, Volume I*. Prentice Hall, 1993. 608 pp.

[136] U. Spagnolini. *Statistical Signal Processing in Engineering*. 1st ed. John Wiley & Sons , 2018.

[137] B. C. Levy. *Principles of Signal Detection and Parameter Estimation*. Springer, 2010. 660 pp.

[138] M. G. A. Paris. '*Quantum estimation for quantum technology*'. In: *International Journal of Quantum Information* **07.supp01** (2009), pp. 125–137.

[139] I.-Ch. Khoo. *Liquid Crystals*. 2nd ed. John Wiley & Sons, 2007. 384 pp.

[140] S. R. Restaino and S. W. Teare. *Introduction to Liquid Crystals for Optical Design and Engineering*. SPIE, 2015.

[141] A. Márquez and Á. Lizana. *Liquid crystal on silicon devices : modeling and advanced spatial light modulation applications*. MDPI, 2019. 172 pp.

[142] U. Efron. *Spatial light modulator technology : materials, devices, and applications*. New York: CRC Press, 1994. 360 pp.

[143] *LC 2012 Spatial light modulator (transmissive)*. *Holoeye Photonics*.

[144] *1920 x 1152 Spatial light modulator (reflective)*. *Meadowlark*.

[145] *PLUTO-2 Phase-only spatial light modulator (reflective)*. *Holoeye Photonics*.

[146] *X13138 Phase-only LCOS spatial light modulator (reflective)*. *Hamamatsu Photonics*.

[147] R. W. Gerchberg and W. O. Saxton. '*A practical algorithm for the determination of phase from image and diffraction plane pictures*'. In: *Optik* **35.4** (1972), pp. 227–246.

[148] A. Jesacher, A. Schwaighofer, S. Fürhapter, C. Maurer, S. Bernet and M. Ritsch-Marte. '*Wavefront correction of spatial light modulators using an optical vortex image*'. In: *Optics Express* **15.9** (2007), pp. 5801–5808.

[149] A. M. Mignardi, O. R. Gale, S. D. Dawson and C. Jack. *MEMS and MOEMS Technology and Applications*. Ed. by P. Rai-Choudhury. SPIE, 2000.

[150] M. A. Mentzer. *Applied Optics Fundamentals and Device Applications*. Taylor & Francis Ltd, 2017. 368 pp.

[151] T. Gmünder. *Digital Light Processing® using digital micromirror devices : a primer*. Bellingham, Washington (1000 20th St. Bellingham WA 98225-6705 USA: SPIE, 2016.

[152] E. Abbe. '*Beiträge zur Theorie des Mikroskops und der mikroskopischen Wahrnehmung*'. In: *Archiv für Mikroskopische Anatomie* **9.1** (1873), pp. 413–469.

[153] L. Moťka, B. Stoklasa, M. D'Angelo, P. Facchi, A. Garuccio et al. '*Optical resolution from Fisher information*'. In: *The European Physical Journal Plus* **131.5** (2016).

[154] S. Ram, E. S. Ward and R. J. Ober. '*Beyond Rayleigh's criterion: A resolution measure with application to single-molecule microscopy*'. In: *Proceedings of the National Academy of Sciences* **103.12** (2006), pp. 4457–4462.

[155] Halsey Royden and Patrick Fitzpatrick. *Real Analysis*. 4th ed. Pearson, 2010. 544 pp.

[156] H. Wolter. '*Die Minimumstrahlkennzeichnung als Mittel zur Genauigkeitssteigerung optischer Messungen und als methodisches Hilfsmittel zum Ersatz des Strahlbegriffes*'. In: *Annalen der Physik* **442.7-8** (1950), pp. 341–368.

[157] J. K. T. Eu and A. W. Lohmann. '*Isotropic Hilbert spatial filtering*'. In: *Optics Communications* **9.3** (1973), pp. 257–262.

[158] A. W. Lohmann, D. M. and Z. Zalevsky. '*Fractional Hilbert transform*'. In: *Optics Letters* **21.4** (1996), pp. 281–283.

[159] F. W. J. Olver, D. W. Lozier, R. F. Boisvert and Ch. W. Clark. *NIST Handbook of Mathematical Functions*. Cambridge University Press, 2010. 968 pp.

[160] R. J. Wells. '*Rapid approximation to the Voigt/Faddeeva function and its derivatives*'. In: *Journal of Quantitative Spectroscopy and Radiative Transfer* **62.1** (1999), pp. 29–48.

[161] F. W. King. *Hilbert transforms*. Vol. **1**. Cambridge University Press, 2010.

[162] P. Henrici. *Applied and Computational Complex Analysis*. Vol. 1. John Wiley & Sons Inc, 1988. 704 pp.

[163] L. V. Ahlfors. *Complex Analysis: An Introduction to the Theory of Analytic Functions*. 2nd ed. McGraw-Hill, 1979. 352 pp.

[164] L. Vandenberghe and S. Boyd. '*Semidefinite Programming*'. In: *SIAM Review* **38.1** (1996), pp. 49–95.

[165] J. M. Bernardo and F. M. Smith. *Bayesian Theory*. John Wiley & Sons, 2000. 610 pp.

[166] M. Tsang. '*Quantum limits to optical point-source localization*'. In: *Optica* **2.7** (2015), pp. 646–653.

[167] M. P. Backlund, Y. Shechtman and R. L. Walsworth. '*Fundamental Precision Bounds for Three-Dimensional Optical Localization Microscopy with Poisson Statistics*'. In: *Physical Review Letters* **121.2** (2018), p. 023904.

[168] A. E. Siegman. *Lasers*. University Science Books, 1986. 1285 pp.

[169] C. S. Smith, N. Joseph, B. Rieger and K. A. Lidke. '*Fast, single-molecule localization that achieves theoretically minimum uncertainty*'. In: *Nature Methods* **7.5** (2010), pp. 373–375.

[170] S. Hua Tao and X. Yuan. '*Self-reconstruction property of fractional Bessel beams*'. In: *Journal of the Optical Society of America A* **21.7** (2004), pp. 1192–1197.

[171] P. Fischer, H. Little, R. L. Smith, C. Lopez-Mariscal, C. T. A. Brown, W. Sibbett and K. Dholakia. '*Wavelength dependent propagation and reconstruction of white light Bessel beams*'. In: *Journal of Optics A: Pure and Applied Optics* **8.5** (2006), pp. 477–482.

[172] J. Broky, G. A. Siviloglou, A. Dogariu and D. N. Christodoulides. '*Self-healing properties of optical Airy beams*'. In: *Optics Express* **16.17** (2008), pp. 12880–12891.

[173] M. Born and E. Wolf. *Principles of Optics*. 7th ed. Cambridge University Press, 2013. 952 pp.

[174] K. Ball. '*Ellipsoids of maximal volume in convex bodies*'. In: *Geometriae Dedicata* **41.2** (1992), pp. 241–250.

[175] I. A. Litvin, M. G. McLaren and A. Forbes. '*A conical wave approach to calculating Bessel-Gauss beam reconstruction after complex obstacles*'. In: *Optics Communications* **282.6** (2009), pp. 1078–1082.

[176] M. A. Nielsen and I. L. Chuang. *Quantum Computation and Quantum Information*. Cambridge University Press, 2010. 702 pp.

[177] A. N. Kolmogorov. *Elements of the Theory of Functions and Functional Analysis*. Dover Publications Inc., 1999. 288 pp.

[178] M. Hillery. '*Nonclassical distance in quantum optics*'. In: *Physical Review A* **35.2** (1987), pp. 725–732.

[179] A. B. Klimov, L. L. Sánchez-Soto, E. C. Yustas, J. Söderholm and G. Björk. '*Distance-based degrees of polarization for a quantum field*'. In: *Physical Review A* **72.3** (2005), p. 033813.

[180] S. Gnutzmann and K. Zyczkowski. '*Rényi-Wehrl entropies as measures of localization in phase space*'. In: *Journal of Physics A: Mathematical and General* **34.47** (2001), pp. 10123–10139.